THE EFFECT OF Au DIFFUSION-DOPED ON STRUCTURAL, SUPERCONDUCTING AND MECHANICAL PROPERTIES OF $Bi_{1.8}Pb_{0.35}Sr_{1.9}Ca_{2.1}Cu_3O_y$

by

ÖZGÜR ÖZTÜRK

THESIS SUBMITTED TO
THE GRADUATE SCHOOL OF NATURAL AND APPLIED SCIENCES
OF
THE ABANT İZZET BAYSAL UNIVERSITY
IN PARTIAL FULFILLMENT OF THE REQUIREMENTS FOR THE DEGREE
OF
DOCTOR OF PHILOSOPHY
IN
THE DEPARTMENT OF PHYSICS

OCTOBER 2007

Approval of the Graduate School of Natural and Applied Science

Prof. Dr. Nihat ÇELEBİ

Director

I certify that this thesis satisfies all the requirements as a thesis for the degree of Doctor of Philosophy.

Prof. Dr. Ahmet Turan ALAN

Head of Physics Department

This is to certify that we have read this thesis and that in our opinion it is fully adequate, in scope and quality as a thesis for the degree of Doctor of Philosophy.

Assoc. Prof. Dr. Cabir TERZİOĞLU

Supervisor

Examining Committee Members

1. Prof. Dr. İbrahim BELENLİ ……
2. Assoc. Prof. Dr. Cabir TERZİOĞLU ……
3. Assoc. Prof. Dr. Saffet NEZİR ……
4. Assist. Prof. Dr. Ömer ÇAKIROĞLU ……
5. Assist. Prof. Dr. Mustafa NURSOY ……

ABSTRACT

THE EFFECT OF Au DIFFUSION-DOPED ON STRUCTURAL, SUPERCONDUCTING AND MECHANICAL PROPERTIES OF $Bi_{1.8}Pb_{0.35}Sr_{1.9}Ca_{2.1}Cu_3O_y$

Öztürk, Özgür

Ph-D., Department of Physics

Supervisor: Assoc. Prof. Dr. Cabir Terzioğlu

October 2007, 149 pages

In this study, we have investigated the effect of the gold diffusion-doping and diffusion-annealing duration on structural, superconducting and mechanical properties of the $Bi_{1.8}Pb_{0.35}Sr_{1.9}Ca_{2.1}Cu_3O_y$ superconductors annealed 830°C for 10, 20, 50 hours. The samples were prepared by the conventional solid-state reaction method in the polycrystalline bulk form. Doping of *Bi-2223* was carried out by means of *Au* diffusion during sintering from an evaporated *Au* films on pellets. The experimental works in this study consist of DC electrical resistivity, critical current

density and AC susceptibility measurements for electrical, magnetic and superconducting properties, microhardness measurements for mechanical properties (such as Vickers microhardness, Young's modulus, fracture toughness and yield strength). The mechanical properties of the samples were found to be diffusion annealing time and load dependent. Powder X-ray diffraction for phase analyses and lattice parameters, and SEM for microstructure examinations were carried out. These measurements showed that *Au* doping, in comparison with the undoped samples, increased the lattice parameter *c*, grain size, critical current density, and critical transition temperature, improved the mechanical properties and enhanced formation of *Bi-2223* phase. Moreover, as the diffusion-annealing time decreased the number and size of voids increased, transition temperature, critical current density, lattice parameter *c* decreased. Additionally, we have calculated the activation energies and diffusion coefficients of *Au* in *BSCCO*. For this reason, the undoped samples were coated with an *Au* layer and diffusion annealing was carried out 500, 600, 700, 750 and 800°C for 10 hours. There are several methods to estimate the diffusion parameter in polycrystalline high-T_c superconductors. The most common four methods are: successive removal of thin layers and (1) the measurement of the sample's resistivity, (2) the measurements of lattice parameters from XRD patterns, (3) the energy dispersive X-ray fluorescence, and (4) the radio-tracer methods. In this study, we used first two techniques to calculate the diffusion coefficient of *Au* in *Bi(Pb)-Sr-Ca-Cu-O* system. The temperature dependence of the *Au* diffusion coefficients in the range of 500-800°C was described by the relation $D = D_0 \exp(-E_a/k_BT)$. It was obtained that for diffusion of *Au* atoms in *Bi-2223* in the temperature range 500-800°C, the coefficients of diffusion increases, the corresponding activation energy being 1.08 eV. Diffusion at lower annealing

temperatures is much less significant. The possible reasons for the observed improvements in structural, superconducting and mechanical properties due to *Au* diffusion in the superconductor BSCCO samples were discussed.

Keywords: *Bi-2223*, *Bi-2212*, High temperature superconductor, Diffusion coefficient, Transition temperature, Transport critical current density, Intergrain and Intragrain critical current density, Mechanical properties,

ÖZET

$Bi_{1.8}Pb_{0.35}Sr_{1.9}Ca_{2.1}Cu_3O_y$ SÜPERİLETKENİNDE Au DİFÜZYONUNUN YAPISAL, ÜSTÜNİLETKENLİK VE MEKANİK ÖZELLİKLERİ ÜZERİNE ETKİSİ

Öztürk, Özgür

Doktora, Fizik Bölümü

Tez Danışmanı: Doç. Dr. Cabir Terzioğlu

Ekim 2007, 149 sayfa

Bu çalışmada, katıhal tepkime yöntemiyle hazırlanan $Bi_{1,8}Pb_{0,35}Sr_{1,9}Ca_{2,1}Cu_3O_y$ süperiletken numunelerinin bir yüzeyine altın buharlaştırılarak 830°C' de 10, 20 ve 50 saat' lik tavlama sonucu ince altın tabakasının numuneye difüze olması sağlandı. Bu işlemden sonra, difüzyon yolu ile numuneye altın katkılamanın ve difüzyon ısıl işlem süresinin numunelerin süperiletkenlik, yapısal ve mekanik özellikleri üzerindeki etkileri incelendi. Karşılaştırma yapmak için aynı şartlarda katkısız numune de hazırlandı. Elektrik, manyetik ve süperiletkenlik özelliklerini belirlemek

için DC özdirenç, kritik akım yoğunluğu ve AC alınganlık ölçümleri yapıldı. Mekanik özelliklerini belirlemek için ise mikrosertlik ölçümleri yapıldı. Numunelerin mekanik özellikleri difüzyon ısıl işlen süresine ve yüke bağlı olarak belirlendi. Faz analizi ve örgü parametrelerinin belirlenmesi için X-ışınları kırınımı incelemesi, mikroyapı incelemeleri için ise SEM ölçümleri yapıldı. Bu ölçümler sonucunda altın katkılanmış numune ile ve katkısız numune karşılaştırdığında, *c* örgü parametresinin, kritik akım yoğunluğunun, kritik dönüşüm sıcaklığının arttığı ve taneciklerin büyüdüğü gözlendi. Ayrıca mekanik özellikler ve *Bi-2223* fazında iyileşmeler belirlendi. Difüzyon ısıl işlem süresi azaldıkça, numune yüzeyindeki boşlukların sayısı ve büyüklüğü artmış, *c* örgü parametresi, kritik dönüşüm sıcaklığı ve kritik akım yoğunluğu azalmıştır. Bunlara ek olarak altının difüzyon katsayısı ve aktivasyon enerjisi hesaplandı. Bu sebeple 500, 600, 700, 750, 800 °C de 10 saat süreyle difüzyon-tavlaması yapılarak katkısız numune üzerine buharlaştırılan ince altın tabakasının numuneye difüze olması sağlandı. Yüksek sıcaklık süperiletkenlerde difüzyon parametrelerinin belirlenmesinde birkaç metot vardır. Bunlardan en yaygın olanları şunlardır: Numunenin özdirencini ölçerek, numunelerin XRD verilerinden örgü parametrelerini hesaplayarak, X-ray Fluorescence tekniği ve radio-tracer yöntemidir. Bu çalışmada yukarıda bahsedilen ilk iki yöntem kullanıldı. 500-800°C arasında üretilen altın katkılanmış *Bi-2223* numunelerinin difüzyon ısıl işlem sıcaklığına bağlı difüzyon katsayısını hesaplamak için $D=D_0\ exp(-E_a/k_BT)$ bağıntısı kullanıldı ve altının aktivasyon enerjisi (E_a), 1,08 eV olarak hesaplandı. Bu çalışmada, süperiletken BSCCO numunesine difüzyon yoluyla altın kakılanmasıyla meydana gelen yapısal, süperiletkenlik ve mekanik özelliklerindeki iyileşmenin nedenleri tartışıldı.

Anahtar Kelimeler: *Bi-2223* fazı, *Bi-2212* fazı, Yüksek sıcaklık süperiletkenler, Difüzyon katsayısı, Geçiş sıcaklığı, Taşıma kritik akım yoğunluğu, Taneler arası ve tane içi akım yoğunluğu, Mekanik özellikler.

To my parents…

ACKNOWLEDGMENTS

It is a great pleasure to thank many people who have contributed to the completion of this thesis through their knowledge, guidance, support and friendship. First of all, I would like to thank my thesis supervisor, Assoc. Prof. Dr. Cabir Terzioğlu for his support, guidance, patience and encouragement during the preparation of this thesis. My understanding of physics has been improved by his enthusiasm and practical viewpoints. I also, thank to Prof. Dr. İbrahim Belenli and Assoc. Prof. Dr. Ahmet Varilci for many discussions, their assistances and enlightening comments on my works over the years.

I am grateful to Assoc. Prof. Dr. Saffet Nezir, Assist. Prof. Dr. Ömer Çakıroğlu, and Assist. Prof. Dr. Erdal Bekiroğlu along with my advisor for serving on my thesis committee.

I would like to express my gratitude to Assist. Prof. Dr. Mustafa Nursoy for SEM work and Hardness tests at A.I.B University Faculty of Engineering.

I also acknowledge Assist. Prof. Dr. Tayfur Küçükömeroğlu for XRD work at Karadeniz Technical University.

I would like to thank all my friends for their kind help, especially, Assist. Prof. Dr. Musrafa Yılmazlar, R. A. Mustafa Akdoğan, Expert Cihan Parlak, R. A. Murat Erdem, and R. A. Hüseyin Aydın.

I want to thank specially to Prof. Dr. Ali Gencer and Assist. Prof. Dr. Ahmet Kılıç for AC Susceptibility measurements at Ankara University.

Finally in my personal side I would like to thank my wife, Demet, and my parents for their continuous supports, patience and encouragement which made it possible for me to continue my research.

This work is supported partly by the Scientific and Technological Council of Turkey (Project No: 104T325) and partly the Turkish State Planning Organization (DPT) (Project No: 2004K120200).

TABLE OF CONTENTS

Page

LIST OF TABLES

TABLE **Page**

LIST OF FIGURES

FIGURE **Page**

CHAPTER 1

INTRODUCTION

Every element and compound that exists in nature has a specific electrical resistance. As the resistance depends on both physical and chemical properties of the material, it can be changed by the effects of outside factors. The resistivity of metals and compounds can be expressed by $\rho = \rho_0 + \rho_i$, where ρ_0 is the resistivity caused by the thermal phonons, and ρ_i is the resistivity caused by scattering of the electron waves by static defects that disturb the periodicity of the lattice (dislocation). Often ρ_0 is independent of the number of defects when their concentration is small, and often ρ_i is independent of temperature. This empirical expression is known as "Mattheissen's rule" [1].

It is observed that when some metals and some compounds are cooled enough, nearly to the liquid helium temperature, their resistance falls down to zero and they have no resistance value against current. This process, which is called superconductivity, was discovered by Kamerlingh Onnes, (Hg) [2]. Onnes was studying the electrical resistance of metals, and with early experiments on platinum and gold he observed that at low temperatures the resistance approached a finite value (residual resistance) and become independent of temperature. This was attributed to the scattering of conduction electrons by impurity atoms. Thinking about studying a purer metal, he decided to examine mercury because it could easily

be purified by multiple distillations. The resistance of mercury was measured as a function of temperature and was observed to drop to an immeasurably low value at 4.15 K. Over 20 metal elements and many compounds and alloys have this property at liquid helium temperature.

In those years scientists did not have enough knowledge about the magnetic properties of the superconductors. The next great milestone occurred in 1933, 20 years after Onnes discovery, the scientists W. Meissner and R.Ochsenfeld discovered that a superconducting material repels magnetic field. According to this discovery, if the superconducting material is cooled below its critical temperature in the presence of an applied magnetic field, it expels all magnetic flux from its interior. If the field is applied after the material has been cooled below its critical temperature, the magnetic flux is excluded from the superconductor. Thus a superconductor is a perfect diamagnet, this property is called “Meissner effect” [3].

In 1957, John Bardeen, Leon Cooper, and Robert Schrieffer developed the first complete microscopic theory of superconductivity (BCS). In the theory, electrons form “cooper pairs” that move in coordinated manner. It was remarkably complete description for conventional low temperature superconductors.

As a result of these important inventions many scientists searched for the way of using superconductors in technology. But there were two main problems. One of them is the need of very low temperature for superconductivity. Once the liquid helium was produced this problem was overtaken but this was an expensive method. The second problem is that, the state of being a superconductor of a sample is corrupted by outside magnetic field and electrical current which are applied to the sample.

Those two problems delayed the use of superconductors in technology. To overcome these problems, samples which can be superconductors at high temperature had been searched. Until 1973, the compound Nb_3Ge, which has a high critical temperature (23.2 K) was the superconductor with the highest superconducting temperature [4].

This was not enough for the scientists but according to the BCS theory, the maximum critical temperature of the superconductivity is suggested to be around 30-35 K. Many scientists have searched for years to obtain superconductor samples in liquid nitrogen temperature which is easy and cheap to produce.

In 1986, Muller and Bednorz, who were working at IBM Zurih, found the critical temperature as 35 K for the compound *La-Ba-Cu-O* prepared by using barium oxide and cupper oxide [4]. In1987, Wu Ashburn et al. found a new compound, *Y-B-C-O*, by using yttrium oxide instead of lanthanum oxide and the critical temperature was over 90 K [5]. This was really an important progress because a new sample which shows superconductivity above liquid nitrogen temperature and is easier to produce and cheaper was found. In 1987, a new chain is added to the superconductivity studies. Michael et al. found the superconductivity in *Bi-Sr-Cu-O* system [6]. In 1988, Maeda and his group observed superconductivity at 105 K by adding calcium to this system as *Bi-Sr-Ca-Cu-O* [7]. Also Tokano and his group stabilized this superconductor at 110 K, by adding lead to the system [8].

There is a tremendous amount of work on *Bi(Pb)-Sr-Ca-Cu-O* system since its discovery [6, 7, 8]. *BSCCO* samples are characterized by a wide variety of techniques. Empirically, the superconducting transition temperature T_c becomes higher with an increasing number of CuO_2 layers. The high T_c 2:2:2:3 ($Bi_2Sr_2Ca_2Cu_3O_{10}$, 110 K) phase is extremely difficult to prepare in a pure form since

it usually intergrows with the 2:2:1:2 ($Bi_2Sr_2CaCu_2O_8$, 85 K) phase. Many studies of doping into superconductor oxide ceramics have been tried in order to improve their mechanical and superconducting properties [9-19]. After the discovery of *Bi*(*Pb*)-*Sr-Ca-Cu-O* system, researchers began to investigate answers for questions such as what happens if the noble metals like *Ag* and *Au*, which are in the same column as Cu in the Periodic Table, are added to the system. The researchers found that silver addition enhances the critical current density (J_c) [19, 20], improves the superconducting transition temperature (T_c) [21, 22], mechanical properties and electrical stability [23], and reduces the normal-state resistivity, and the contact resistance [22, 24]. It is also known that silver addition improves grain growth and helps to obtain a better grain orientation [21, 25-27]. On the other hand, Jin et al. [28] found that the gold addition degraded the superconductivity of *Bi*(*Pb*)-*Sr-Ca-Cu-O*. Liu et al. [29] found that the *Au* addition did not affect T_c and lattice parameters. It was also found that the gold addition did not affect the formation of the *Bi-2223* [30]. These contradictory reports directed us to this problem.

It could be observed that in all of the investigations, the gold addition of *Bi*(*Pb*)-*Sr-Ca-Cu-O* was carried out in the mixed powders before the pressing and the sintering of pellets. However, gold diffusion in this superconductor has not attracted much attention. The diffusion coefficients of gold may be useful for the understanding of doping mechanism and changes of microstructure and superconducting properties of *BSCCO* systems under doping. Dzhafarov et al. [31] reported the effect of *Au* diffusion combined with slow and fast cooling on critical temperature and critical current density in *Bi*(*Pb*)-*Sr-Ca-Cu-O* system. To our knowledge, no detailed work on the calculation of the *Au* diffusion coefficient in a *Bi*(*Pb*)-*Sr-Ca-Cu-O* bulk sample has been published in the literature. It was observed

that the gold-diffusion doping of *Bi*(*Pb*)-*Sr*-*Ca*-*Cu*-*O* at the sintering process with a fast cooling promotes formation of the high-T_c *Bi-2223* phase and significantly increases J_c [31], which may rather be related with preventing the formation of the impurity phases by fast cooling.

The mechanical properties such as hardness, elastic modulus, yield strength, fracture toughness, brittleness index, ductility, etc. are as important as the superconducting parameters for industrial applications like quasi-permanent magnets and current leads. Regarding mechanical properties, hardness test provides useful information on the strength and deformation properties of the materials. So many studies of doping into superconductor oxide ceramics have been made in order to improve their mechanical properties. Hardness is a mechanical parameter and it is strongly related to the structure and composition of solids. Microhardness is not only a routinely measured mechanical characteristic; it has also been developed as an investigation method of structural parameters. The Vickers microhardness test is one of the convenient methods to estimate the mechanical properties. Finally, the experimental results of hardness measurements were analyzed using the Kick's law, modified proportional sample resistance (MPSR) model and the Hays-Kendall (HK) approach.

The properties of superconductivity are presented in chapter 2. Evaluation of high temperature superconductors and crystal structure of *Bi*(*Pb*)-*Sr*-*Ca*-*Cu*-*O* system are presented in chapter 3. Chapter 4 gives diffusion mechanism of superconductors. Experimental methods of this investigation are outlined in chapter 5. Results and discussions are presented in chapter 6. And finally chapter 7 gives conclusions.

CHAPTER 2

THE PROPERTIES OF SUPERCONDUCTIVITY

2.1 Introduction

The electrical resistivity of many metals and alloys drops suddenly to zero when the sample is cooled to a sufficiently low temperature, often a temperature in the liquid helium range. The phenomenon is called superconductivity.

As we mentioned before, Kammerlingh-Onnes found that the electrical resistance of solid mercury drops to an immeasurably small value when cooled below a certain temperature called the critical temperature T_c in 1911 [2]. Mercury goes from a normal state to a superconducting state as the temperature drops below T_c = 4.2 K as shown in Figure 2.1. Fallowing this discovery many other elements, many compounds and alloys, were found to be superconductors with critical temperatures as high as 23 K, but not all materials superconduct. In 1957 Bardeen, Cooper and Schrieffer (BCS) gave an explanation to this phenomenon. However, the discovery of an unusually high-T_c superconductor by Bednorz Müller (1986) has caused complete change of the general view on superconductivity because it is no longer limited only to very low temperatures. It is even more fascinating than previously thought, and its industrial application became conceivable.

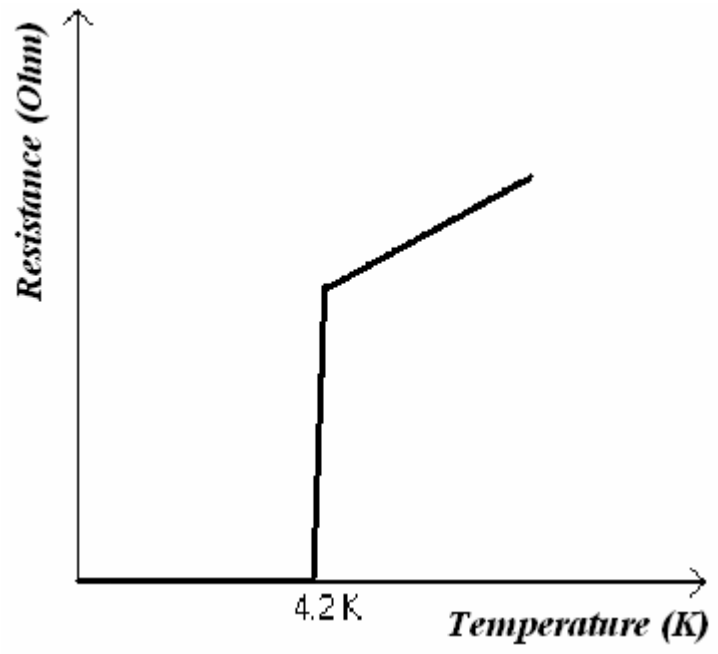

Figure 2.1: The resistance of a mercury sample as a function of temperature.

The most striking features of a superconductor are [32];

1- A superconductor can behave as if it had no measurable DC electrical resistivity.

2- A superconductor can behave as a perfect diamagnet. A sample in thermal equilibrium in an applied magnetic field, provided the field is not too strong, carries electrical surface currents. These currents give rise to an additional magnetic field that precisely cancels the applied magnetic field in the interior of the superconductor.

3- A superconductor usually behaves as if there were a gap in energy of width 2Δ centered about the Fermi energy, in the set of allowed one-electron levels [33].

The magnetic properties of superconductors are very important as their electrical properties. It is a fact that a bulk superconductor in a weak magnetic field will act as a perfect diamagnet, with zero magnetic induction in the interior. When a sample is placed in a magnetic field and is then cooled through the transition temperature for

superconductivity, the magnetic flux originally present is ejected from the sample. This phenomenon is known as the “Meissner effect”.

2.2 Loses Resistance and Critical Temperature

As long as the superconductor is cooled to very low temperatures, the cooper pair stays intact, due to the reduced molecular motion. As the superconductor gains heat energy the vibration in the lattice become more violent and breaks the pairs. As they break, superconductivity diminishes. Superconducting metals and alloys have a characteristic transition temperature from the stage of normal conductors to the stage of superconductors [33]. Below the superconducting transition temperature, the resistivity

of the material is exactly zero. Superconductors made from different materials have different T_c values.

2.3 Persistent Current

Above T_c , the resistivity has the form characteristic of a normal metal

$$\rho(T) = \rho_0 + BT^5 \tag{2.1}$$

In the above equation, constant term is arising from impurity, and defect scattering, and the term T^5 arising from phonon scattering as shown in Figure 2.2.a. Below T_c, this mechanisms lose power to degrade an electric current and the resistivity drops

abruptly to zero as shown in Figure 2.2.b. Currents flow in a superconductor with no discernible dissipation of energy [34]. There are some limitations:

a) Superconductivity is destroyed by application of sufficiently large magnetic field.

b) If the current exceed a "critical value", the superconducting state will be destroyed. The size of critical current depends on the nature and geometry of sample.

c) A superconductor well below T_c will also respond without dissipation to an AC electric field [33].

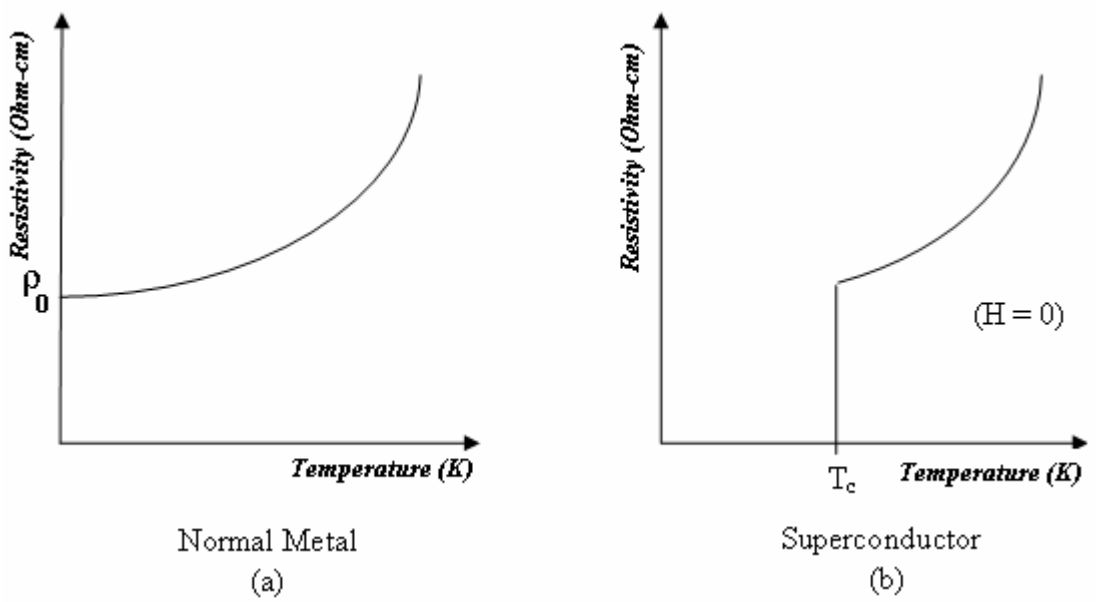

Figure 2.2: (a) Low-temperature resistivity of a normal metal ($\rho(T) = \rho_0 + BT^5$) containing nonmagnetic impurities. **(b)** Low-temperature resistivity of a superconductor (in zero magnetic field) containing nonmagnetic impurities. At T_c, ρ drops abruptly to zero [1].

2.4 Magnetic Properties

Magnetic flux is excluded from the interior of a superconducting sample in an applied magnetic field. Figure 2.3 shows induction field lines near normal and superconducting samples in identical applied magnetic fields (Meissner Effect).

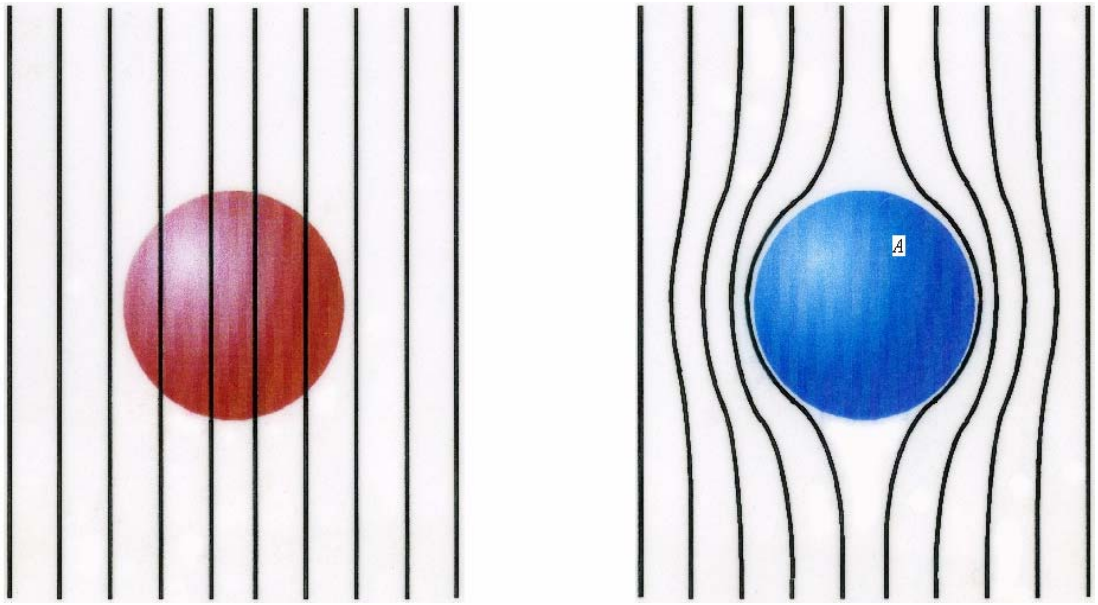

Normal state Superconductor state

Figure 2.3: Meissener effect in a superconducting sphere cooled in a constant applied magnetic field; on passing below the transition temperature the lines of induction B are ejected from the sphere [32].

2.4.1 Perfect Diamagnetism

Flux exclusion is not complete near a sample surface. Rather, the induction field decays exponentially with distance into the sample. The characteristic penetration depth is typically a few hundred angstroms.

Current exists at the surface of superconductors in a magnetic field, but not in its interior. According to the steady state Maxwell equation $\nabla \mathbf{x}\ \mathbf{B} = \mu_0\ \mathbf{J}$, so $\mathbf{J} = 0$ in the interior of a field free region. Surface current, on the other hand, create an induction field that cancels the applied field in the interior and augments it in the region just outside the surface. Here **B** is the applied magnetic field, **J** is the current density.

Superconductors are often described as perfect diamagnets, with magnetic susceptibilities of -1. To discuss flux exclusion in terms of magnetization and susceptibility, we think of supercurrents as magnetization currents. The magnetization is given by $\mathbf{M} = \chi\ \mathbf{H}$, so $\mathbf{B} = \mu_0 (\mathbf{H}+\mathbf{M}) = \mu_0 (1+\chi) \mathbf{H}$ and, since $\mathbf{B} = 0$ in the interior, $\chi = -1$. Where **M** is the magnetization, χ is the magnetic susceptibility, μ_0 is the magnetic permeability, **H** is the external intensity of the magnetic field.

Flux exclusion is plausible if a magnetic field is turned on while a sample is in a superconducting state. An Emf and current are induced by the changing field. When the field current reaches its final strength the emf vanishes but current remains in a narrow boundary region near the sample surface and its field cancels the applied field in the interior.

What happens if a normal sample is placed in a magnetic field, then cooled to below the transition temperature? It might be expected that the induction field be the same before and after cooling as shown in Figure 2.4 [35]. Our conclusion is based on Faraday's law $\partial\mathbf{B} / \partial t = -\nabla \times \varepsilon$, which becomes $\partial\mathbf{B} / \partial t = 0$ in the absence of an electric field. The conclusion is not true. In fact, super currents are generated and flux is excluded from the interior as the temperature passes the transition point. For

type I superconductors the expulsion of flux is sudden and, except for a narrow boundary region, is complete.

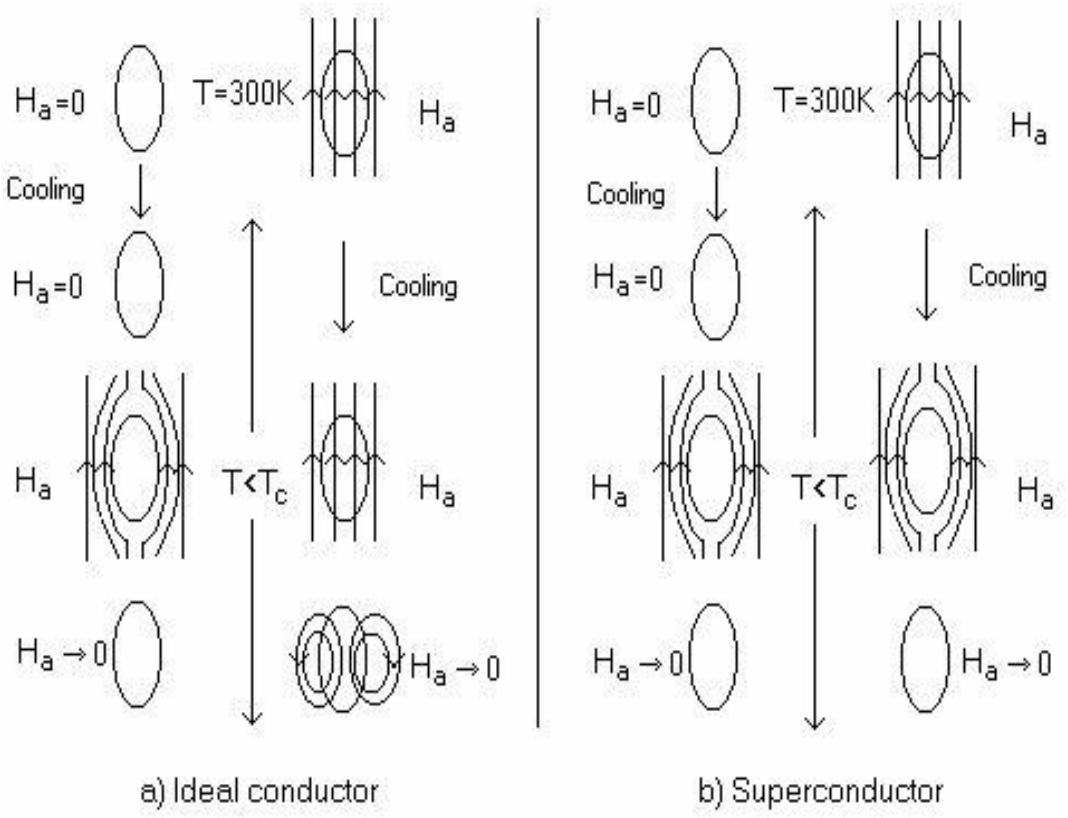

Figure 2.4: The behavior of the **(a)** ideal conductor and **(b)** superconductor in magnetic field [35].

2.4.2 Critical Magnetic Field

If the magnetic field applied to a superconductor is sufficiently strong it destroys superconductivity and the sample becomes normal conductors divide into two classes according to their behavior in a magnetic field.

2.4.2.1 Type I Superconductors

A weak induction field applied parallel to the axis of a cylindrical sample is completely excluded from the sample except for a narrow boundary region. As the applied field strength is increased, penetration suddenly takes place when the critical field is reached. Magnetization as a function of applied field is shown in Figure 2.5.

Critical fields for type I superconductors are temperature dependent. Except near T_c, the critical field is nearly quadratic and is given by $H_c = H_0 (1- (T/T_c)^2)$ in the temperature, as shown in Figure 2.6 for a typical type I superconductor.

We can use the critical field to estimate the change in energy that occurs at a superconducting transition. Consider a superconductor at T = 0 K and calculate the magnetic energy that must be supplied to convert the superconductor to the normal state by increasing the external magnetic field. The energy per unit volume required to change the magnetization by d**M** is $dE = - \mu_0 H \, d\mathbf{M}$ or, since $\mathbf{M} = - \mathbf{H}$ in a superconductor, $dE = \mu_0 \mathbf{H} \, d\mathbf{H}$. Integrate this from $\mathbf{H} = 0$ to $\mathbf{H} = \mathbf{H_c}$ (0) and find $\Delta E = 1/2 \, \mu_0 H^2_c (0)$. This must be the change in energy per unit volume that occurs when the sample passes through the transition point in the absence of an applied field. For a critical field of $5x10^4$ A/m, $\Delta E = 1.6x10^3$ J/m^3.

Once the critical field is reached and the sample turns to normal state, flux penetration occurs. If the sample is a long cylinder exposed to field, the field strength is the same at all points on the surface and flux penetration takes place uniformly. For other geometries, penetration at one point on the surface may require different applied field strength than penetration at another. For example, if the sample is a

cylinder with its axis perpendicular to the applied field, as in Figure 2.3, field at the point A is twice that of the applied field.

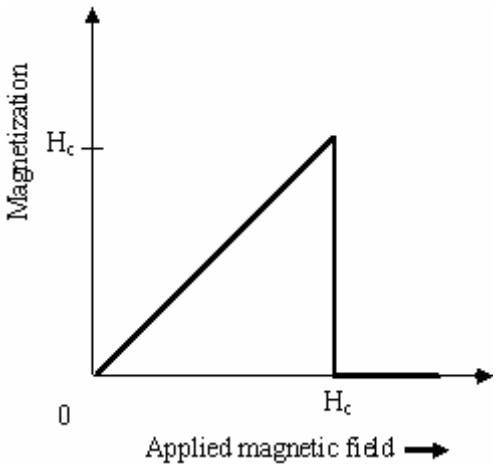

Figure 2.5: The magnitude of the magnetization **M** as a function of H_a for a type I superconductor. **M** is given by **B** / μ_0, where **B** is the induced field produced by supercurrent on a sample surface [1].

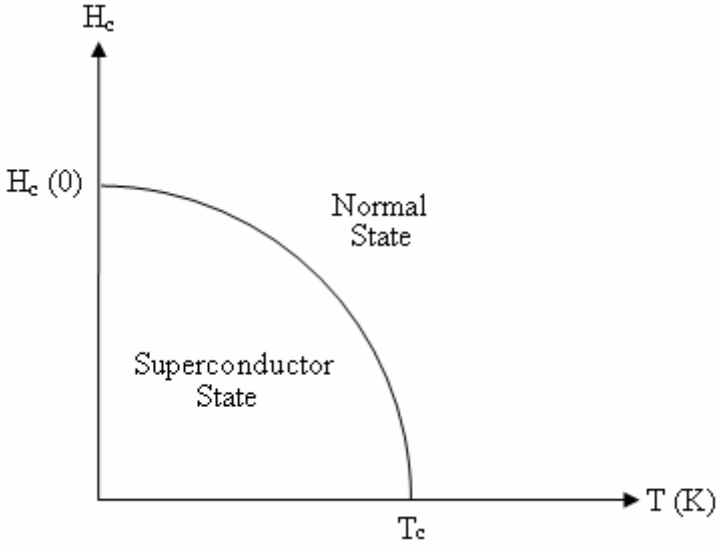

Figure 2.6: The critical field H_c as a function of temperature for a typical type I superconductor. It is maximum for T = 0 and is zero for T > T_c [33].

2.4.2.2 Type II Superconductors

This is also called "High-T_c superconductor". Two critical field points are important for type II superconductor. These are H_{c1} and H_{c2}. Figure 2.7 shows the variation of the magnetization as a function of the applied magnetic field.

At values of H_a between 0 and H_{c1} the magnetization displaces the features at that of type I superconductors. For H_a values between H_{c1} and H_{c2} the magnetization decreases exponentially from its maximum to its minimum (0) value. In the third region, between H_{c2} and H_{c3} the penetration of the magnetic field completely diminishes.

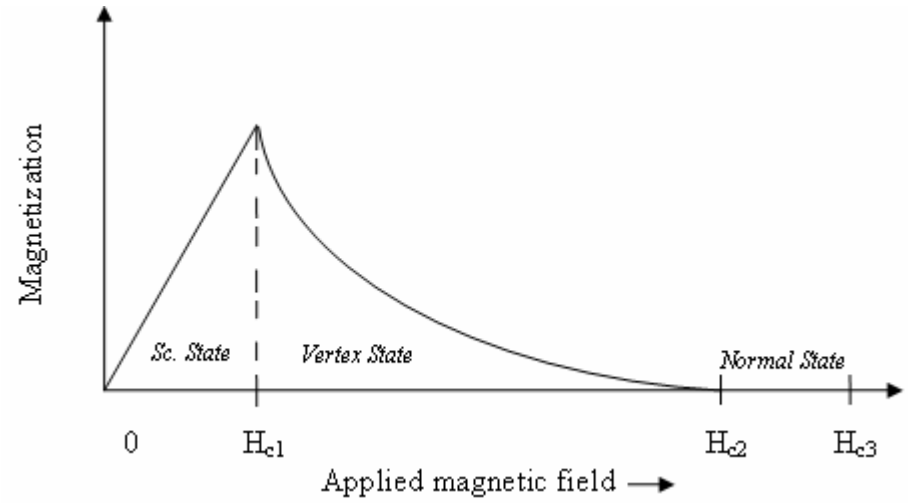

Figure 2.7: The magnitude of the magnetization **M** as function of applied field H_a for a type II superconductor. Below H_{c1} flux is excluded and $\mathbf{M} = -\mathbf{H_a}$. Between H_{c2} and H_{c3} the bulk of the sample is normal but a narrow region at the surface is superconducting. Above H_{c3} the entire sample is normal [1].

2.5 Penetration Depth

Magnetic fields are expelled from the interior of a type I superconductor by the formation of surface currents. In reality, these currents are not formed in infinitesimally thin layer on the surface. Instead, they penetrate the surface to a small extent, within this layer, which is about 100 nm in depth. The magnetic field B inside a type I superconductor decreases exponentially from its external value to zero according to the expression

$$B(x) = B_0 e^{-x/\lambda} \tag{2.2}$$

where it is assumed that the external magnetic field is parallel to the surface of the sample. In this equation, B_o is the value of the magnetic field at the surface, x is the distance from the surface to some interior point, and λ is a parameter called the penetration depth. The variation of the magnetic field inside a semi-infinite type I superconductor with distance is plotted in Figure 2.8. The superconductor occupies the region on the positive side of the x axis. The magnetic field becomes very small at depth a few times λ below the surface. The values of the λ are typically in the range of 10–100 nm. The penetration depth varies with temperature according to empirical expression:

$$\lambda (T) = \lambda_0 [1 - (T / T_c)^2]^{-½} \tag{2.3}$$

where λ_0 is the penetration depth at T = 0K [12].

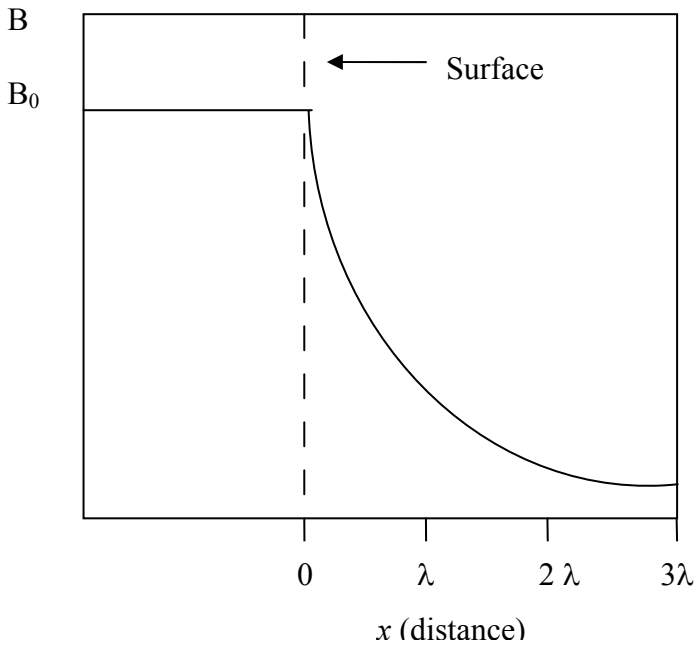

Figure 2.8: The magnetic field B inside a semi-infinite superconductor versus distance *x* from its surface. The field outside the superconductor (for $x < 0$) is B_0, and the superconductor is to the right of the dashed line [12].

2.6 Coherence Length

Another important parameter associated with superconductivity is called the coherence length, ξ. One can think of the smallest dimension over which superconductivity can be established or destroyed. Alternatively, one can view the coherence length as the distance over which the electrons in a Cooper pair remain together. In the BCS theory, the coherence length is directly related to distance over which the two electrons in a cooper remain correlated.

A superconductor will be type I if the coherence length is larger than the penetration depth, λ. Most pure metals fall into this category. On the other hand, an increase in the ratio λ/ξ favors type II superconductivity. A detailed analysis shows

that coherence length and penetration depth depend on mean free path of a metal. The mean free path can be reduced by adding impurities to the metal. On the other hand, addition of impurities increases the penetration depth and decreases the coherence length. As a result the material undergoes at transition from type I to type II superconductor [12].

2.7 BCS Theory

In 1957, Bardeen, Cooper and Schrieffer proposed a detailed microscopic theory, now known as the BCS in which these interactions are included. The predictions of the BCS theory are in excellent agreement with experimental results in type I superconductors.

An electron in a solid passing by adjacent ions in the lattice can act on these ions with a set of coulomb attractions which gives each of the ions momentum that causes the ion to move together on a small region. Because of the elastic properties of the lattice, this region of increased positive charge density will than propagate as a wave, which carries momentum, through the lattice. The electron has emitted a phonon! The momentum of the phonon carriers is supplied by the electron, whose momentum was changed when the phonon was emitted. If a second electron subsequently passes by the moving region of increased positive charge density, it will experience an attractive Coulomb interaction, and thereby it can absorb all the momentum the moving region carries. That is, the second electron can absorb the phonon, thereby absorbing the momentum supplied by the first electron. The net effect is that the two electrons have exchanged some momentum with each other and thus they have interacted with each other. Although the interaction was a two-step,

one involving a phonon as an intermediary, it certainly was an interaction between the two electrons. Furthermore, it was an attractive interaction, since the electron involved in each of the steps participated in an attractive Coulomb interaction [1, 12].

The BCS theory shows that in certain conditions the attraction between two electrons due to a succession of a phonon exchange can exceed slightly the repulsion which they exert directly on each other because of the (shielded) Coulomb interaction of their like charges. Then the electrons will be weakly bound together, and form a so-called cooper pair. Therefore the cooper pairs are responsible for superconductivity [36].

2.7.1 The Results of BCS Theory

- An attractive interaction between electrons can lead to ground state separated from excited states by an energy gap [1].
- The electron-lattice-electron interaction leads to an energy gap of the observed magnitude, as shown in Figure 2.9 ($2\Delta = 3.53.kT_c = E_g$).

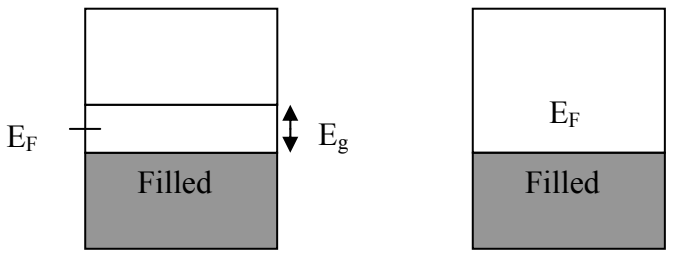

(a) Superconductor (b) Normal Metal

Figure 2.9: (a) Energy gap at the Fermi level in the superconducting state. **(b)** Conduction band in the normal state [12].

- The penetration depth and the coherence length emerge as natural consequences of BCS theory. The London equation is obtained for magnetic fields that vary slowly in space. Thus the central phenomenon in superconductivity, the Meissner effect, is obtained in a natural way [1].

- $T_c = 1.14\ \theta \exp(-1/U\ D(E_F))$

θ is the Debye temperature, U is an attractive interaction and $D(E_f)$ is the density of state [1].

- Magnetic flux through a superconducting ring is quantized and the effective unit of charge is 2e rather than e. The BCS ground state involves pairs of electrons; thus flux quantization in terms of the pair charge 2e is a consequence of the theory [1].

- It has been observed that the critical temperature of superconductors varies with isotopic mass. In mercury T_c varies from 4.185 K to 4.146 K as the average atomic mass M varies from 199.5 to 203.4 atomic mass units. The transition temperature changes smoothly when we mix different isotopes of the same elements. The experimental results within each series of isotopes may be fitted by relation of the from $m^{\alpha}\ T_c$ = constant [1].

CHAPTER 3

EVOLUTION OF THE HIGH TEMPERATURE SUPERCONDUCTORS

In 1908, three years after the discovery of liquid helium, Kamerling Onnes discovered that the electrical resistance of Hg decrease to small undetectable values under a certain critical temperature (T_c) [2]. This observation is known as the discovery of superconductivity. After the discovery of superconductivity the highest T_c observed was 23.2 K for Nb_3Ge compound. Moreover, the BCS theory which explains superconductivity microscopically as electron-lattice-electron interaction theoretically predicted maximum critical temperature about 30-35 K for superconductors. However, early in 1986, J.George Bednorz and Karl Alex Muller, two scientists at IBM Research Laboratory in Zurich, made a remarkable discovery that has resulted in a revolution in the field of superconductivity. They found that an oxide of lanthanum, barium, and copper in a mixed-phase form of a ceramic become superconducting at about 30 K [4].

The superconducting phase was soon identified at other laboratories as the compound $La_{2-x}Ba_xCuO_4$ where $x \approx 0.2$. Announcements of higher temperature superconductivity were met with great skepticism, since such high critical temperatures were quite unexpected, especially in a metallic oxide. By replacing barium with strontium, researchers soon raised the value of T_c to about 36 K. Inspired by these developments, scientists worldwide worked feverishly to discover

materials with even higher T_c values, and research in the superconducting behavior of metallic oxides accelerated at tremendous page. The lower temperature system $La_{2-y}R_yCuO_{4-x}$ shows superconductivity at varying T_c's for R = Ba, Ca, or Sr the critical temperature is found to vary with x, peaking for R = Sr and x = 0.15 at T_c = 40.3 K [37, 38].

Early in 1987, research groups at the University of Alabama and the University of Houston (Wu Ashburn et al.) announced the discovery of superconductivity near 92 K in a mixed-phase sample containing yttrium, barium, copper, and oxygen [5]. This was really an important progress because a new sample which shows superconductivity in liquid nitrogen temperature and is easier to produce and cheaper was found. The discovery was confirmed in other laboratories around the world, and the superconducting phase was soon identified to be the compound $YBa_2Cu_3O_{7-x}$. By looking at the ratios of barium yttrium and copper, this compound is called as 1:2:3 or *Y-B-C-O* [39-42]. The newly found sample was in perovskite structure as in *La-Ba-Cu-O* compound. The difference between two compounds is oxygen vacancy. By means of those vacancies, there is the possibility of changing the critical temperature [43]. In *YBCO* system the yttrium can be replaced by ten or more other elements, including magnetic ions, without a significant decrease in T_c thus, the systems $RBa_2Cu_3O_{7-x}$ have been shown to have T_c's of 75-95 K where R = Sr, La, Nd, Sm, Eu, Gd, Dy, Ho, Er, Y or Lu [44, 45].

Several complex metallic oxides in the form of ceramics have been investigated, and critical temperatures above (triple-digit superconductivity) have been observed. In 1987, a new chain is added to the superconductivity studies. Michael et al. found the superconductivity in *Bi-Sr-Cu-O* system [6]. In 1988, Maeda and his group observed superconductivity at 105 K by adding calcium to this system

as *Bi-Sr-Ca-Cu-O* [7]. Also Tokano and his group found a stable superconductor at 110 K, by adding lead to the system [8]. Addition of lead increases the ratio of the phase which has high critical temperature. In 1992, Quidwai and his group observed the transition to superconductivity at 130-140 K by adding antimony to the system [46].

In 1988, Sheng and Parkin observed superconductivity in *Tl-Ba-Ca-Cu-O* compound first at 110 K and then at 125 K, but this compound has cancerogenic effect and was not stable and it has to be produced each time.

In 1993, Schilling and his group observed superconductivity in $HgBa_2Ca_2Cu_3O_{1+x}$ compound at 133 K and Chu and his group observed superconductivity in high pressure with Hg based compounds at 150 K [47]. The highest T_c obtain up to date is 164 K (under 31 GPa Pressure) for Hg-based superconductors by Gatt et al. Some physical properties of high temperature superconductors are given in Table 3.1

During the years from 1986 till today, important developments occurred in these compounds which are called 'Type II superconductors'. And during this time first type superconductors were neglected. In 2001, J.Nagamatsu, J.Akimitsu and their group observed superconductivity in MgB_2 compound at 39 K [48]. This was a very important improvement in Type I superconductors. Although the sample was a type I its critical temperature was quite high. And since it was elastic, it had the advantage of being easy to be adapted to technology. A study on this system is going on and it is still popular.

Table 3.1: Some physical properties of high temperature superconductors [47].

HIGH TEMPERATURE SUPERCONDUCTOR MATERALS	**T_c (K)**	**Number of Cu-O Layers in unit cell**	**DISCOVERY YEAR AND SCIENTIST**
$YBa_2Cu_3O_{7-\delta}$	**92**	**2**	Wu et al. **(1987)**
$Bi_2Sr_2CaCu_2O_8$	**85**	**2**	Maeda et al. **(1988)**
$Bi_2Sr_2Ca_2Cu_3O_{10}$	**110**	**3**	Chu and Hazen **(1988)**
$Tl_2Ba_2CaCu_3O_8$	**110**	**3**	Sheng / Parkin **(1988)**
$Tl_2Ba_2Ca_2Cu_4O_{10}$	**125**	**4**	Sheng / Parkin **(1988)**
$HgBa_2CaCu_2O_{6+x}$ and $HgBa_2Ca_2Cu_3O_{1+x}$	**126** **133**	**2** **3**	Schilling et al. (**1993)**
Hg – based compound under high pressure	**~ 150**	**2 or 3**	Chu et al. (**1993)**

The superconductors containing cupper-oxide layers are generally called "HTSc" (High Temperature Superconductor) and they have a potential of technological applications. Because the HTSc can be used in liquid nitrogen in

applications as opposed to the conventional superconductors are produced as thin and thick films, wires, and stripes. For the engineering applications, these materials have a potential of commercial market share around the world. In the near future, applications will be possible at liquid nitrogen temperature with the replacement of conventional superconductors with HTSc.

It has been well established that these new copper oxides exhibit the two characteristic properties of superconductors, namely zero resistivity and diamagnetism. In addition, they are known to have the fallowing properties:

- They have been determined to be type II superconductors with very high upper critical fields, greater than 100T.
- They are very anisotropic in nature, as evidenced by their small resistivities in the copper-oxygen planes, and much higher resistivities in the direction perpendicular to these planes.
- They have a granular or ceramic composition. Because of these properties, they have the unfortunate mechanical problem of being very brittle and inflexible.
- There appears to be a direct correlation between their superconducting properties and their crystallographic structures that contain oxygen deficient copper layers and chains.
- Substitution of atoms on the copper oxide layers degrades or destroys the superconductivity, while atomic substitution at other sites has little effect on superconductivity.
- The critical current densities in bulk polycrystalline samples are low, but much higher in well-oriented thin films [12].

3.1 Crystal Structure

3.1.1 Introduction

The new high-T_c materials are all copper oxides of one form or another. The various superconducting compounds that have been extensively studied to date can be classified in terms of the so-called perovskite crystal structures. Compounds with the perovskite structure have the formula of ABO_3. A is a relatively large ion in the center of cube (unit cell), and B is a smaller ion at the corners, while oxygen ions are at the unit cell edges. The perovskite structure is also described with the A ion at the corners of a cubic unit cell, the B ion in the center, oxygen ions in the faces. For touching ions, it can be seen from geometric considerations that the $\sqrt{2}$ times the B-O distance along the edge of the cube is equal to the A-O distance [49]. The first class (Figure 3.1a) is a cubic perovskite ($a=b=c$) such as $BaPb_{1-x}Bi_xO_3$ one of the original "high-T_c materials" which has $T_c \approx 10$ K. The second, known as the $KNiF_4$ structure (Figure 3.1b) is a single layer perovskite having a tetragonal distortion ($a=b\neq c$), of which $La_{1.85}Sr_{0.15}CuO_4$ is an example, having $T_c \approx 38$ K. Note that the lattice parameters a and b are measured in the copper-oxygen planes, while c is perpendicular to these planes. The third class is a multi-layer perovskite (Figure 3.1c) such as $YBa_2Cu_3O_7$ ($T_c \approx 92$ K), whose structure is orthorhombic ($a\neq b\neq c$). Compounds in this class are sometimes called 1:2:3 materials because of their relative metallic composition.

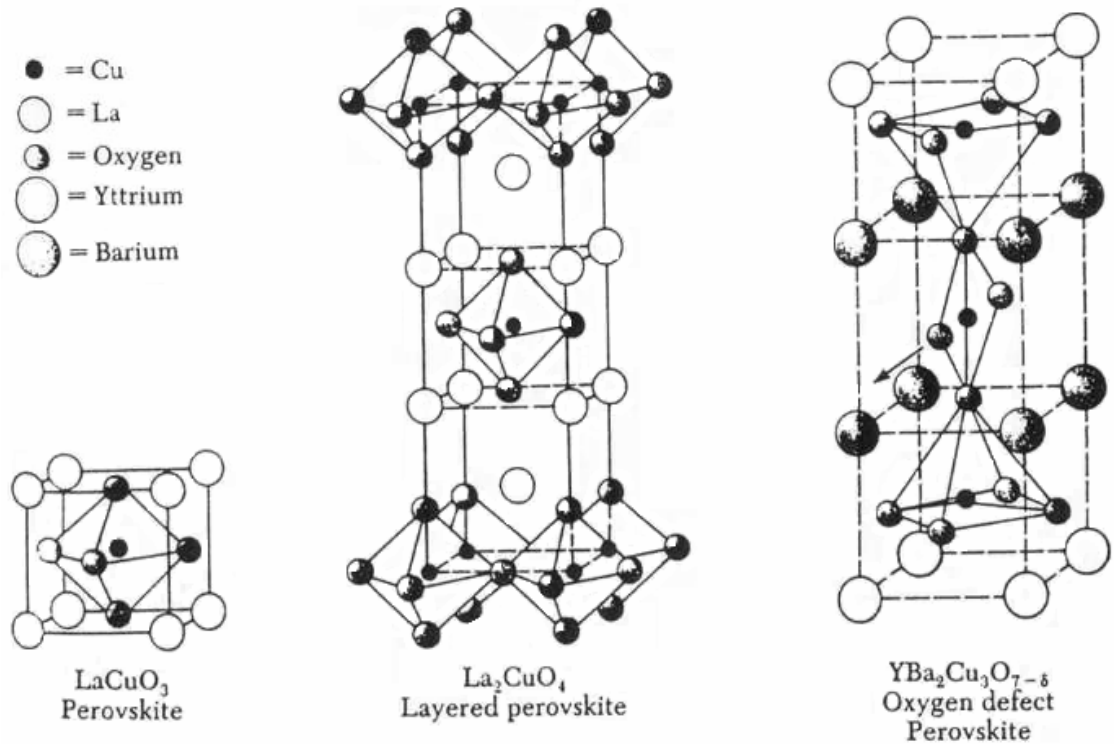

Figure 3.1: Crystal structures for some of the new superconducting materials whose general class structure is perovskite. **(a)** The fundamental perovskite unit. **(b)** The single-layered perovskite having a tetragonal distortion ($a=b\neq c$). **(c)** The double-layered perovskite with its orthorhombic structure ($a\neq b\neq c$) [12].

3.1.2 Bi-Based High Temperature Superconductors

This family of superconductor as a wide area of study because they do not contain poison elements or rare earth elements. Bi-based superconductors are very close to technological applications. In 1997, Michel et al. discovered superconductivity in *Bi-Sr-Cu-O* system [6]. In 1988, Meada et al. added Ca to this system and produced *Bi-Sr-Ca-Cu-O* with a high T_c of about 105 K [7]. In later studies, although higher critical temperatures were obtained, resistivity became zero

for lower temperature. In 1908, Takano et al. added Pb to this system and obtained superconductivity onset temperature at 110 K and achieved a stable superconductor [8]. Addition of Pb, increase the ratio of high temperature phase and improve to electrical properties.

The discovery of the *Bi-Sr-Ca-Cu-O* compounds in 1988 made it possible to consider useful polycrystalline forms of high-T_c material, as week links seemed less of a problem in *BSCCO*.

There are three superconducting phases in the BSCCO system, which are $Bi_2Sr_2Cu_1O_x$ (2201), $Bi_2Sr_2Ca_1Cu_2O_x$ (2212), and $Bi_2Sr_2Ca_2Cu_3O_x$ (2223). The three phases differ mainly by the number of Cu-O layers that rest between the Bi-O layers which cap the unit cell. Presently, the most promising of the *BSCCO* compounds for long length conductor manufacture is *BSCCO*-2223, which is the *BSSCO* phase with highest T_c at about 110 K.

The almost two dimensional character of the 2223 compounds is responsible for poor flux pinning within the grains. However, at temperatures below ~ 30 K, where flux pinning is strong. 2223 tapes can carry significant current densities in very high magnetic fields. Although conventional low-T_c materials can carry significantly greater current densities at low magnetic fields, the BSCCO compounds can carry higher current densities at fields above ~ 8 T. Thin films or single crystals of a number of other high-T_c materials can carry even greater J_c values, but presently they can not be economically made into long lengths of conductor. Although *BSCCO*-2212 typically has better properties than *BSSCO*-2223 at 4.2 K, its low T_c (~ 80 K) makes only the 2223 phase attractive for operation at liquid nitrogen temperatures.

3.1.3 Crystal Structure of The $Bi_2Sr_2Ca_{n-1}Cu_nO_y$ (n=1, 2, 3) System

Bi-based high temperature superconductors crystallize in the form of $Bi_2Sr_2Ca_{n-1}Cu_nO_y$ [50]. Here n is the number of cupper-oxide layers in the range of 1, 2, 3 and T_c increase with increasing n.

3.1.3.1 Crystal Structure of the $Bi_2Sr_2CuO_6$ System

The lowest T_c (0-20 K) of the Bi-based superconductors is $Bi_2Sr_2CuO_6$ (2201) compound which first discovered by Michel et al. in 1987 has a tetragonal symmetry with lattice parameters $a = 3.81\sqrt{2} = 5.39$ °A, $c = 24.6$ °A [50].

In figure 3.2, the unit cell of $Bi_2Sr_2CuO_6$ which is known as 2201 is shown [47]. Along the c axis the block consisting of two Sr-O and one Cu-O layers repeat itself with a translation of $a/2$, $a/2$ in the xy plane and form the unit cell. In the crystal structure the bases are Bi-O layers and copper atoms form an octahedral structure with the closest 6 oxygen atoms.

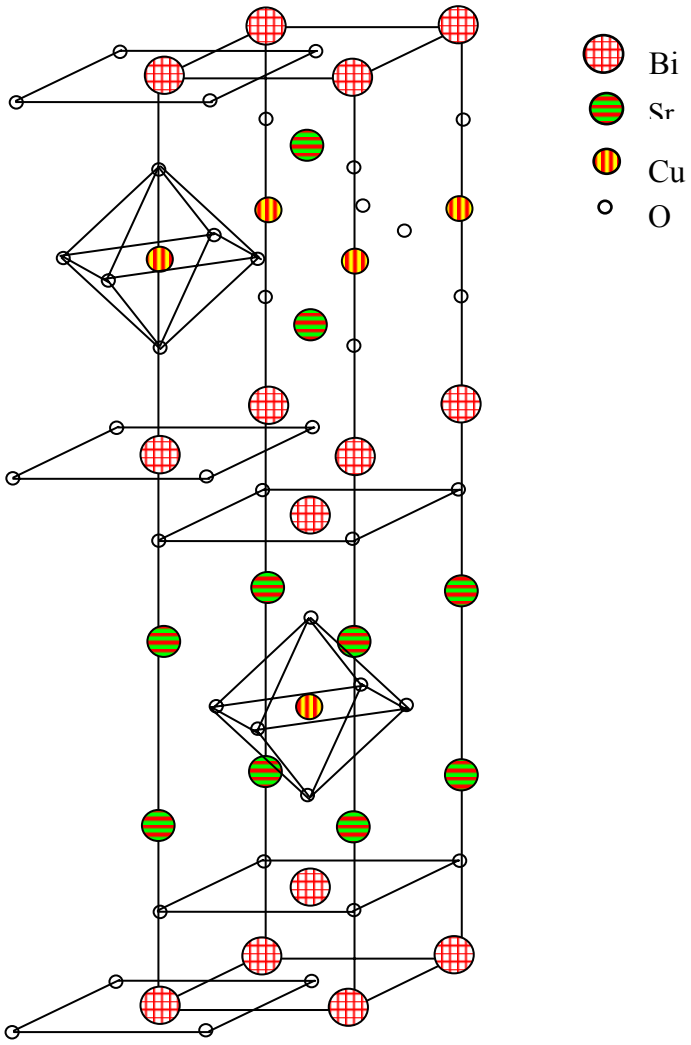

Figure 3.2: Crystal structure of $Bi_2Sr_2CuO_6$ compounds.

3.1.3.2 Crystal Structure of the $Bi_2Sr_2CaCu_2O_8$ System

$Bi_2Sr_2CaCu_2O_8$ compound is produced by addition of Ca to $Bi_2Sr_2CuO_6$ system by Maeda et al. It has a crystal structure of pseudo-tetragonal with lattice parameters a = 5.4 °A, and c = 30.6 °A. This compound also known as 2212 phase for n = 2 in $Bi_2Sr_2Ca_{n-1}Cu_nO_y$ form has a critical transition temperature 75-85 K [50].

Figure 3.3 shows the crystal structure of $Bi_2Sr_2CaCu_2O_8$ compounds [47]. The 2212 compound is composed of Bi-O layers in the bases and two Sr-O, two Cu-O layers and one Ca layer. The copper atoms form an octahedral structure with 6 oxygen atoms in 2201 compound but in 2212 compound it form pyramid structure with 5 oxygen atoms. Along the *ab* plane between these Cu-O pyramids, there are Ca atoms without oxygen bound.

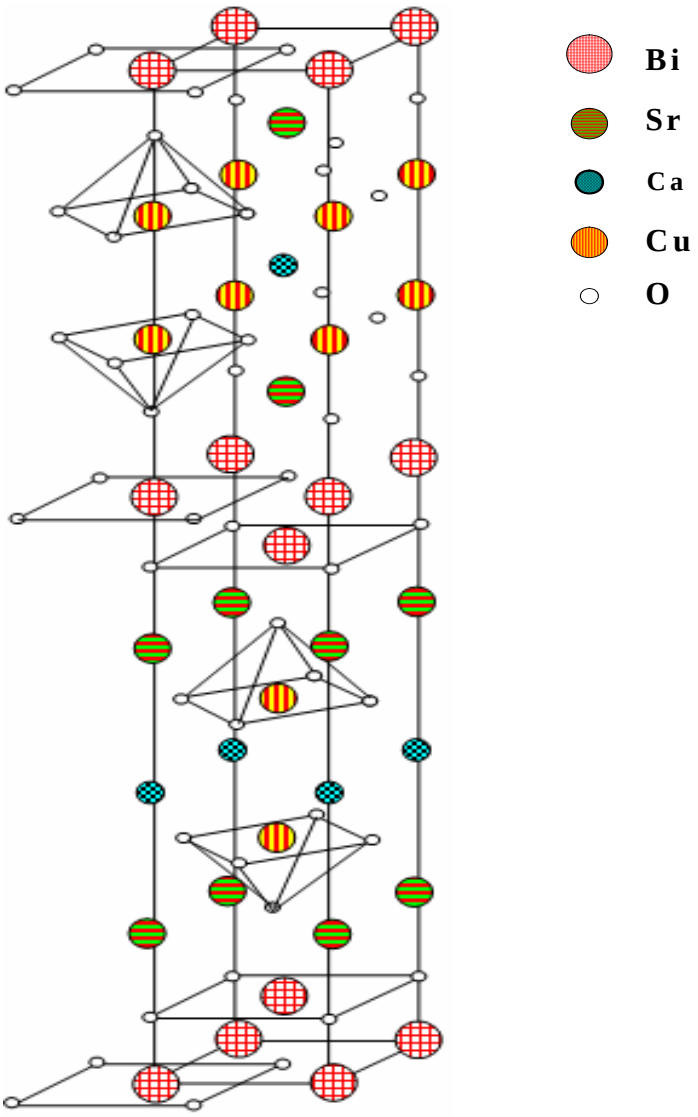

Figure 3.3: Crystal structure of $Bi_2Sr_2CaCu_2O_8$ compounds.

3.1.3.3 Crystal Structure of the $Bi_2Sr_2Ca_2Cu_3O_{10}$ System

$Bi_2Sr_2Ca_2Cu_3O_{10}$ (2223) compound with a T_c at 110 K is in the form of pseudo-tetragonal structure. It is composed of two Bi-O layers, two Sr-O layers, two Ca and Three Cu-O layers [51].

Figure 3.4 shows the crystal structure of 2223 phase [47]. Addition of one Ca and one Cu-O_2 layer to the crystal structure of 2212 phase increase *c* value to 37,1 °A. As shows in figure, in addition to the pyramid structure the copper atoms form square layers with 4 oxygen atoms.

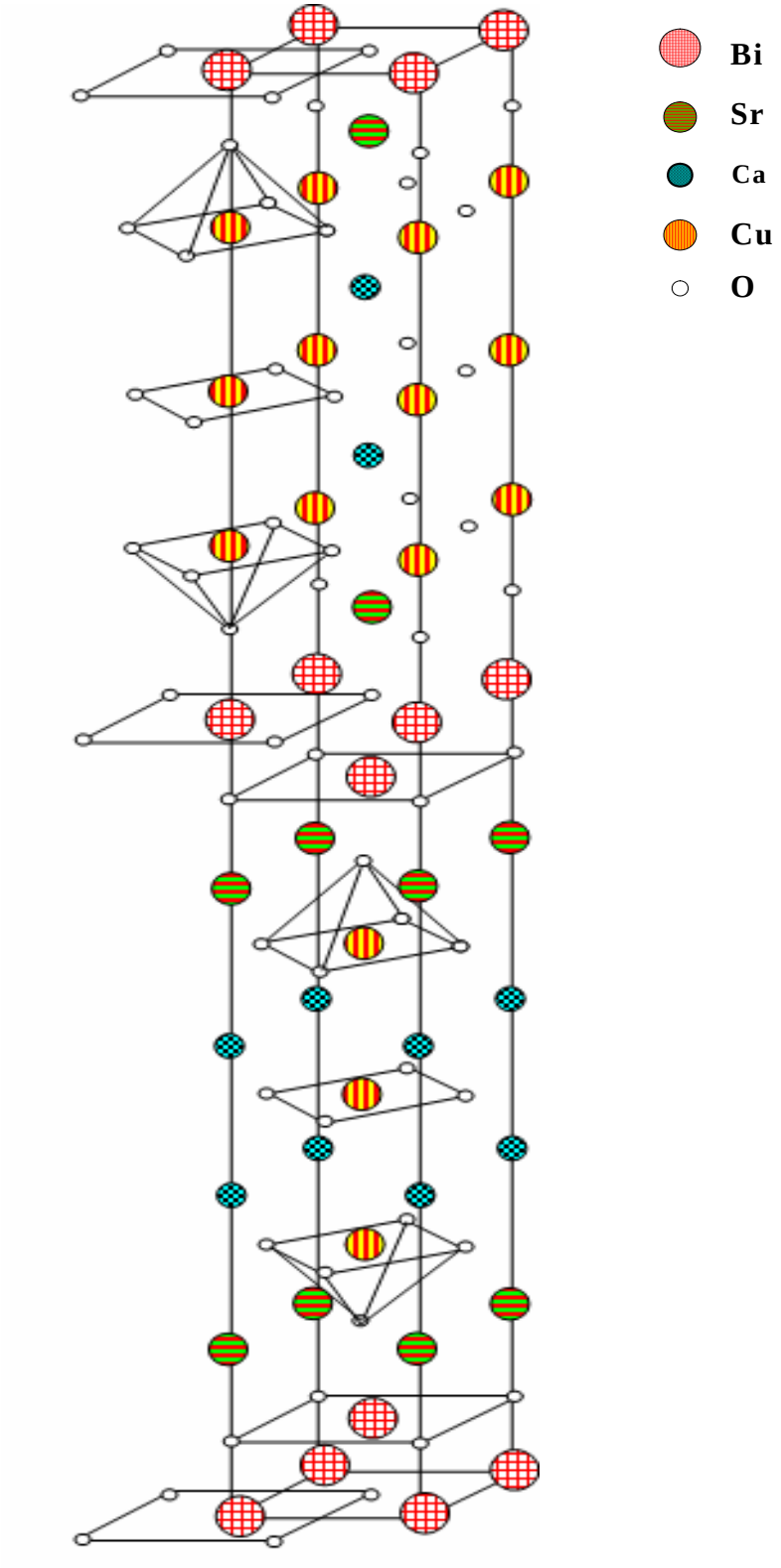

Figure 3.4: Crystal structure of $Bi_2Sr_2Ca_2Cu_3O_{10}$ compounds.

CHAPTER 4

DIFFUSION MECHANISM OF SUPERCONDUCTORS

4.1 Introduction

This chapter is summarized from "Atomic Diffusion in Semiconductor Structures" [52]. The widespread use of diffusion technology in the production of superconductor devices in the past two decades has stimulated much theoretical and experimental research into the diffusion of impurity atoms in superconductors and related diffusion phenomena. This research has yielded significant amount of scientific information which clarifies with the fundamental questions in solid-state physics, in particular those dealing with the mechanism of atomic migration in superconductors, and has also led to the development of precision engineering methods for fabricating superconductor devices.

4.2 Structural Defects and the Mechanisms of Atomic Migration

Real crystal contain various structural defects which have a substantial influence on the many physical properties solids and play a decisive role in diffusion processes and related phenomena.

Point defects are any irregularities of atomic dimensions in the crystal structure. This is the simplest class of defects and can be present in a crystal under conditions of thermodynamic equilibrium. Point defects include vacancies, interstitial atoms, antistructure defects, and impurity atoms. In addition to these, complexes of the vacancy-vacancy type, vacancy-impurity-atom type, and more complicated complexes of vacancies and atoms are also point defects.

Defects in solids are divided into Frenkel defects and Schottky defects. When an atom moves from a lattice site to an interstitial side, a pair of defects is created in the crystal-a vacancy and an interstitial atom (Frenkel defects). Isolated vacancies in a regular crystal lattice are Schottky defects. The mechanism by which such defects from can be thought of as an evaporation of atoms from a surface (boundary) layer and the subsequent migration of the vacancies into the volume. In crystals with close packing, the Schottky defects are the more common [52].

The concentration of Schottky defects (of vacancies, N_v) depends exponentially on the temperature.

$$N_v=N_0 \exp(-G_v/kT). \tag{4.1}$$

Here G_v is the free energy of vacancy formation, which is defined by the relation

$$G_v= E_v-TS_v; \tag{4.2}$$

N_0 is the number of lattice sites in the crystal (per cm^3), E_v and S_v are the energy and entropy of vacancy formation, respectively, and k is the Boltzmann's constant. The concentration of Frenkel defects also obeys an exponential law:

$$N_F = \sqrt{N_0}\, N_i \exp(-G_v/2kT), \quad (4.3)$$

Where, N_i is the number of interstitial sites (per cm^3).

In addition to these simple point defects, a real crystal can contain linear defects, two-dimensional defects (surface defects, stacking faults, grain boundaries, blocks and twins, phase boundaries), and there-dimensional defects (second-phase inclusions, voids, etc.).

Dislocations occur in two forms; edge dislocations and screw dislocations. An edge dislocation can arise as a result of a slip of part of the crystal with respect to the other; the dislocation is defined as the boundary between the slipped and unslipped parts of the crystal. A screw dislocation can be represented as a crystal with a screw dislocation is an atom plane twisted into a holicoid. A grain boundary is a region between two small crystals (grains) of solid, in which the atoms are less densely paced than in the volume of the crystals [52].

In a crystalline solid, owing to the presence of both a regular sequence of lattice sites and a collection of structural defects, which are energetically favourable positions for atoms, it is relatively easy (in comparison with the case of gases, liquids, and amorphous solids) to describe the elementary jumps of atoms from one equilibrium positions to another that lie at the heart of diffusion processes. Depending on the type of elementary jump from one equilibrium position to another, one can represent the possible migration mechanisms as:

a) Pair exchange

b) Ring exchange

c) Interstitial mechanism

d) Vacancy mechanism

e) Dissociative mechanism

f) Migration via dislocations

g) Migration via stacking faults

h) Migration via grain boundaries.

The simplest mechanism of an elementary jump, which does not require the presence of structural defects, is a direct exchange of places between two adjacent atoms. An exchange of this sort should be hindered in close-paced crystals because of the need for strong compressions of the surrounding atoms during the elementary jump. If the direct exchange involves the simultaneous participation of several atoms located in a ring, with the result that the entire ring is rotated by one inter atomic distance, the mechanism is called “ring change”. Although a ring exchange does not require as high a compression of the crystal lattice as in the case of a pair exchange, the probability for the ring migration mechanism in crystals is small. A ring exchange of atoms, like a pair exchange, can occur in structurally perfect (defect less) crystals.

The interstitial mechanism comes into play when a diffusion atom moves from one equilibrium position in an interstitial site to another interstitial position. This type atomic migration has higher probability for atoms with small radii in crystals which are not close-packed [52].

A variation of the interstitial mechanism is the jumping of an atom from an interstitial site to an occupied lattice site, with the result that the atom which was originally located at the lattice site is knocked into an interstitial position. This mechanism occurs in the self- diffusion of silver in silver halides.

In the vacancy mechanism of migration the elementary diffusion event consists of the jumping of an atom a lattice site into an adjacent vacancy, so that the atom and vacancy exchange places.

In binary compounds, and also superconductors, diffusion can occur by a dissociative mechanism, which is a combination of the vacancy and interstitial mechanism. Here an atom from a lattice site moves into an interstitial position, migrates via interstitial sites, and then moves back into a vacancy. Some time later, the cycle is repeated

Diffusion via dislocations, grain boundaries, and stacking faults in a solid should occur more readily than diffusion in the volume of the crystal, since in the regions of the crystal structure is disrupted. The kinetics of atomic migration near these linear and surface defects is hard to analyze. The density of dislocations, stacking faults, and grain boundaries is less temperature dependent than the concentration of point defects, which governs the rate of migration in the volume of a crystal. Consequently, the temperature dependence of the diffusion coefficient should be weak in the case of impurity diffusion via dislocations, stacking faults, and grain boundaries. Diffusion via these defects should be important at relatively low temperatures, whereas volume diffusion is predominant at higher temperature. Diffusion via linear and surface defects is also complicated by processes involving the decomposition of supersaturated solid solutions of impurities in solids, in which these defects can serve as centers for the precipitation of new phases [52].

4.3 Mathematical Principles of Diffusion in Superconductors

For the free diffusion of noninteracting atoms in a homogeneous and isotropic solid in the absence of external forces, the flux J of diffusing particles is proportional to the concentration gradient (*dN/dx*), the relation between these quantities being given in the one dimensional case by Fick's first law:

$$J = -D \frac{\partial N}{\partial x}, \tag{4.4}$$

Where, D is the atomic diffusion coefficient, which has the explicit expression given in fallowing relation;

$$D = \alpha a^2 \upsilon \tag{4.5}$$

Here, a is the jump length, υ is the jumping frequency, α is the geometrical factor.

$\alpha = \frac{1}{6}$ Simple cubic crystal

$\alpha = \frac{1}{8}$ Body centred cubic crystal

$\alpha = \frac{1}{12}$ Face centred cubic crystal

The jumping frequency is given by the expression

$$\upsilon = \upsilon_0 \exp\left(\frac{S}{k}\right)\exp\left(-\frac{W}{kT}\right), \tag{4.6}$$

Where, υ_0 is the natural vibration frequency of the atoms, *S* and *W* are the activation entropy and enthalpy (Activation energy) respectively, which are related to the Gibbs free energy by $G = W - TS$. Substituting expression 4.6 into 4.5, we obtain

$$D = \alpha a^2 \nu_0 \exp\left(\frac{S}{k}\right)\exp\left(-\frac{W}{kT}\right). \tag{4.7}$$

For the case in which the diffusion coefficient is independent of the concentration of migrating particles, the application of the continuity equation to equation 4.4 yields Fick's second law, which establishes a connection between the time of diffusion and the concentration of diffusing atoms at various point in the body:

$$\frac{\partial N}{\partial t} = -\frac{\partial J}{\partial x}, \tag{4.8}$$

$$\frac{\partial N}{\partial t} = \frac{\partial}{\partial x} D \frac{\partial N}{\partial x} = D \frac{\partial^2 N}{\partial x^2}. \tag{4.9}$$

The solution of equation 4.9 takes different forms depending on the boundary and initial conditions. Let us briefly consider the solution of equation 4.9 for diffusion in a semi-infinite solid under the conditions which are most frequently encountered in practice.

Diffusion from a constant source is usually realized in experiments on the diffusion of impurity atoms from the gas phase or from the thick film deposited on the surface of a sample, when a constant concentration of the impurity is maintained on the surface of the sample over the entire course of the diffusion anneal. The boundary and initial conditions are

$N(x, t) = 0$ Beginning condition

$N(0, t) = N_0$ Boundary condition

The solution of equation 4.9 for diffusion form a constant source is

$$N(x_0, t) = N_0\left(1 - erf\frac{x}{2\sqrt{Dt}}\right), \tag{4.10}$$

where $erf[x/2(Dt)^{1/2}]$ represents the error function with argument $y = x/2(Dt)^{1/2}$

$$erf(y) = \frac{2}{\sqrt{\pi}}\int_0^y \exp(-y^2)dy. \tag{4.11}$$

Here $N_0 = N(0,t)$ is the constant concentration on the surface of the sample, $N(x,t)$ is the impurity concentration at the distance x, D is the diffusion coefficient, and t is the diffusion annealing time [52].

CHAPTER 5

EXPERIMENTAL METHOD

5.1 Preparation of Superconducting $Bi_{1.8}Pb_{0.35}Sr_{1.9}Ca_{2.1}Cu_3O_y$

There are a number of variations on the general procedure for the preparation of ceramic superconductor, which are the solid-state reaction method, chemical routes, and novel preparation methods etc.

The solid-state reaction method is the most common preparation route for ceramic superconductors [53]. Superconducting $Bi_{1.8}Pb_{0.35}Sr_{1.9}Ca_{2.1}Cu_3O_y$ samples were prepared by the standard solid-state reaction method. For this method, the appropriate amounts of Bi_2O_3 (99.99%), PbO (99.9+%), $SrCO_3$ (99.9+%), $CaCO_3$ (99+%) and CuO (99+%) were mixed in the stoichiometric ratios of Bi:Pb:Sr:Ca:Cu = 1.8:0.35:1.9:2.1:3 compound were determined as fallows:

Element	Atomic Weight (au)
Bi	208.98
Pb	207.19
Sr	87.62
Ca	40.08
Cu	63.54
C	12.01
O	15.99

Table 5.1: Atomic weight and purity of the compounds.

Compound	Purity (%)	Atomic weight
Bi_2O_3	99,99	465,96
PbO	99,9	223,19
$SrCO_3$	99,9	147,63
$CaCO_3$	99+	56,08
CuO	99+	79,54

Therefore, the chemical equilibrium equation is written,

$$(0.9)Bi_2O_3 + (0.35)PbO + (1.9)SrCO_3 + (2.1)CaCO_3 + (3)CuO + \longrightarrow Bi_{1.8}Pb_{0.35}Sr_{1.9}Ca_{2.1}Cu_3O_{10} + \text{Gases}$$

From this equation, the quantities of reactants to produce approximately 20 grammas of unreacted compound shown in Table 5.2.

Table 5.2: The weight of the compounds for produce 20 grammas.

Compounds	Mass (gr)
Bi_2O_3	8.0809 gr
PbO	1.4646 gr
$SrCO_3$	5.2589 gr
$CaCO_3$	3.9407 gr
CuO	4.6235 gr

The mixed powders were calcined in air at 700, 750 and 800 ^{o}C for 24 h. At every calcined temperature, the sample cooled to room temperature to regrind (Figure 5.1). The calcined material was reground and pressed into pellets of 10x4x2 mm^3 at 300 MPa (Figure 5.2).

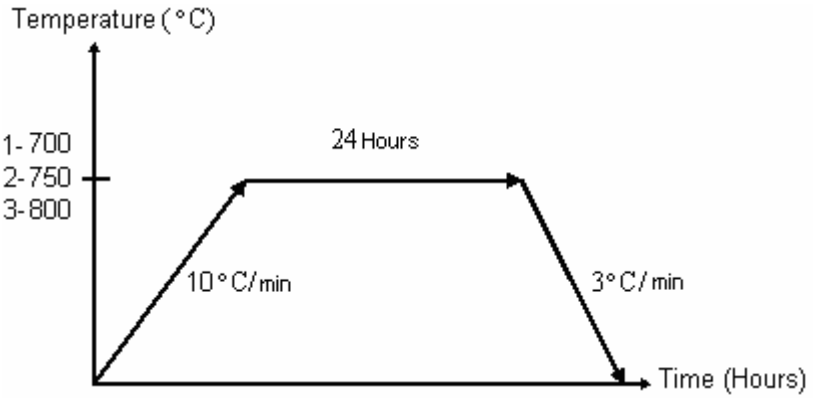

Figure 5.1: Calcinations process of the powder.

Figure 5.2: Photograph of the press.

The pellets were sintered in air at 830 ^{o}C for 48 h and then cooled down to room temperature. The heating and cooling rates of the temperature were chosen to be 10 and 3 ^{o}C min^{-1}, respectively (Figure 5.3).

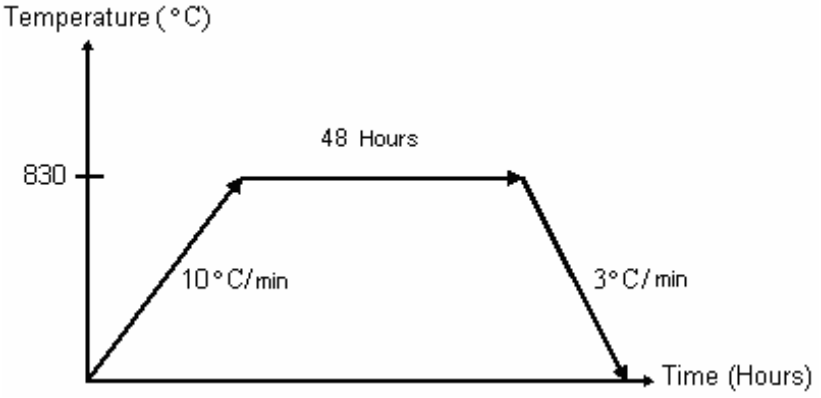

Figure 5.3: Sintering process of the samples.

The *Au* evaporation (thickness of about 50 μm) on one face of the samples was carried out using an AUTO 306 Vacuum Coater (EDWARDS) (Figure 5.4). Then, the Au layered superconducting samples were annealed at 830 ^{o}C for 10 h (*G1*), 20 h (*G2*) and 50 h (*G3*) and 800 ^{o}C (*G800*) ,750 ^{o}C (*G750*), 700 ^{o}C (*G700*), 600 ^{o}C (*G600*), 500 ^{o}C (*G500*) for 10 hours. At the end of this run, *Au* diffusion was realized through the samples. For comparison, undoped samples were also annealed under the same conditions. The diffusion annealing was performed in a programmable tube furnace from PROTHERM (Model PTF 12/75/200) (Figure 5.5). All of the annealing and evaporation process showed in Figure 5.6.

Figure 5.4: EDWARDS, AUTO 306 vacuum coater.

Figure 5.5: PROTHERM (Model PTF 12/75/200) programmable tube furnace.

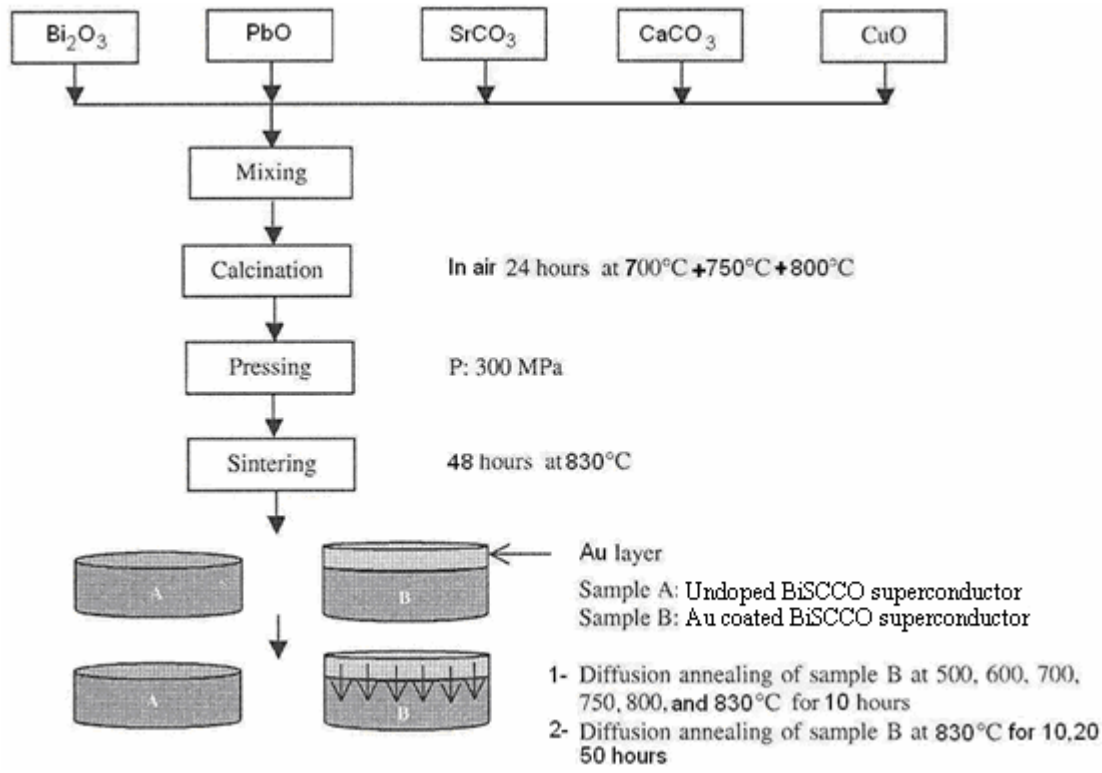

Figure 5.6: Schematic diagram of the all annealing and evaporation process.

5.2 X-Ray Diffraction Analysis

X-ray diffraction (XRD) data were taken using a Rigaku D/Max-IIIC diffractometer with CuK_α radiation in the range $2\Theta = 3°$- $60°$ with a scan speed of 3 °/min and a step increment of 0.02° at room temperature (Figure 5.7). The XRD measurements provide data about lattice parameters for only a thin surface layer of *Au*-diffused $Bi_{1.8}Pb_{0.35}Sr_{1.9}Ca_{2.1}Cu_3O_y$ sample, since the effective penetration depth of the x-rays is about 15 μm into the sample. Phase purity and the lattice parameters were determined these XRD patterns. The accuracy in determining the lattice parameter *c* was ± 0.001 Å. The mean values of lattice parameter *c* of $Bi_{1.8}Pb_{0.35}Sr_{1.9}Ca_{2.1}Cu_3O_y$ samples are determined from the high-angle (00*l*) peaks of the XRD measurements.

Figure 5.7: Rigaku D/Max-IIIC diffractometer.

5.3 SEM Analysis

The surface morphologies of the *Au*-diffused and pure samples were studied by using a Philips XL30 SFEG scanning electron microscope. SEM micrographs were taken from fracture surfaces of the bulk samples. Micrographs of the samples were magnified approximately 8000 times (in general 2 cm represents to 5 μm). We investigated microstructure of the sample, connection and size of the grains.

5.4 Resistivity Measurements

The low temperature DC electrical resistivity measurements were carried out by using OXFORD Edwards Model CS2/9 (Figure 5.8).

The measurements of DC resistivity were performed with the four-probe method on all samples (Figure 5.9). Both voltage and current contacts were made with silver paint, the contact resistance being in the order of 0.1 Ω or lower. Resistive contacts caused heating and the test was completed in possible shortest time to avoid extensiveness of this effect. We measured temperature (70 K-130 K) dependence of resistivity of the samples running 5 mA DC current through the samples in the cryostat.

Figure 5.8: OXFORD, Edwards Model CS2/9 cryogenic system.

A Keithley 220 programmable current source and a Keithley 2182A nano-voltmeter were used for the resistivity measurements. The transition temperature, T_c, was defined as R = 0. To convert voltage to resistivity the calculation is made as fallowing:

$$\rho = \frac{V\,l}{I\,A} \qquad (5.1)$$

where l is the distance between the inner electrical contacts, A is the cross-section of the sample.

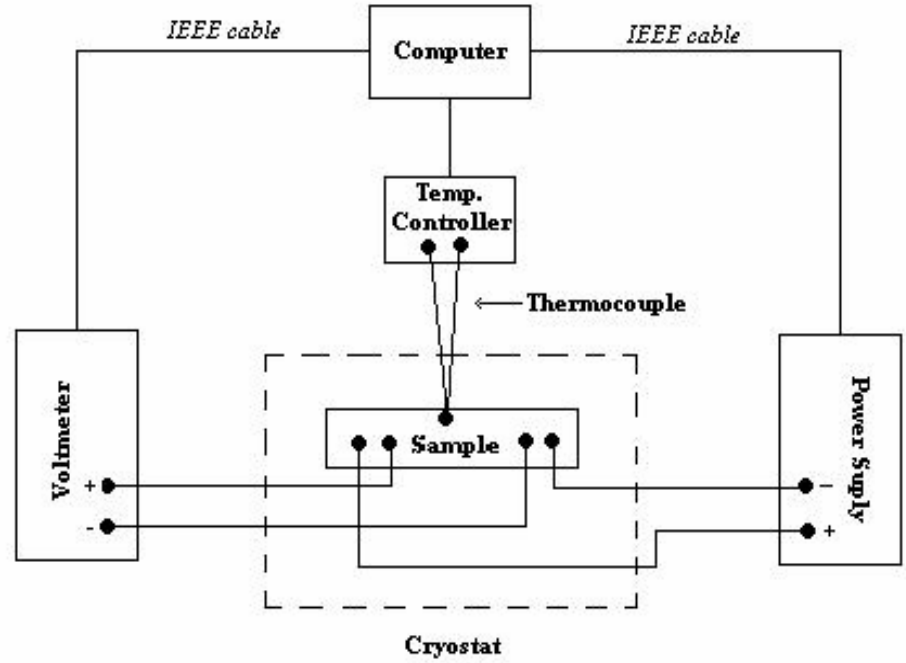

Figure 5.9: Schematic diagram of the four-probe method.

5.4.1 Description of The Resistivity Measurement System

The closed cycle cooler system includes the cryostat build on an Edwards model CS2/9 cold head, a water cooled compressor unit and integral control unit, a pair of flexible helium lines, and an intelligent temperature controller (ITC). The schematic diagram of the all cryogenic system is shown in Figure 5.10.

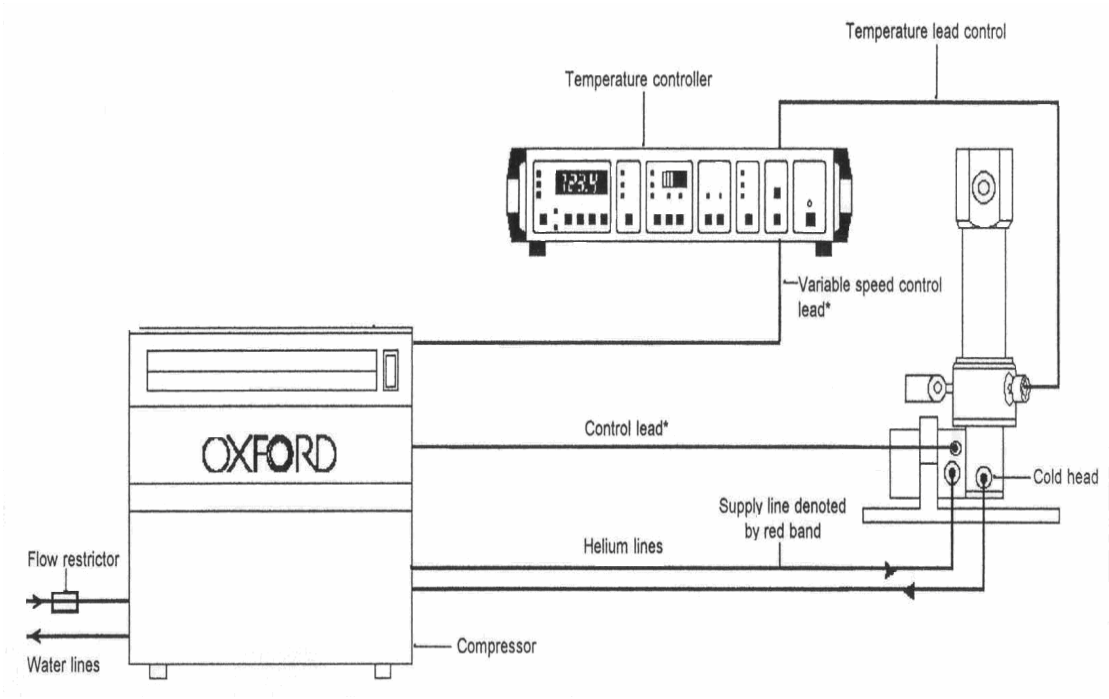

Figure 5.10: The schematic diagram of the cryogenic system.

Helium is compressed to 16.5 bar in the compressor and then expanded in controlled manner in the cold head to produce the cooling. The ITC not only controls the heater power to achieve stable control, but also adjusts the speed of the cold head to ensure that its speed is no higher than is necessary. This prolongs the life of the seals within the cold head.

The cold stage of the cold head is attached to a copper block, which contains a rhodium iron temperature sensor and two wire-wound resistor heaters to allow variable temperature operation. The sample holder is attached directly to this block. The schematic diagram of the cryostat with plain is shown in Figure 5.11.

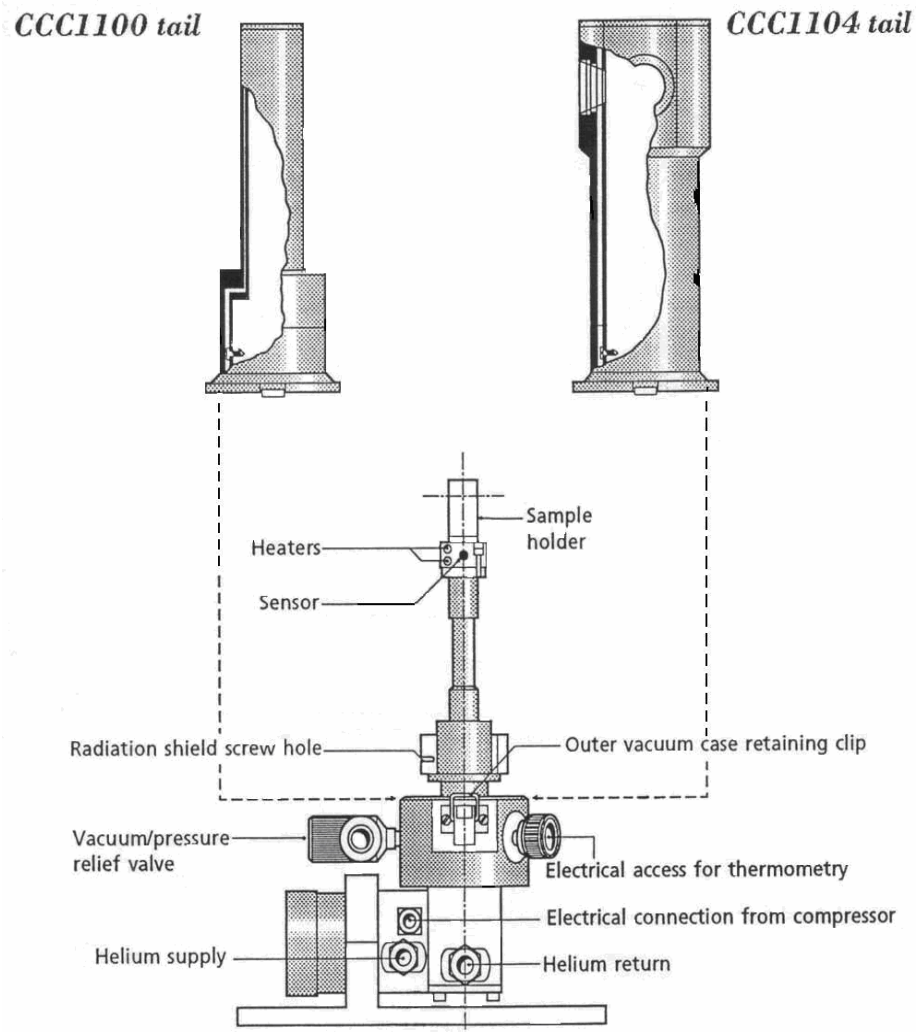

Figure 5.11: Schematic diagram of the vacuum loading cryostat with plain and optical tails.

The first stage of the cooler is connected to a copper radiation shield which extends upwards to shield the heat exchanger and sample holder from room temperature radiation.

An outer vacuum chamber (OVC), then surrounds the radiation shield to provide vacuum insulation for the cryostat. This space is pumped to a high vacuum before the cryostat is cooled down but it is protected against accidental build up of pressure by a relief valve.

5.5 Critical Current Measurements

The measurements of transport critical current density, J_c were performed with the four-probe method on all samples. The current was applied to the two outer electrical contacts and the voltage drops across the two inner electrical contacts were measured against current. Both voltage and current contacts were made with silver paint, the contact resistance being in the order of 0.1 Ω or lower. We determined J_c from the *I-V* curves at 77 K, the criterion for critical current was 1 μV/cm. Resistive contacts caused heating and the test was completed in possible shortest time to avoid extensiveness of this effect. A PCE Power Control GEN1500 programmable current source and a Keithley 2700 Multimeter were used for the *I-V* measurements. The schematic diagram of critical current measurement system is shown in Figure 5.12.

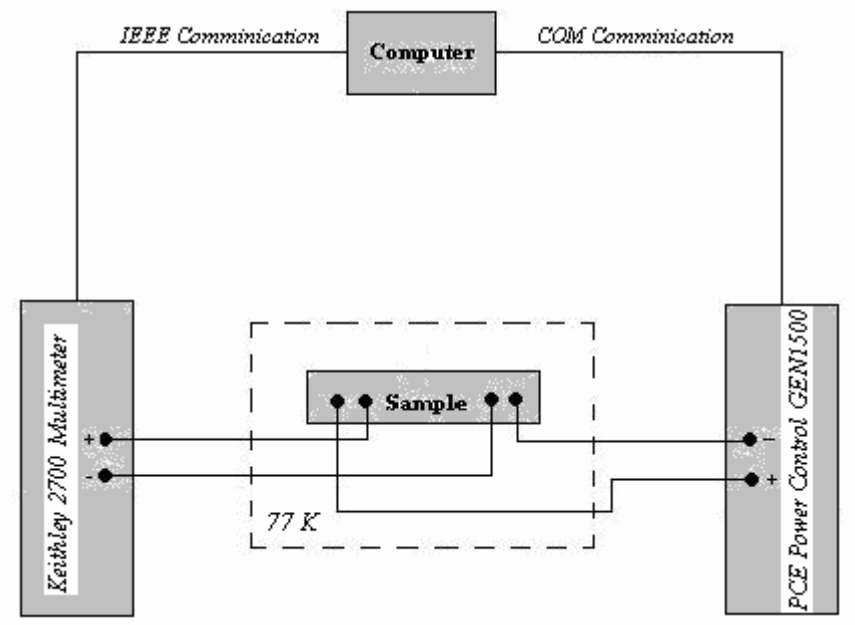

Figure 5.12: The schematic diagram of critical current measurement system.

5.6 Magnetoresistivity Measurements

We measured temperature (70-130 K) and DC magnetic field (0-0.5 T) dependent of resistivity of the samples with 5 mA DC current in a cryostat. The magnetic field was applied parallel to the current direction. The external dc magnetic fields for resistivity measurements were provided by an electromagnet. The transition temperature T_c was determined as the temperature at zero resistivity. Megnetoresistivity measurement system is shown in Figure 5.8.

5.7 AC Magnetic Susceptibility Measurements

AC magnetic susceptibility has become a popular technique over the recent years and its measurement allows determination of some useful superconducting properties of superconductors. It is an inductive and noncontactless measurement that involves screening currents flowing in the entire volume of the sample. Although there is a vast amount of work in the literature [54-57] on the magnetic response of high temperature superconductors (HTSCs), the interpretation of AC susceptibility is model dependent and there are some controversial issues concerning the occurrence of the peak in the out-of-phase component of the susceptibility. Müller *et al.* [58], Malozemoff *et al.* [59] and others have suggested that the peak in χ_1'' can be monitored to determine a so called 'irreversibility line' which separates the regions of reversible from irreversible magnetic behaviour. However, a non-zero value in χ_1'' would imply a hysteretic behaviour in magnetization [60]. Therefore, measurements at low dc bias fields and large drive amplitudes need to be considered in some detail for clear interpretation of AC susceptibility, where the temperature and field dependences

include contributions from flux line lattice dynamics [61–63]. For any conducting material exhibiting magnetic response to an alternating field $H_m \cos(n\omega t)$ the AC magnetization can be written as

$$M(t) = H_0 \sum_n \left(\chi_n' \cos(n\omega t) - \chi_n'' \sin(n\omega t) \right) \tag{5.2}$$

where χ_n' and χ_n'' are the in-phase and out-of-phase components of the harmonic susceptibilities with n = 1, 2, 3… For materials exhibiting a linear response, higher harmonics are not generated and only the fundamental harmonic susceptibility is dominant to describe the magnetic behavior. However, HTSC materials are well known to exhibit a hysteretic M–H magnetic response. Therefore, higher harmonics play a crucial role [64, 67] and their contribution to the total magnetic response should be considered in the vicinity of T_c.

For a single-phase type II superconductor exhibiting hysteretic magnetization, with no extrinsic flux pinning mechanism, the fundamental AC susceptibility normally shows a significant drop in the real part χ_1' as the temperature is lowered below T_c and a corresponding peak in the imaginary part of the susceptibility, χ_1''. The drop in χ_1' just below T_c is associated with flux exclusion from the interior of the superconductor, which indicates a measure of diamagnetic character, while the peak in χ_1'' is associated with AC losses. Hence, the out-of-phase component is a measure of the losses within the superconductor. As is well known, AC losses in a superconductor can be of two types, namely bulk pinning and eddy current losses. Bulk pinning losses are in general hysteretic and dominant in describing Ac behavior at sufficiently low frequencies, while eddy current losses are negligible provided that flux motion in the

mixed state does not contribute to a finite but very small resistivity of the material within the AC cycle of the measurement. Normally bulk pinning losses are independent of frequency but dependent on the field, while eddy current losses depend on the frequency and are independent of the field. In a real superconductor with a strong pinning mechanism, where there is an irreversible motion of flux lines, a critical state model [65] can be considered as valid at low frequencies approaching the dc limit. However, at sufficiently high frequencies the skin depth δ associated with flux sweeping in and out of the sample becomes comparable with the sample size and the critical state model is no longer valid. In the latter, χ_1'' peaks at $\delta = a$ for a cylinder with radius a, while the critical state model assumes that χ_1'' peaks at a field for which the full flux penetration to the centre of sample occurs. However, these idealized approaches may well be too simplified to describe the AC susceptibility of HTSCs that may exhibit additional peaks in χ_n'' due to various intrinsic and extrinsic pinning mechanisms, structural disorder and crystal defects. In a real superconductor, an interplay of these various loss mechanisms should also be considered, but this is a complicated task as the losses are not simply additive [68].

The AC magnetic susceptibility as a function of temperature was measured by means of a Lake Shore 7130 AC susceptometer in the temperature range 40–120 K in a magnetic field of 20-320 A/m and 111 Hz frequency (Figure 5.13). The sample, kept in helium exchange gas with a controllable temperature resolution better than 10 mK, was moved from the centre of one secondary coil to the other to eliminate unwanted signals and to maximize the signal from the sample itself. The AC field was applied parallel to the long axis of the sample. For AC susceptibility measurements automatic data acquisition was selected, while magnetization was measured manually in order to adjust the phase angle correctly for the measurement frequencies. The phase angle

was chosen so that ΔM = 0 at ac field crossing and χ_1'' was also zero a low temperatures. Schematic Diagram of the AC susceptibility system is shown in Figure 5.14.

Figure 5.13: Lake Shore AC susceptometer 7130.

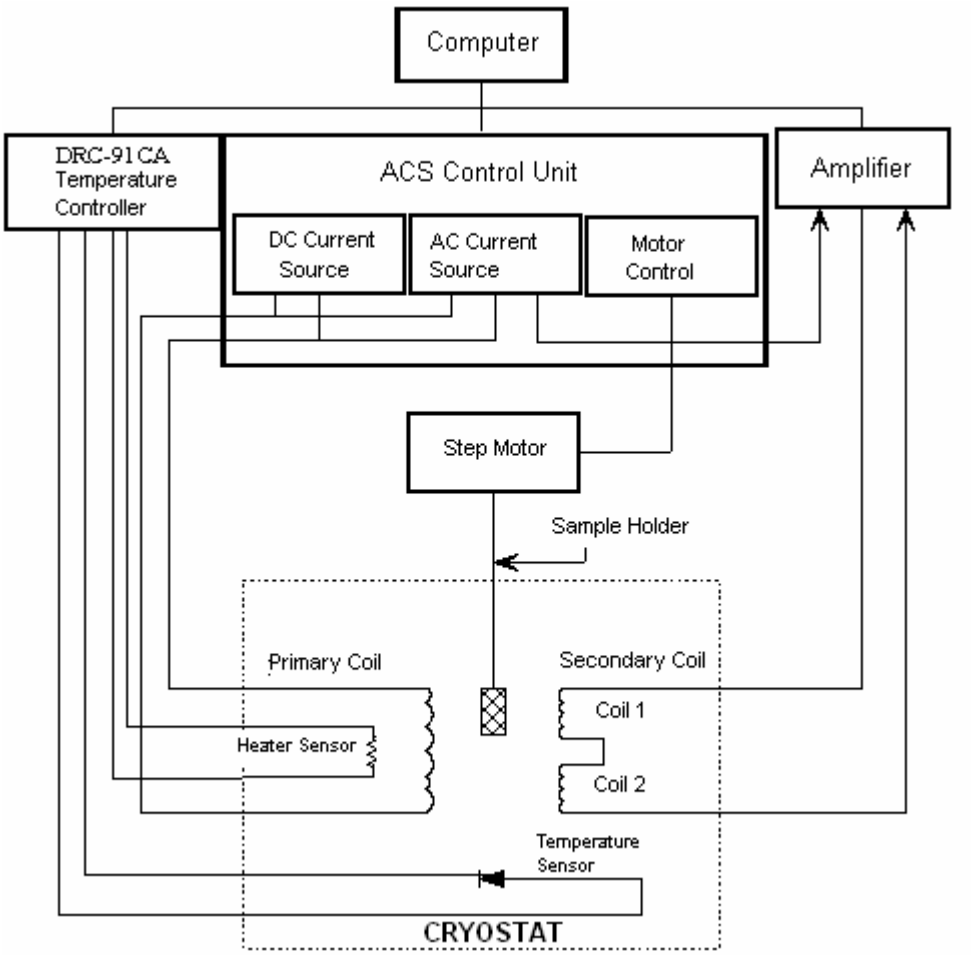

Figure 5.14: Schematic diagram of the AC susceptibility system [47].

5.8 Hardness Measurements

Many studies of doping into superconductor oxide ceramics have been made in order to improve their mechanical and superconducting properties [13, 31, 69-72]. Engineering applications of high critical temperature (T_c) superconducting ceramics are generally restricted because of their brittleness. Therefore, improvement of the mechanical properties of *BSCCO* is a major research objective and very important for their practical applications and high performance such as quasi-permanent magnets and current leads. Hardness is a mechanical parameter and it is strongly related to the structure and composition of solids. There are several methods to estimate the

hardness values in polycrystalline high-T_c superconductors. The most common methods are: Vickers, Brinnel, Knopp, and Rockwell. The Vickers microhardness test is one of the convenient methods to estimate the mechanical properties.

5.8.1 Vickers Hardness Measurements

Hardness measurements of *BSCCO* samples were performed with a digital microhardness tester (Instron Series 2100) at room temperature. A Vickers pyramidal indenter with different loads (0.245, 0.490, 0.980, 1.960, and 2.940 N) and a single loading time of 10 s were applied and the diagonals of indentation were measured with an accuracy of ± 0.1 μm. Indentations were made at different parts of the samples' surface in such a way that the distance between any two indentations was no less than two times the diagonal of the indentation mark to avoid surface effects due to neighboring indentation. An average of 10 readings at different locations of specimen surfaces was taken to obtain reasonable mean values for each load. Schematic diagram of the Vickers microhardness measurement system is shown in figure 5.15

The Vickers microhardness (load dependent) values of different applied loads were calculated by using the equation,

$$H_v = 1854.4\left(F/d^2\right) \quad (GPa) \tag{5.3}$$

where F is the applied load in N and d is the diagonal length of the indentation mark in μm ($d=(d_1+d_2)/2$).

In most materials, the elastic modulus (Young's modulus), E, is related to the bulk hardness by the relation [73]

$$E = 81.9635 H_v, \tag{5.4}$$

and yield strength Y is related to the hardness by the relation [74, 75]

$$Y \approx H_v / 3. \tag{5.5}$$

It is useful to mention the fracture toughness, K_{IC}, as it is one of the main mechanical properties of superconducting samples. The fracture toughness is an important parameter for the selection of materials for applications. Due to the nature of intrinsic brittleness, microindentation may result in microfracture around the impressed region on the surface of the samples [76]. Since microfracture occurs mainly during the loading a portion of the energy, which is used to create the indentation deformation, will be dissipated by the crack formation. Owing to the definition of the K_{IC} as the critical stress intensity factor, it is directly related to γ (the surface energy) of the crack faces [77]

$$K_{IC} = \sqrt{2E\gamma}. \tag{5.6}$$

where E is the Young's modulus.

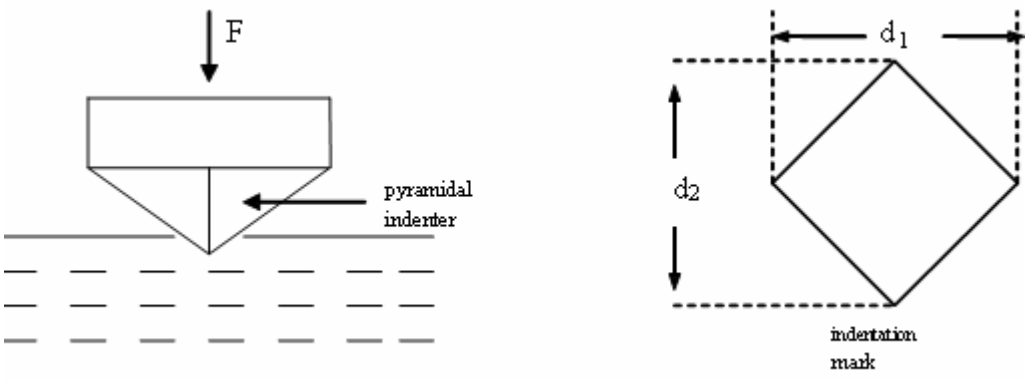

Figure 5.15: Schematic diagram of the Vickers microhardness measurement system.

CHAPTER 6

RESULTS AND DISCUSSIONS

6.1 Introduction

The noble metals such as *Ag* and *Au*, in the same column as copper in the Periodic Table, are of special interest for the high temperature superconductors [31]. There is a tremendous amount of work on *Bi(Pb)-Sr-Ca-Cu-O* system since its discovery. To improve the superconducting properties, partial substitution and diffusion have been investigated extensively [9, 16, 17, 24, 78-81]. O. Gorur et al. [27, 82] investigated the effect of *Ag* diffusion on properties of $YBa_2Cu_3O_{7-x}$ thin films produced by electron beam deposition techniques and bulk samples. They found that, for *Ag*-doped sample, T_c and J_c were increased while the room temperature resistivity values were decreased in comparison with those of undoped *YBCO*. The researchers found that *Ag* addition in *BSCCO* system enhances J_c [19, 20], improves T_c [21, 22], mechanical properties and electrical stability [23]; and reduces the normal-state resistivity, and the contact resistance [22, 28]. On the other hand, it was observed that *Au* addition degraded the superconductivity of *Bi(Pb)-Sr-Ca-Cu-O* [28]. In contrary, it was also found that the *Au* addition did not affect on T_c and lattice parameters [29] and the gold addition did not affect the formation of the *Bi-2223* [30]. Therefore, there has been a contradicting about gold addition. It could be observed that in all of the

investigations, the gold addition of *Bi(Pb)-Sr-Ca-Cu-O* was carried out in the mixed powders before pressing and sintering of pellets. Dzhafarov et al. [31] reported the effect of *Au* diffusion combined with slow and fast cooling on T_c and J_c in *Bi(Pb)-Sr-Ca-Cu-O* system. It was observed that the gold-diffusion doping of *Bi(Pb)-Sr-Ca-Cu-O* at the sintering process with a fast cooling promotes formation of the high-T_c *Bi-2223* phase and significantly increases J_c.

The diffusion coefficients of gold may be useful for the understanding of doping mechanism and changes of microstructure and superconducting properties of *BSCCO* systems under doping. To our knowledge, no detailed work on the calculation of the *Au* diffusion coefficient in a *Bi(Pb)-Sr-Ca-Cu-O* bulk sample has been published in the literature.

The gold diffusion parameters in $Bi_{1.8}Pb_{0.35}Sr_{1.9}Ca_{2.1}Cu_3O_y$ have been studied over the temperature range of 500-830$^\circ C$ using the two different techniques. The diffusion coefficient is calculated using the technique of successive removal of thin layers and measurement of the sample's resistivity at room temperature, and also, calculation of the lattice parameter *c* from XRD patterns at room temperature.

The mechanical properties such as hardness, elastic modulus, yield strength, fracture toughness, brittleness index, ductility, etc. are as important as the superconducting parameters for industrial applications like quasi-permanent magnets and current leads. Regarding mechanical properties, hardness test provides useful information on the strength and deformation properties of the materials. Microhardness is not only a routinely measured mechanical characteristic; it has also been developed as an investigation method of structural parameters.

In this thesis, we have investigated the effect of the gold-diffusion, and diffusion-annealing duration on the microstructure, superconducting and mechanical

properties of *Bi-2223* superconducting samples employing X-ray diffraction (XRD), scanning electron microscopy (SEM), critical transition temperature, critical current density, AC susceptibility, microhardness, and room temperature resistivity measurements.

6.2 X-ray Diffraction Characterizations

The samples of *Bi-2223* pellets will be hereafter denoted as *G0* (undoped sample annealed at 830 $^{\circ}C$ for 10 h), *G1* (gold diffused sample annealed at 830 $^{\circ}C$ for 10 h), *G2* (gold diffused sample annealed at 830 $^{\circ}C$ for 20 h), and *G3* (gold diffused sample annealed at 830 $^{\circ}C$ for 50 h).

The x-ray powder diffraction patterns from the surface of the *G0, G1, G2* and *G3* samples are shown in Figure 6.1. Some of the Miller indices are indicated in the figure. We used the linear least squares method to calculate the lattice parameters of the samples. The determined lattice parameters from the *(00l)* peaks of the XRD data are given in Table 6.1.

The *Au* doping (*G1*) increased the *c*-parameter and the intensity of the peaks, and decreased the *a*-parameter of the sample in comparison with that for the undoped sample (*G0*).

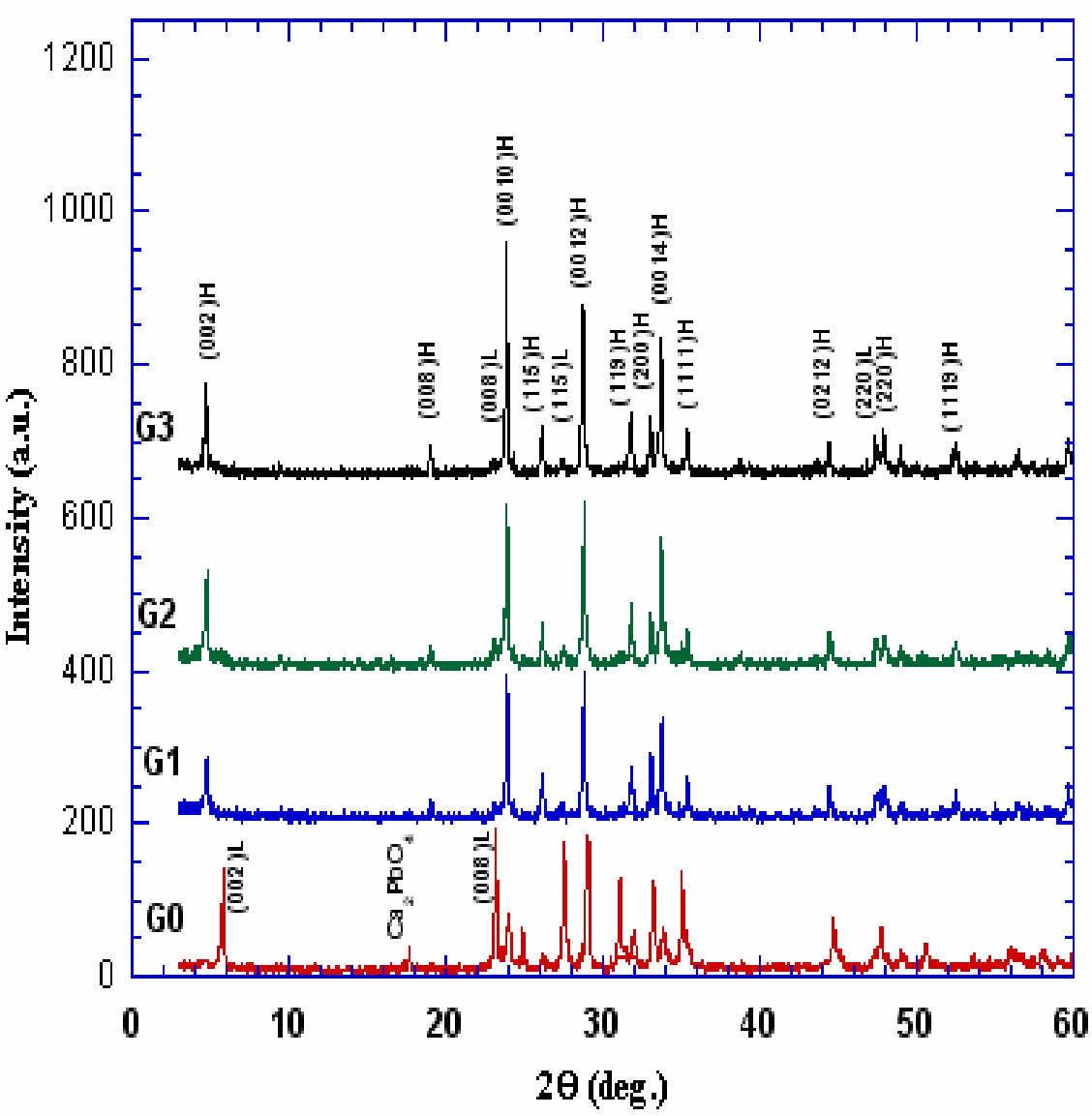

Figure 6.1: XRD patterns from the surface of the *G0, G1, G2,* and *G3* samples.

The increase in the intensities of the peaks for the *G1* sample may testify to the enhanced grain growth and orientation of grains with *Au* diffusion, causing the critical current density increase as will be confirmed by critical current density measurements in the current study. It was observed that the *c*-parameter increased with further increasing the diffusion-annealing time (20 and 50 h). Our measurements showed an increase of the *c*-parameter by about 0.13%. We used this information to calculate the diffusion coefficient of *Au*. The increase in the *c*-parameter indicated that cations of

the system (Bi^{+3}, Sr^{+2}, Ca^{+2}) may partly be substituted by *Au* ions (0.85 Å). Substitution at the *Cu* site is less likely because we have observed that T_c of the samples has increased [83].

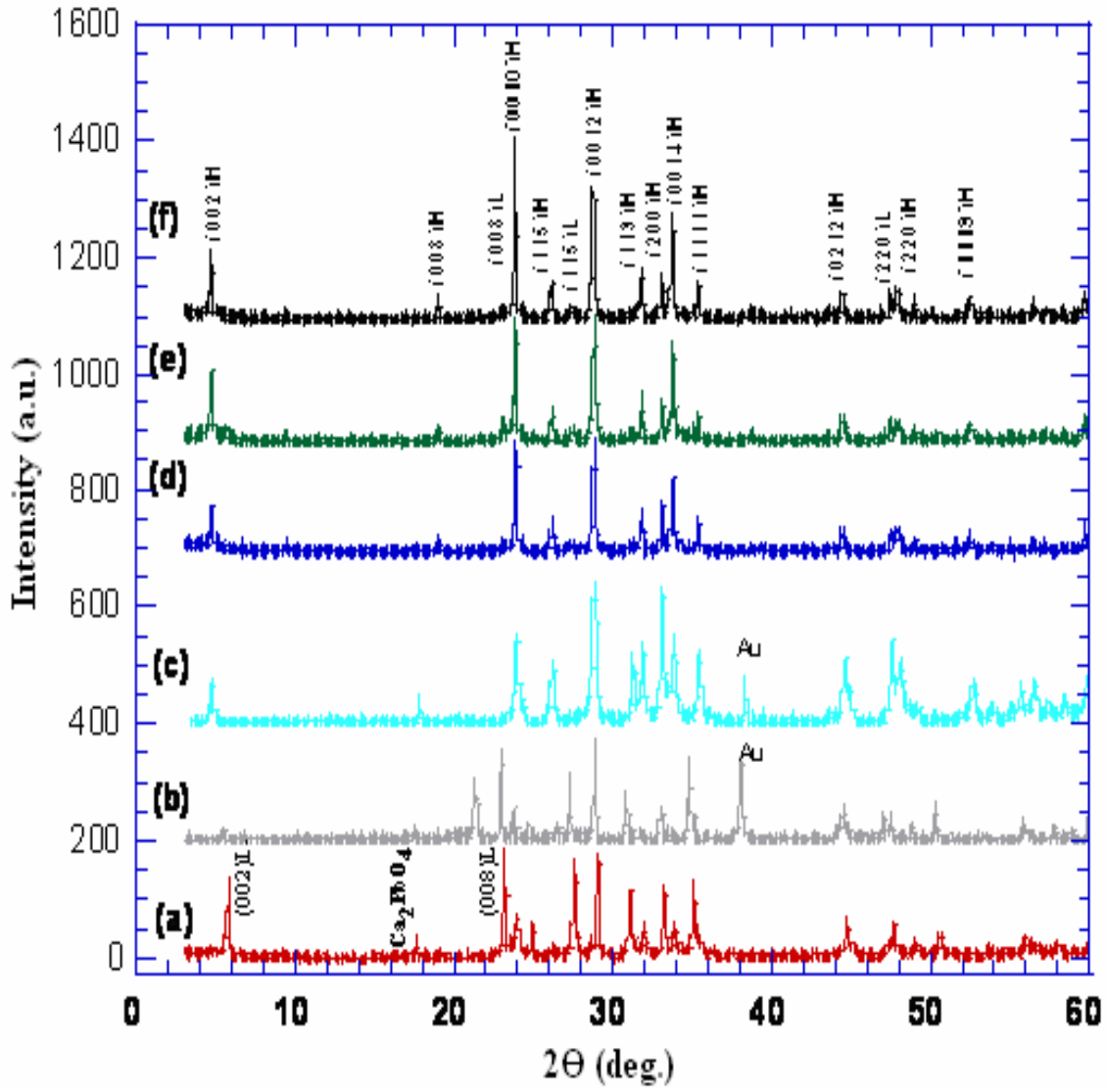

Figure 6.2: (a) The powder XRD pattern of sample *G0*, **(b)** XRD pattern taken from the surface of the *Au*-covered bulk sample before grinding and annealing, **(c)** XRD pattern taken from the surface of the bulk sample *G1* before grinding (annealed), **(d)** powder XRD pattern of sample *G1*, **(e)** powder XRD pattern of sample *G2* and **(f)** powder XRD pattern of the sample *G3*. The peaks indexed *(hkl)L* and *(hkl)H* represent the *Bi-2212* and *Bi-2223* phases, respectively.

XRD peaks due to *Au* is not seen in the powder XRD patterns of the diffusion-doped samples (Fig. 6.2(d)) although it was seen in the XRD patterns taken from the surface of the bulk samples prior to grinding in about 2Θ = 38.32° (Fig. 6.2 (c)). We compared the lattice parameter *c* of sample *G1* calculated from sample's surface (37.100 Å) and from powder (37.030 Å). It was found that the lattice parameter *c* is larger at the surface. This result implies that *Au* is incorporated into the structure from the surface by diffusion. In the *G1* sample, (*002*)*L* and Ca_2PbO_4 peaks are absent but that impurity phase and (*002*)*L* peaks are present in *G0* sample. *Au* doping (*G1*) increased the *c*-parameter and intensity of the peaks, and decreased the *a*-parameter of the sample in compression with that for the undoped sample (*G0*). The increase in the intensities of the peaks for the *G1* sample may testify to the enhanced grain growth and better orientation of grains with *Au* diffusion.

The relative volume fractions of the *Bi-2223* and *Bi-2212* phases were determined from the peak intensities of the same particular reflections, using the following well-known expressions [84, 85];

$$f_{(2223)} = \frac{\sum I_{H(hkl)}}{\sum I_{H(hkl)} + \sum I_{L(hkl)}} \tag{6.1}$$

$$f_{(2212)} = \frac{\sum I_{L(hkl)}}{\sum I_{H(hkl)} + \sum I_{L(hkl)}} \tag{6.2}$$

Here $I_{H(hkl)}$ and $I_{L(hkl)}$ are the intensities of the *(hkl)* diffraction lines for *Bi-2223* and *Bi-2212* phases, respectively (Fig.6.1). The calculated relative volume fraction of the samples is listed in Table 6.1. As seen in the table, with *Au* diffusion, the volume fraction of *Bi-2223* phase increased and that of *Bi-2212* phase decreased. The

diffusion doping sample by gold improves formation of the high-T_c *Bi-2223* phase in comparison with undoped sample.

Table 6.1: Lattice parameter *a*, and *c*, and volume fractions of *G0, G1, G2,* and *G3* samples.

Samples	**Lattice parameter *a* (Å)**	**Lattice parameter *c* (Å)**	***Volume fractions (%)***	
			2212	***2223***
G0	5.431	36.960	34	66
G1	5.430	37.030	15	85
G2	5.390	37.190	11	89
G3	5.382	37.206	8	92

6.3 SEM Investigations

The samples produced are named as *G830, G800, G750, G700, G600,* and *G500* (gold diffused samples annealed at 830, 800, 750, 700, 600 and 500 $^{\circ}C$ for 10 h, respectively), *P830, P800, P750, P700, P600, P500* (pure samples annealed at 830, 800, 750, 700, 600 and 500$^{\circ}C$ for 10 h, respectively).

The structure of surface morphology of the *Au* doped *Bi(Pb)-Sr-Ca-Cu-O* samples was studied by SEM in order to determine the grain sizes and possible precipitation at the grain boundaries. Figure 6.3 (a-d) represents surface micrographs for the *G0*, *G1, G2,* and *G3* samples. The grain size of the *G3* sample is relatively bigger than that of the other samples (*G1, G2*) especially *G0* sample, it is apparent from Figure 6.3 although we have not carried out conclusive quantitative analysis.

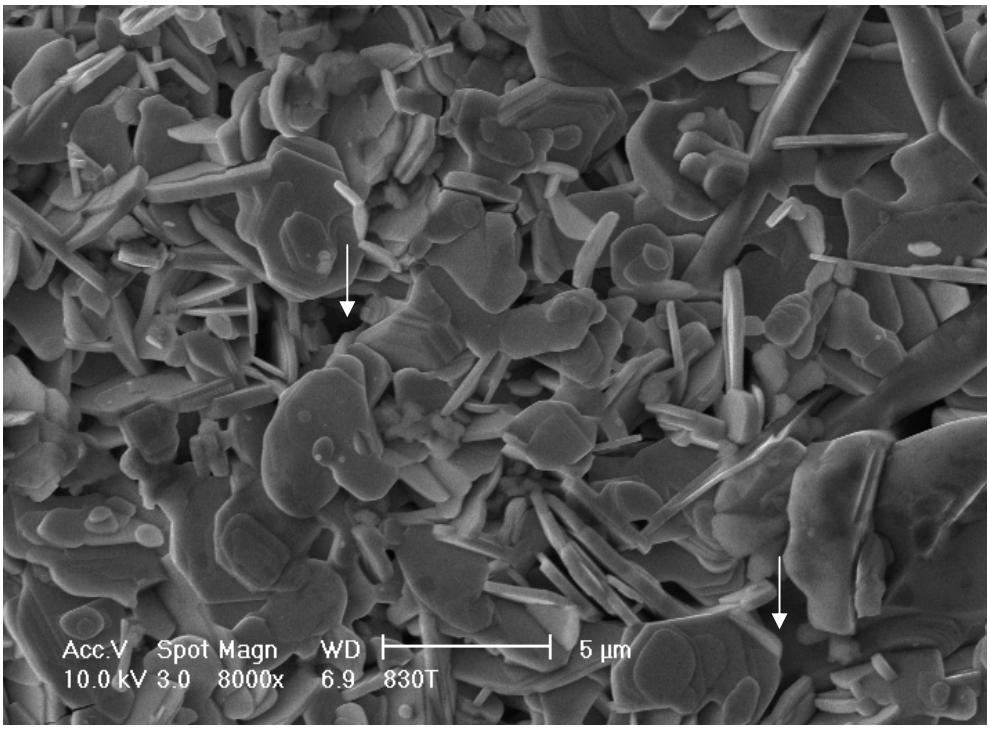
Acc.V Spot Magn WD 5 µm
10.0 kV 3.0 8000x 6.9 830T

(a)

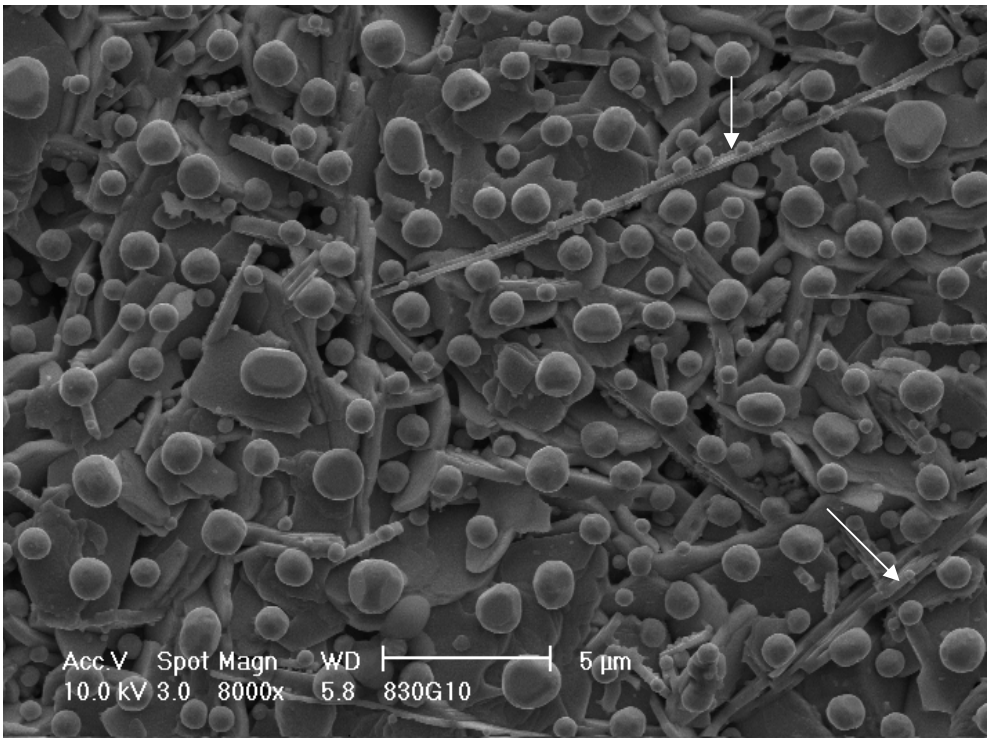
Acc.V Spot Magn WD 5 µm
10.0 kV 3.0 8000x 5.8 830G10

(b)

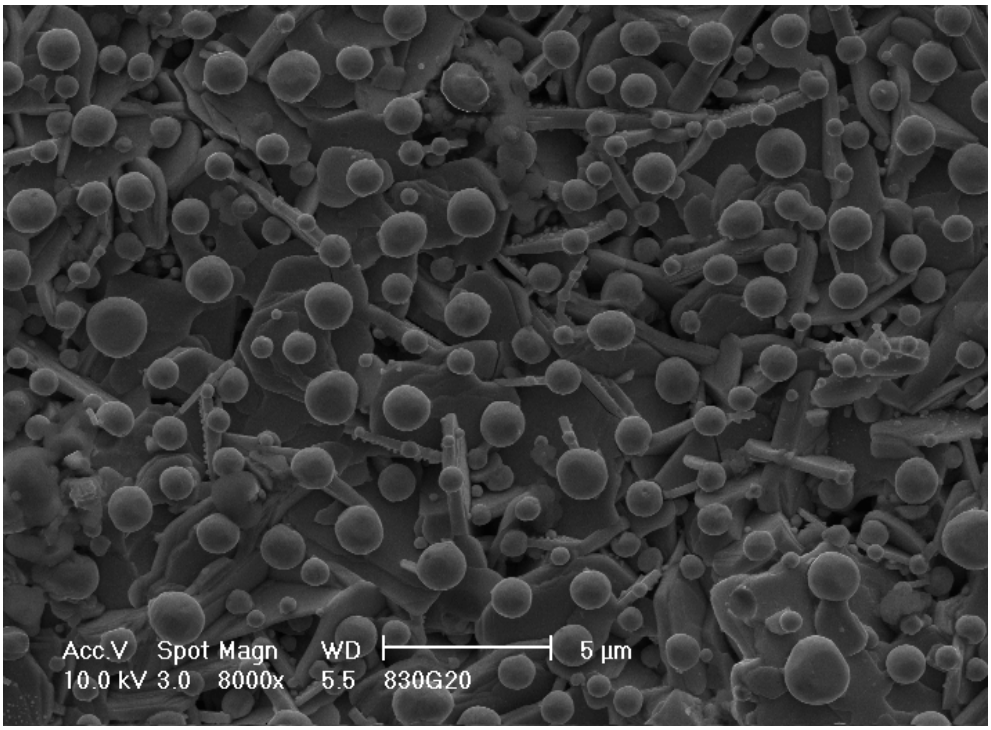

(c)

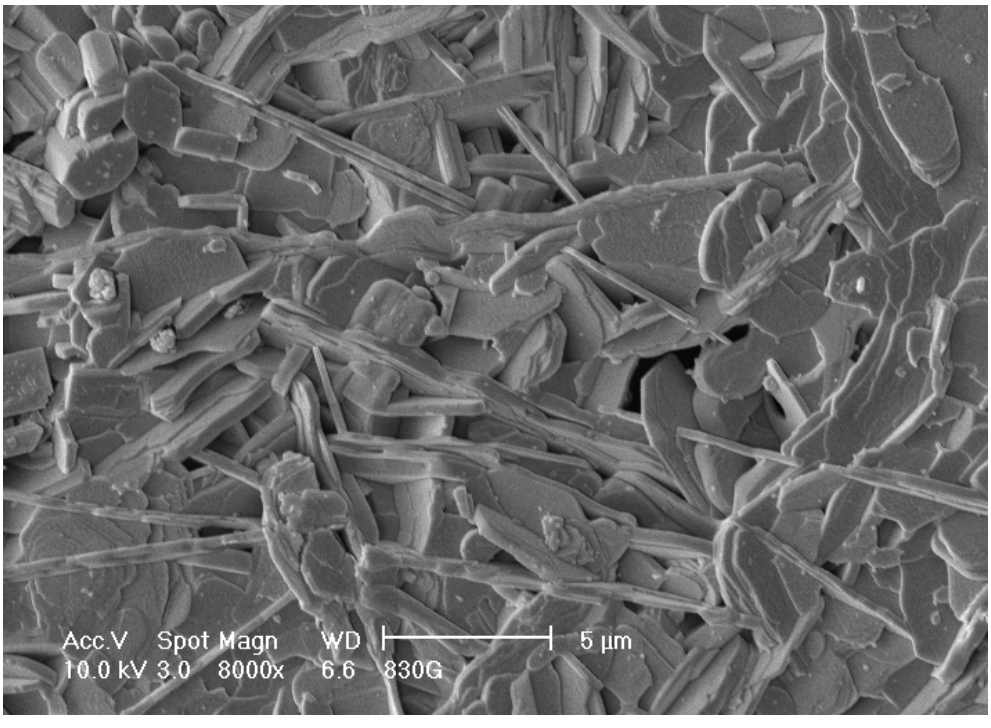

(d)

Figure 6.3: SEM micrographs of the samples **(a)** *G0*, **(b)** *G1*, **(c)** *G2*, and **(d)** *G3*.

The surface of the *G3* sample is also smoother and denser and the grains are longer than other samples**.** Moreover, grain size of gold doped samples improved with longer annealing times. When we comparison with *G0* and *G1* samples, also we can say the grain size of the *G1* sample is relatively bigger than that of the other sample *G0*, the surface of the *G1* sample is also smoother and denser. Arrows on the SEM pictures indicate longer grains and voids. Tiny spherical objects on the surface of micrograph shown in Figure 6.3 (b-c) are gold particles. They are absent in the micrograph shown in Figure 6.3 a. These micrographs show us that gold remains on the sample's surface after 10 h heat treatment. These spherical gold particles are absorbed in the sample when the duration of heat treatment is increased to 50 hours.

The *G0* sample consists of flake-type grains as shown in Figure 6.3 and the composition of flake-type grains is approximately equal to the *Bi-2212* phase [70, 86]. From the figure, one can say that the grains in the *G0* sample are oriented randomly and poorly connected. The flake-like grains are less dominant in sample *G1* with respect to sample *G0*, while the concentration of the needle-like grains grew gradually. The needle-like grains are believed to be due to the *Bi-2223* phase [70, 86, 87]. These results indicate that the surface morphology of the sample is relatively improved by *Au*-doping.

These results indicate that the surface morphology of the sample is relatively improved by *Au*-doping. *G0* has non-uniform surface appearance with smaller grains. SEM pictures of the surface of the samples annealed at lower temperatures present completely different morphology. For instance sample annealed at 800 ^{o}C has small spheres of gold particles disrupting the uniform film appearance, which was observed when the 500 ^{o}C-annealed sample was examined. This finding also shows that diffusion of gold at 800^{o}C is much slower than in the case of 830 ^{o}C heat treatment.

Gold film on the sample forms a metallic connection; this resistive short-circuit connects the grains and lowers the room temperature resistivity. This effect continues even when gold film is diffused in to the sample, indicating the gold's effect on grain boundary properties. SEM pictures show better connectivity in gold coated samples after heat treatment at 830 ^{o}C for 10 h.

Figure 6.4 (a-d) represents SEM micrograhps on the surface of the samples *G800, G700, G600* and *G500.* SEM pictures of the surface of the samples annealed at lower temperatures (500, 600, 700, 800 °C) present completely different morphology. We can say smoother and denser surface morphology for G500 (500°C) and G800 (800°C) samples with increasing diffusion-annealing temperature. Grain size and alignment of gold doped samples improved with higher diffusion-annealing temperature.

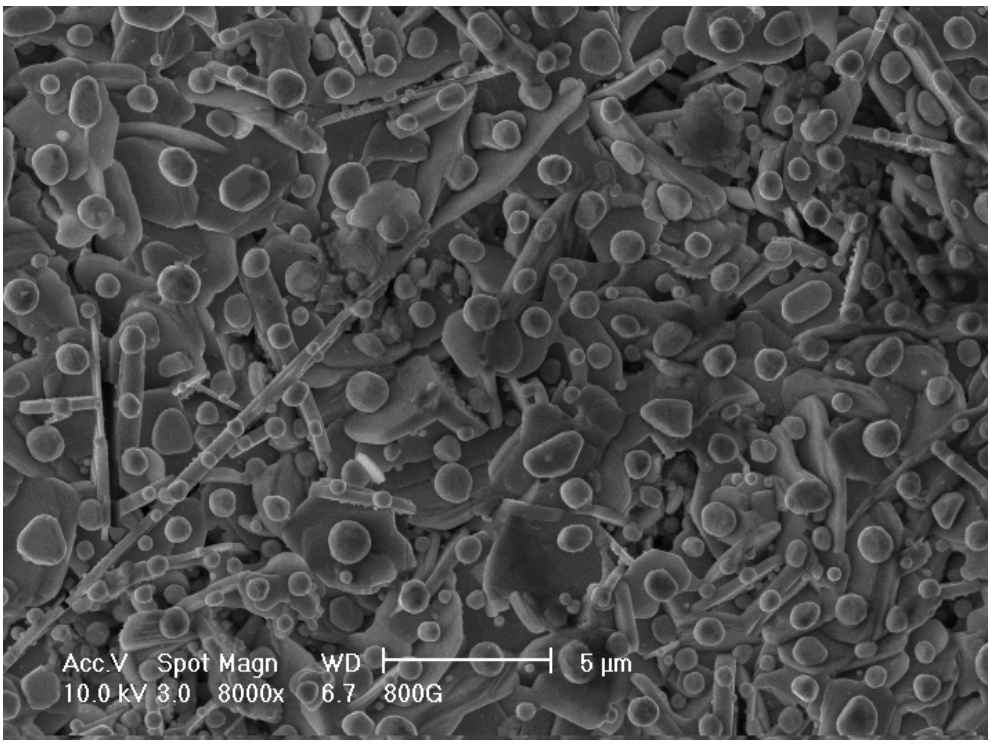

(a)

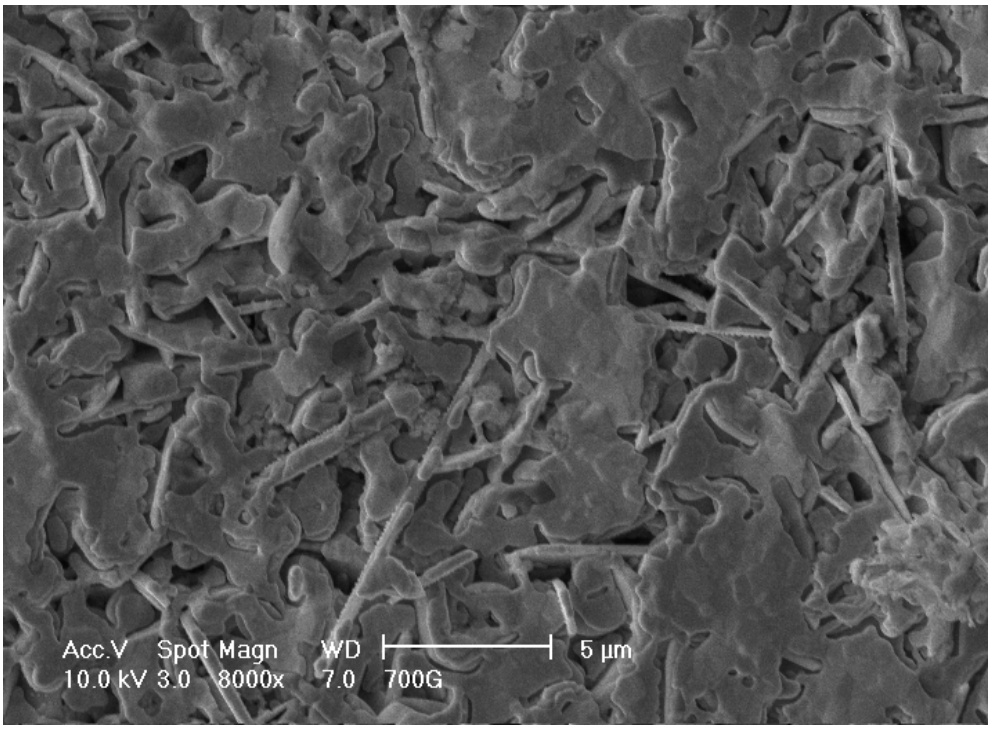
Acc.V Spot Magn WD 5 µm
10.0 kV 3.0 8000x 7.0 700G

(b)

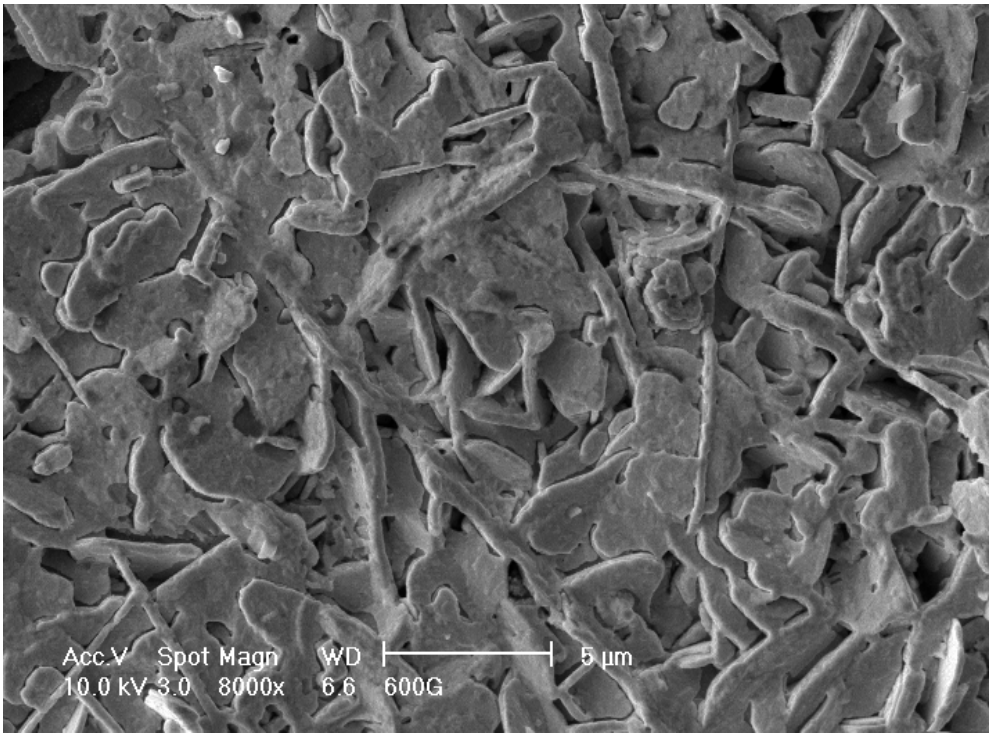
Acc.V Spot Magn WD 5 µm
10.0 kV 3.0 8000x 6.6 600G

(c)

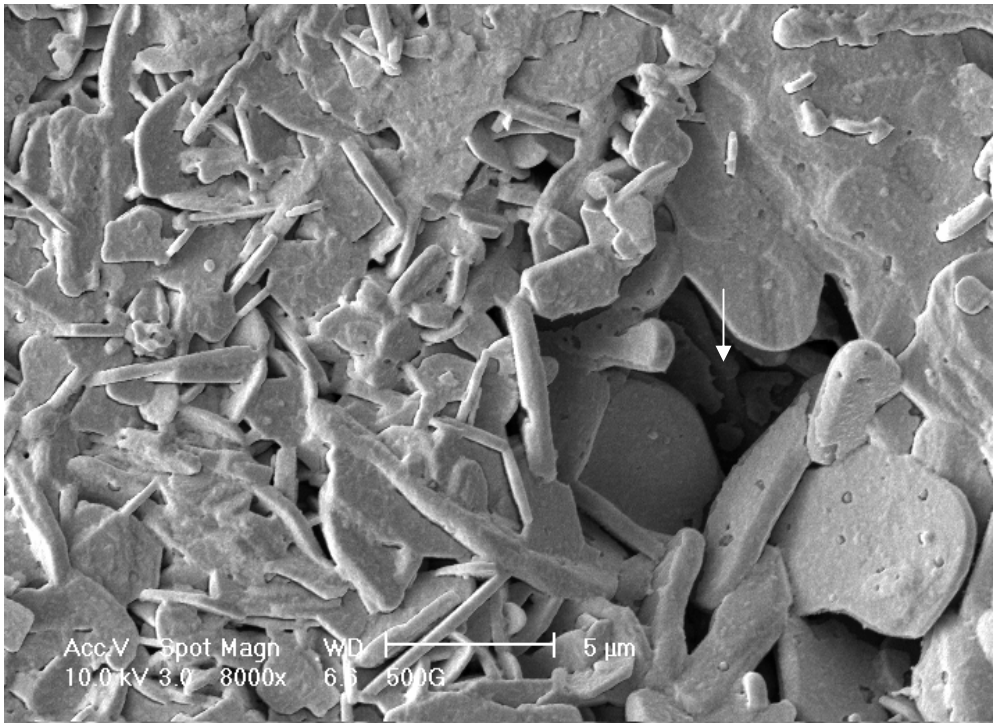

(d)

Figure 6.4 : SEM micrographs of samples **(a)** *G800*, **(b)** *G700,* **(c)** *G600* and **(d)** *G500.*

6.4 Resistivity Measurements

The electrical resistivity was measured using the standard four-probe dc technique, in the temperature range between 70 and 130 K with DC current of 5 mA. The temperature dependence of resistivity and normalized resistivity for *G0, G1, G2* and *G3* samples are shown in Figure 6.5 (a-b). The temperature dependence of the resistivities of the samples shows the metallic behaviour (at $T \geq 110\,K$) with the zero-resistivity transition temperatures of 100 K, 104 K, 105 K and 106 K**,** respectively.

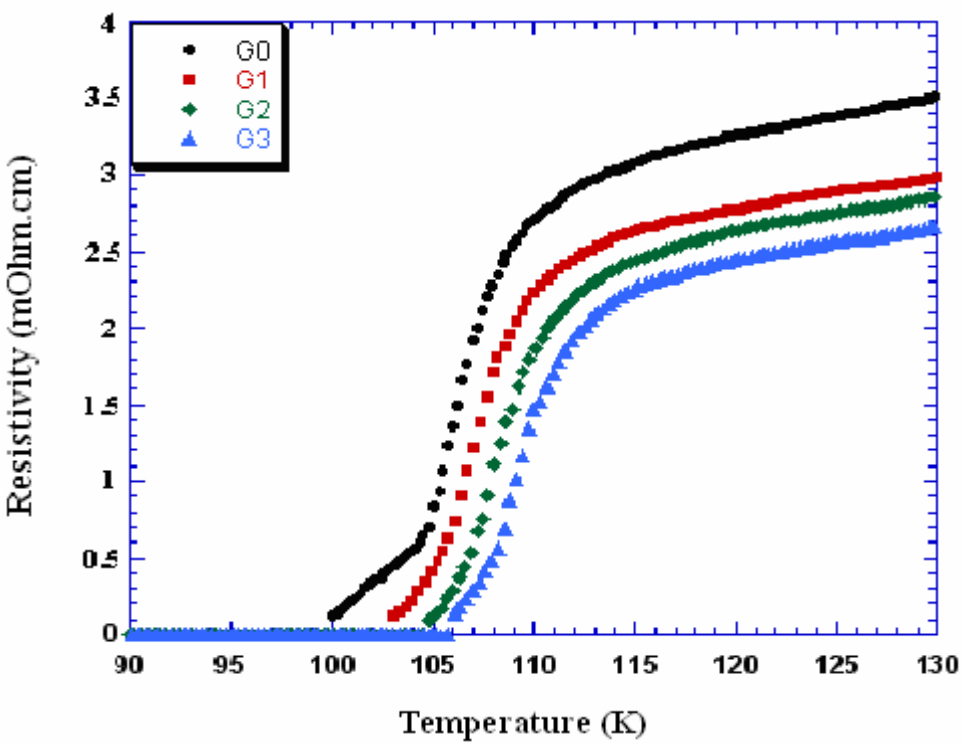

(a)

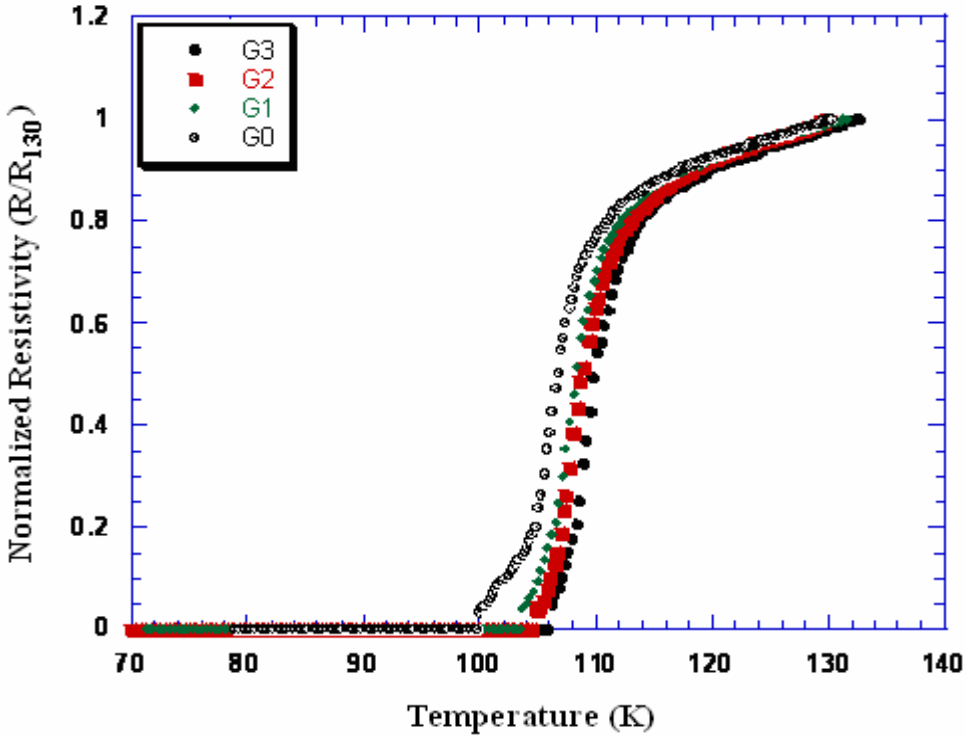

(b)

Figure 6.5: (a) Temperature dependence resistivity graph and **(b)** Temperature dependence normalized resistivity graph, for *G0, G1, G2* and *G3* samples.

Room temperature resistivities were calculated from room temperature *I-V* curves (Table 6.2). The value of the resistivity at room temperature was decreased upon *Au* doping and annealing time. Gold film on the sample forms a metallic connection; this resistive short-circuit connects the grains and lowers the room temperature resistivity. This effect continues even when gold film is diffused into the sample, indicating the gold's effect on grain boundary properties. The transition width of the samples decreases with increasing annealing time. The broadening of the transition width shows that *G0* sample has lower percentage of the Bi-2223 phase compared to that of gold diffused samples. The reduction of broadening in $\rho - T$ curve may be due to the modifying effect of the gold diffusion on the grain boundaries. Sharper transitions are accompanied by higher critical temperature and higher critical current density values.

Table 6.2: Some Physical properties of *G0, G1, G2* and *G3* samples.

Samples	***Critical Temperature*** T_c^{offset} ***(K)***	***Room Temp. Resistivity*** ρ ***(m*** Ω ***.cm)***
G0	100 ± 0.2	8.50
G1	104 ± 0.2	7.10
G2	105 ± 0.2	6.70
G3	106 ± 0.2	6.35

On the other hand, we have carried out further analysis of the temperature-resistivity data between the *G0* and *G1* samples. Both samples were annealed isothermally at 830 $^{\circ}C$ for 10 h. It was obtained that the transition curves from the normal state to superconducting state have double step behaviour, which is more

pronounced in *G0.* We believed that the double step resistive transition is an indication of weak links and dominancy of the *Bi-2212* phase. It is observed that the zero resistivity transition temperature of the *G1* (104 K) is higher than that for the *G0* sample (100 K). The increase in T_c may be related to the optimization of the hole concentration and possible changes in the lattice vibration of *Bi(Pb)-Sr-Ca-Cu-O***.** It is also possible that resistive nature of the grain boundaries is modified by accumulation of gold atoms at the grain boundaries but this requires to elucidation by transmission electron microscopy study, which is within our plans. Although wetting of the grain boundaries by a very thin layer of gold is unlikely, preferential accumulation of gold ions at the grain boundaries may reduce the resistive behaviour.

The electrical resistivity of *G830, G800, G750, G700, G600* and *G500* samples were measured using the standard four-probe DC technique, in the temperature range between 60 and 130 K. Room temperature resistivities were calculated from room temperature *I-V* curves for all samples and tabulated in Table 6.3.

Table 6.3: Some physical properties of temperature dependence undoped, and gold diffusion-doped samples.

Samples	T_c^{offset} **(K)**	J_c^{trans} **(A/cm^2)**	ρ **($m\Omega.cm$) at 300 K**
G830	104 ± 0.2	125	7.10
G800	80 ± 0.2	4	5.70
G750	98 ± 0.2	12	4.80
G700	95 ± 0.2	8	4.20
G600	102 ± 0.2	35	3.50
G500	103 ± 0.2	38	3.20
P830	100 ± 0.2	40	8.50

The room temperature resistivity value of all samples decreased with decreasing diffusion-annealing temperature. Annealing temperatures close to the optimum annealing temperature of 830 ^{o}C cause more degradation in superconducting properties than the lower annealing temperatures, being less degrading in gold-doped samples. 800 ^{o}C, 750 ^{o}C and 700 ^{o}C annealing temperatures are believed to produce impurity phases through phase segregation while 600 ^{o}C and 500 ^{o}C annealings only change oxygen content of the samples. The effect of gold doping is apparent in resistive tails, which is shorter in gold-doped samples.

Figures 6.6, 6.7, and 6.8, exhibits resistivity versus temperature for undoped and *Au* doped, *P830-G830, P700-G700*, and *P500-G500* samples respectively. In Figure 6.6, both samples were annealed isothermally at 830 $^{\circ}C$ for 10 h. It is observed that the zero resistivity transition temperature of the *G830* (104 K) is higher than that for the *P830* sample (100 K). This behaviour is observed in all samples with the same annealing temperature (between *P800* and *G800* etc.). Data of increasing T_c by about 4 K in the *G830* sample over that for undoped samples are reproducible using different batches of the sample.

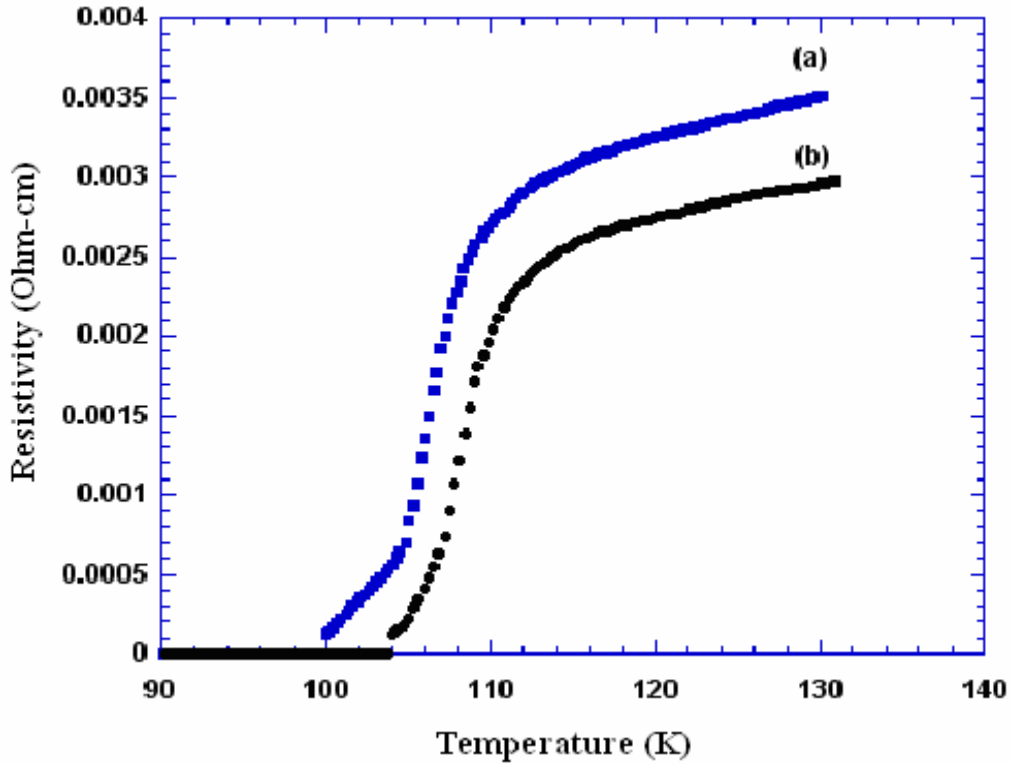

Figure 6.6: Resistivity versus temperature of the samples **(a)** *P830* and **(b)** *G830*.

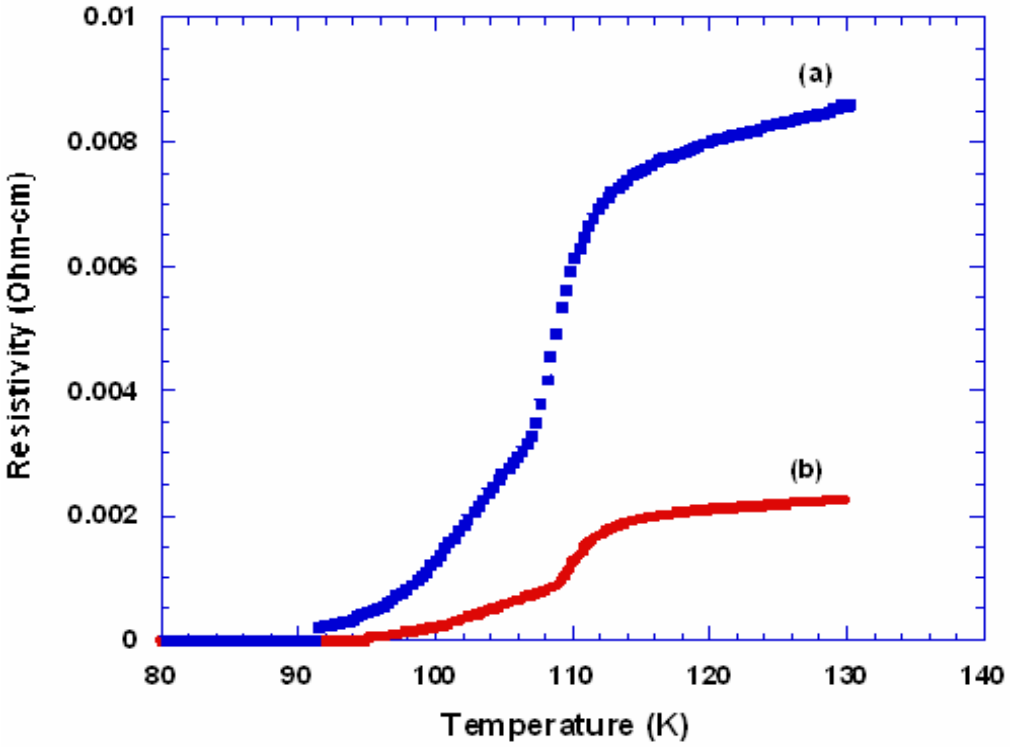

Figure 6.7: Resistivity versus temperature of the samples **(a)** *P700* and **(b)** *G700*.

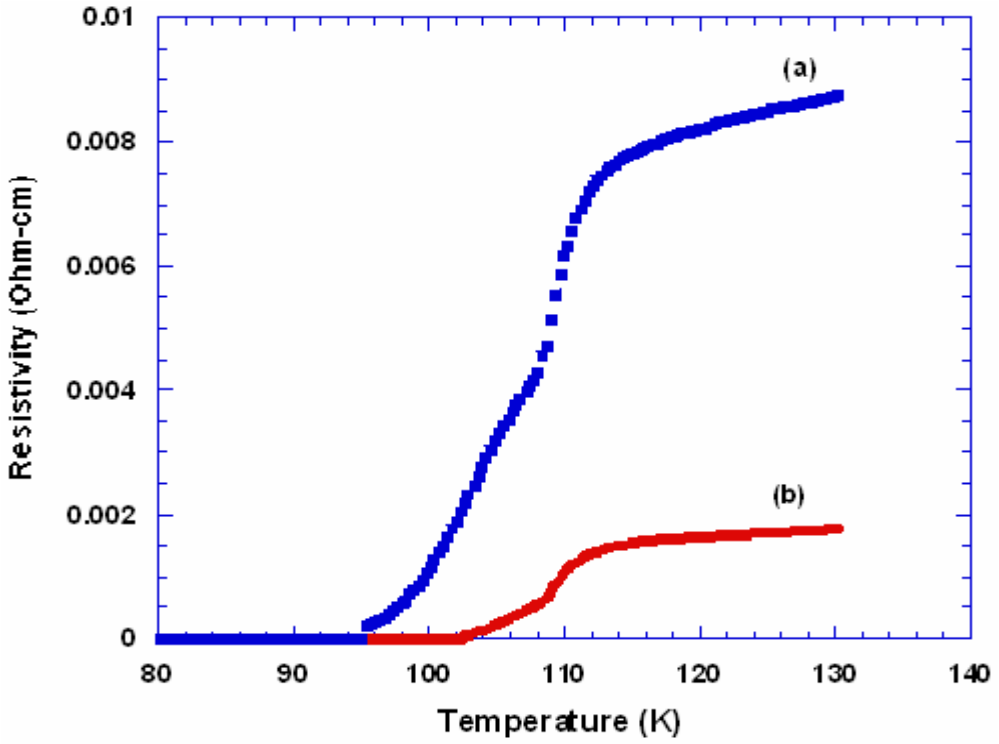

Figure 6.8: Resistivity versus temperature of the samples **(a)** *P500* and **(b)** *G500*.

6.5 Critical Current Measurements

The transport critical current density of the *Au* diffused-doped *Bi(Pb)-Sr-Ca-Cu-O* samples, measured in liquid nitrogen, are listed in Table 6.4**.** It should be noted that the transport critical current density of the gold-doped sample *G3* is about four times larger than that of undoped *Bi(Pb)-Sr-Ca-Cu-O* sample. A similar increase of J_c was observed in *Au*-doped *Bi(Pb)-Sr-Ca-Cu-O* [31] and *YBaCuO* superconductors [88]. The J_c of gold coated samples increases with increasing annealing time. The increase of J_c in *Bi(Pb)-Sr-Ca-Cu-O* by *Au* diffusion may be caused by the increase of grain sizes and their orientations, by improved coupling between *Au*-diffused superconducting grains, and by the increased number of flux pinning centres due to the presence of *Au* in the intergrain regions. This similar improving effect of the *Au*-

diffusion in J_c is revealed for the critical transition temperature. The increased value of J_c in the *Au* diffusion-doped samples compared with the *G0* in our investigations can be interpreted as a result of gold diffusion in intergrain boundaries. This in turn causes the increase of intergrain contact surface or decreasing the intergrain resistivity as can be seen in Figure 6.5. It is observed that the value of J_c in the *G1* sample (125 A/cm^2) is lower than that of the *G2* and *G3* (135 and 150 A/cm^2, respectively) in our investigations. The lattice parameter *c* is increased by *Au* doping. The longer the average length of the lattice parameter *c*, the higher J_c becomes. This indicates that *Au* doped *Bi-2223* sample has better J_c under the heat treatment schemes. From the above result, it was inferred that the annealing time has the positive effect on the J_c value of the samples. This similar improving effect of the *Au*-diffusion in J_c is revealed for the critical transition temperature. Annealing at lower temperatures had detrimental effect on critical current densities at 77 K. 600 ^{o}C and 500 ^{o}C annealing were less severe as shown in Table 6.3.

6.6 Carrier Concentration Calculation

The carrier (number of holes) concentration, *p*, is calculated by using the relation [89].

$$T_c/T_c^{max} = 1 - 82.6\,(p - 0.16)^2 \qquad (6.3)$$

where T_c^{max} is taken as 110 K for *Bi-2223* system. This formula is found to be applicable to several cuprate systems [9, 90]. The calculated carrier concentration is summarized in Table 6.4. It is observed that the hole carrier concentration for the *G0* and *G1* samples were 0.126 to 0.134, respectively. Further increasing diffusion

annealing time from 10 to 50 h increased the hole carrier concentration from 0.126 to 0.139. The slight increase in T_c may also be related to the optimization of the hole density. Thus, the *Au*-diffusion improves the carrier density by affecting the hole concentration and possible changes in the lattice vibration of *Bi(Pb)-Sr-Ca-Cu-O*.

Table 6.4: Some physical properties of *G0, G1, G2* and *G3* samples.

Samples	***Critical Temperature*** T_c^{offset} ***(K)***	***Critical Current Density at 77 K*** J_c^{trans}***(A/cm²)***	***Hole Concentration p***
G0	100 ± 0.2	40	0.126
G1	104 ± 0.2	125	0.134
G2	105 ± 0.2	135	0.137
G3	106 ± 0.2	150	0.139

6.7 Magnetoresistivity Measurements

We measured temperature (70-130 K) and DC magnetic field (0-0.5 T) dependent of resistivity of the samples with 5 mA DC current in a cryostat. The magnetic field was applied parallel to the current direction. The external DC magnetic fields for resistivity measurements were provided by an electromagnet. The transition temperature T_c was determined as the temperature at zero resistivity.

Figure 6.9 (a-d) shows temperature dependence of resistivity for all samples, at various magnetic fields (0, 0.1, 0.2, 0.3 and 0.5 T). It is observed that, with increasing dc magnetic field up to 0.5 T, T_c^{offset} ranges from 100 K to 67 K for *G0* sample, 104 K

to 70 K for *G1*, 105 K to 71 K for *G2*, and 106 K to 75 K for *G3*. As can be seen from the all figures, T_c^{offset} increased with increasing diffusion annealing time; also we can see T_c^{offset} decreased of each sample with increasing external magnetic field. The width of intragrain transition slowly increases with increasing magnetic field. Below T_c^{onset}, the thermally activated flux flow (TAFF) is an important dissipation mechanism inducting a long resistance tail [91].

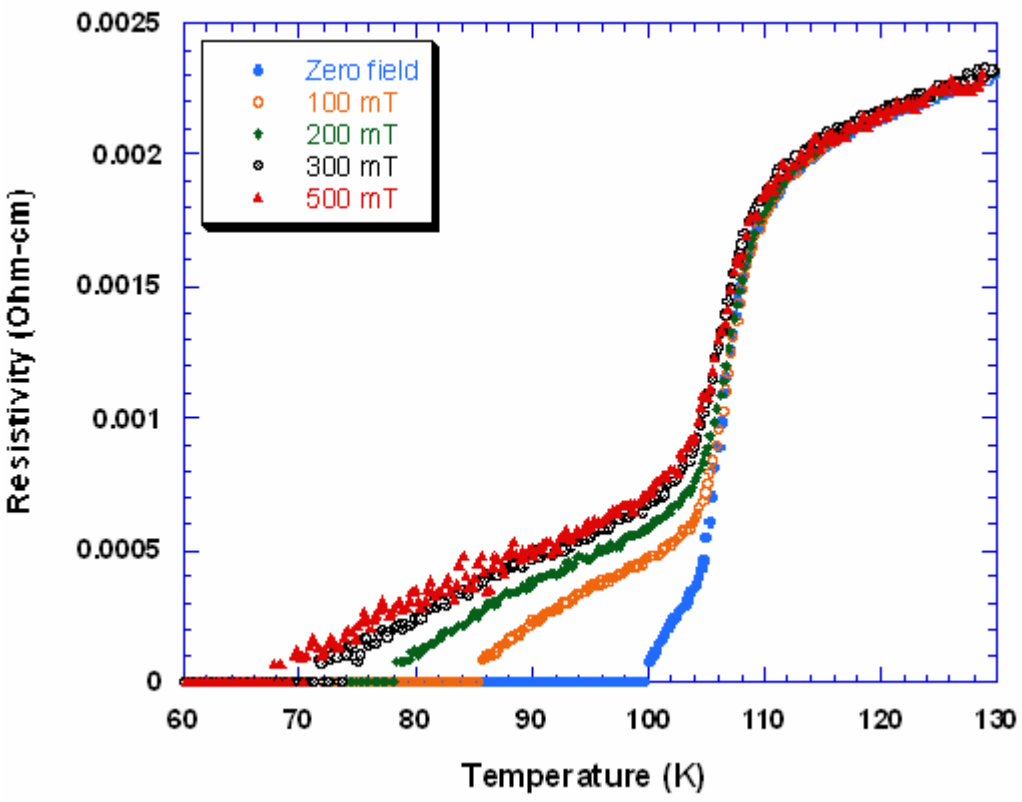

(a)

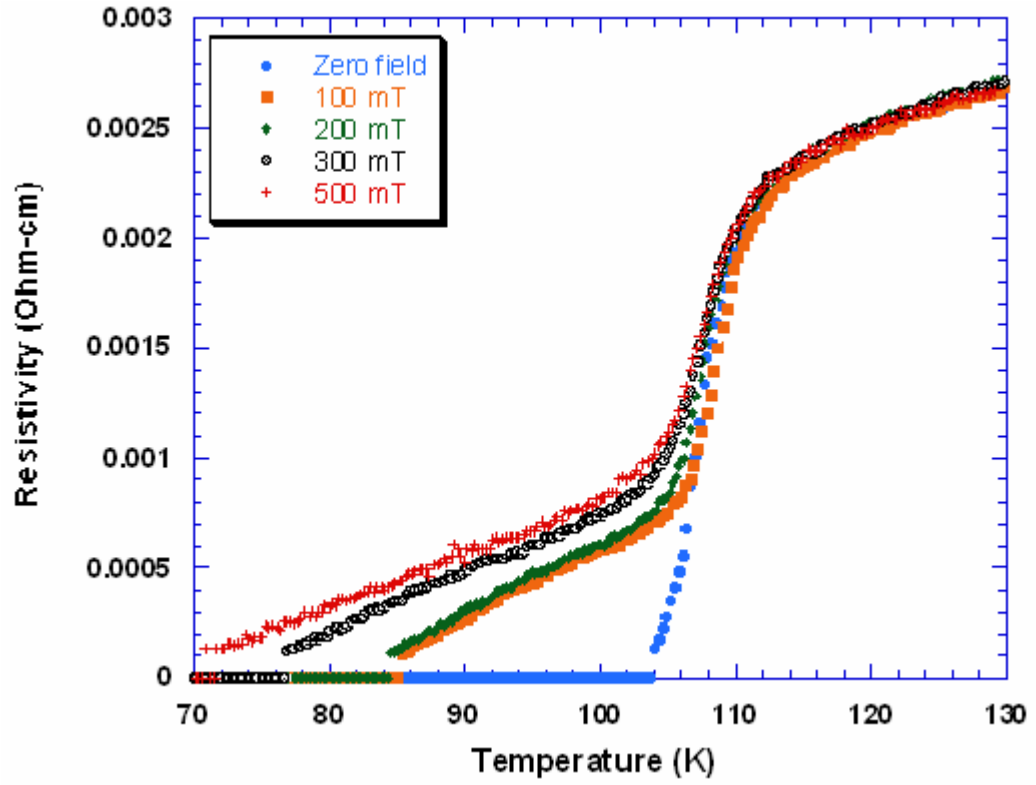
Zero field
100 mT
200 mT
300 mT
500 mT
Resistivity (Ohm-cm)
Temperature (K)
0.003
0.0025
0.002
0.0015
0.001
0.0005
0
70
80
90
100
110
120
130

(b)

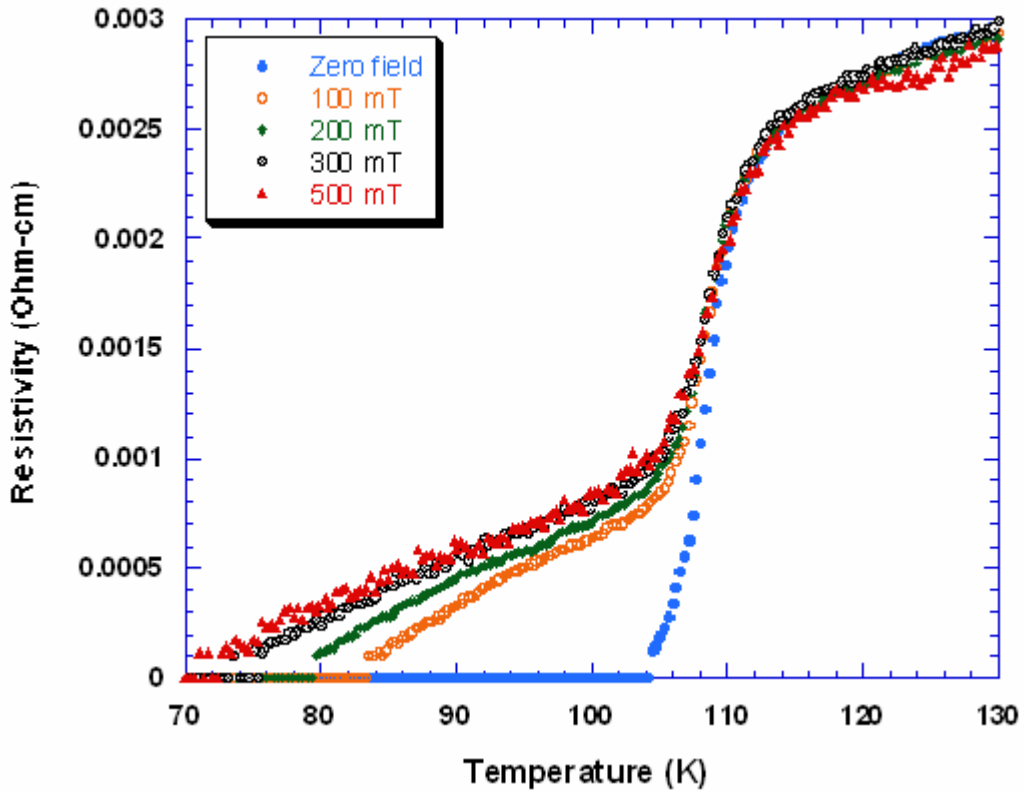
Zero field
100 mT
200 mT
300 mT
500 mT
Resistivity (Ohm-cm)
Temperature (K)
0.003
0.0025
0.002
0.0015
0.001
0.0005
0
70
80
90
100
110
120
130

(c)

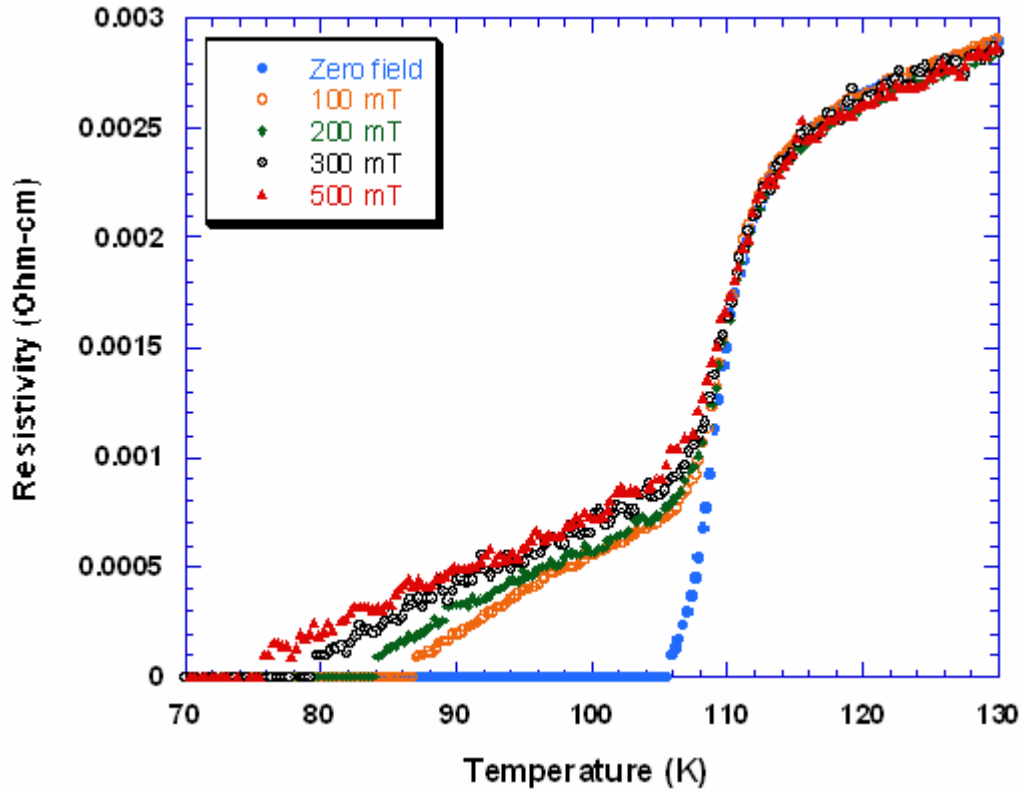

(d)

Figure 6.9: Temperature dependence of resistivity for **(a)** *G0*, **(b)** *G1*, **(c)** *G2*, and **(d)** *G3* samples, at various magnetic fields up to 0.5 T.

6.8 AC Susceptibility Measurements

We investigated the effect of *Au* diffusion-doped and diffusion-annealing duration in *Bi(Pb)SrCaCuO* high temperature superconductors by using the low field AC magnetic susceptibility method [92]. The AC magnetic susceptibility as a function of temperature was measured by means of a Lake Shore 7130 AC Susceptometer in the temperature range 40–120 K in a magnetic field of 20-320 A/m and 111 Hz frequency. The sample, kept in helium exchange gas with a controllable temperature resolution better than 10 mK, was moved from the centre of one secondary coil to the other to eliminate unwanted signals and to maximize the signal from the sample itself.

The AC field was applied parallel to the long axis of the sample. For AC susceptibility measurements automatic data acquisition was selected. AC susceptibility ($\chi(T) = \chi'(T) - i\chi''(T)$) as a function of temperature under different AC field amplitudes for *G0, G1, G2*, and *G3* are shown in Figure 6.10 (a-d). The onsets of diamagnetism are at 110 K for the all samples.

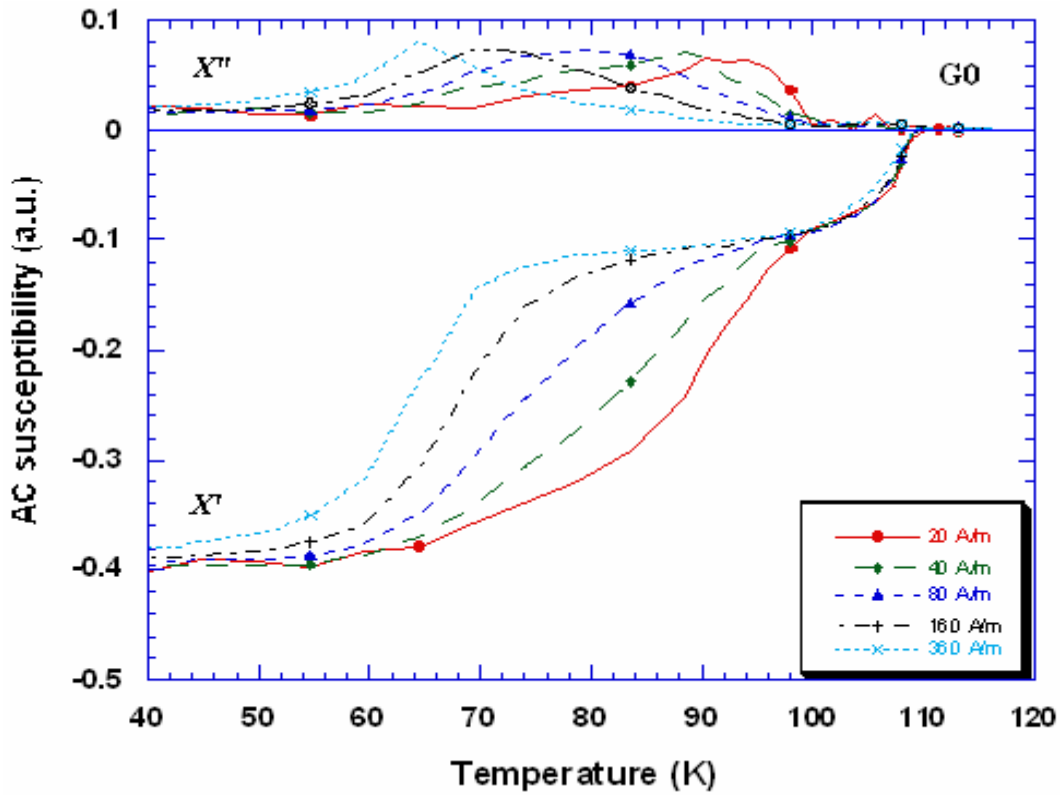

(a)

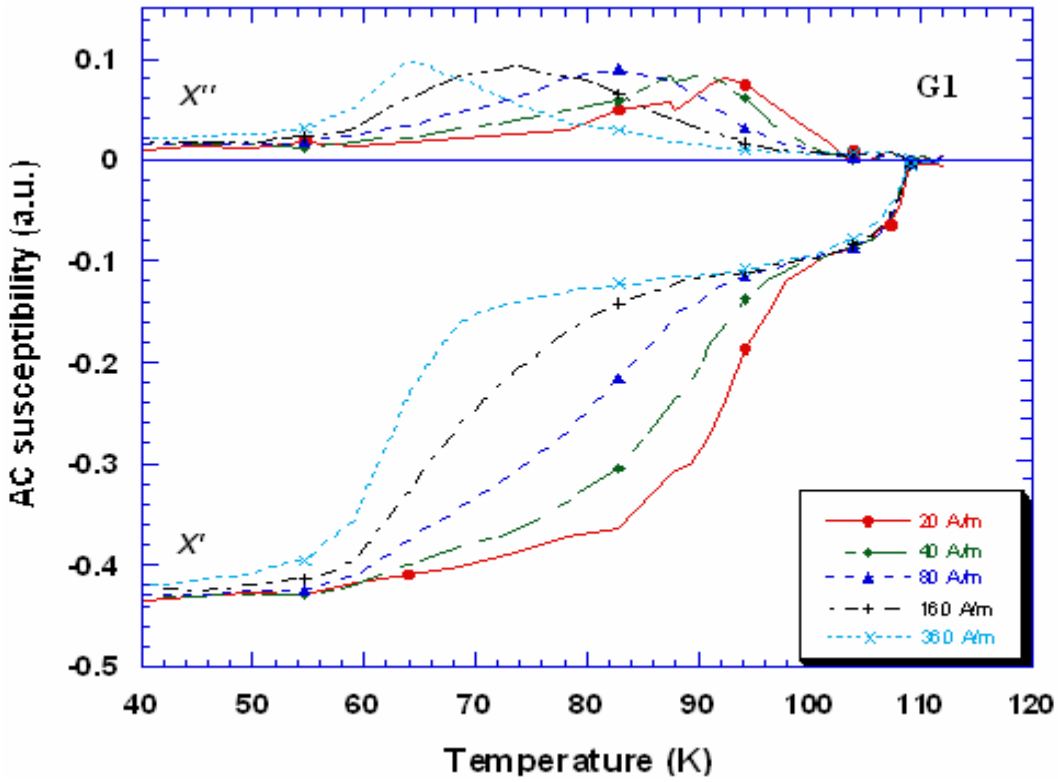
G1
X''
X'
AC susceptibility (a.u.)
Temperature (K)
20 A/m
40 A/m
80 A/m
160 A/m
360 A/m

(b)

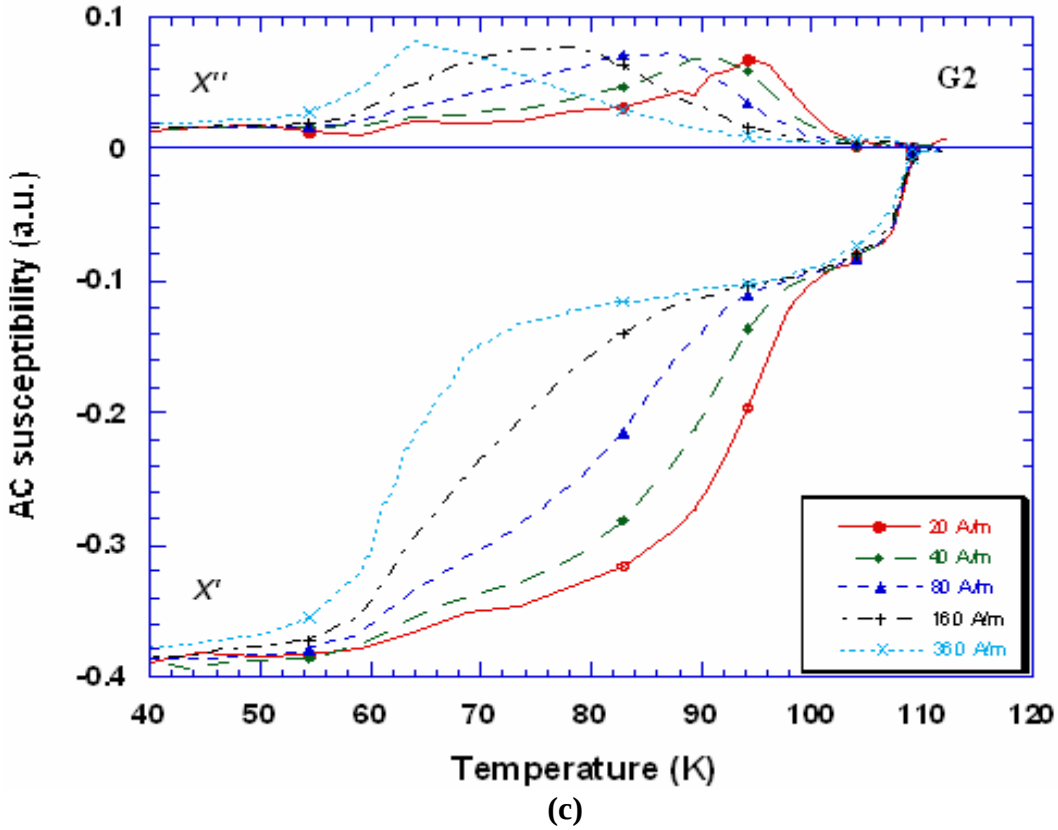
G2
X''
X'
AC susceptibility (a.u.)
Temperature (K)
20 A/m
40 A/m
80 A/m
160 A/m
360 A/m

(c)

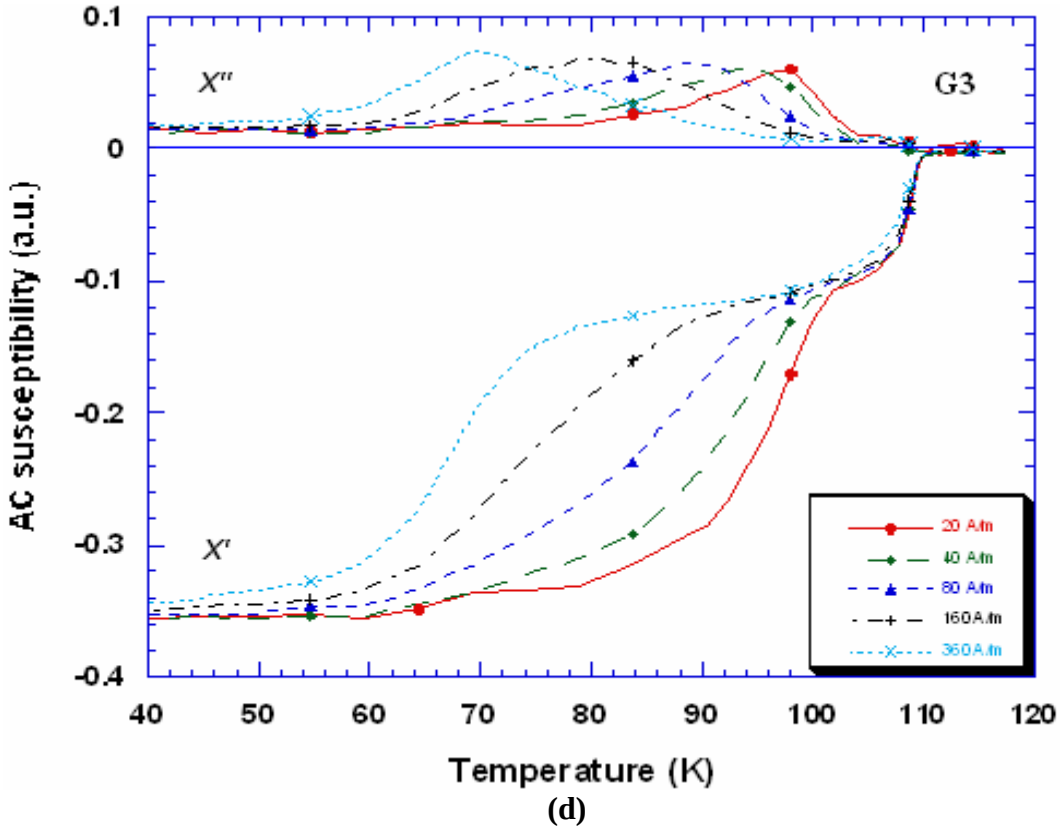

Figure 6.10: AC susceptibility as a function of temperature under different AC field amplitudes for **(a)** *G0*, **(b)** *G1*, **(c)** *G2*, and **(d)** *G3* samples.

It was observed that the overall susceptibility curves of the samples are shifted to lower temperature by increasing the AC field amplitude. The intensity of the imaginary parts increased with increasing the AC field amplitude. The susceptibility-temperature curves shifted to lower temperatures and considerably increased the transition width in χ''-T curves, and also decreased the shielding fraction of the superconducting phase in the samples with increasing the gold diffusion time.

Figure 6.10 (a-d) exhibit that the peak temperature (T_p) of χ'' shifts to lower temperatures when the field amplitude increases. The shift is related to the pinning

force strength. The larger the shift in the maximum of χ'', the weaker is the pinning, [93]. At the peak values of the imaginary part, the AC field amplitude is equal to the full flux penetration field, H_p.

Figure 6.10 and figure 6.11 gives information about the grain sizes and grain boundary effect for a given magnetic field strength. As seen from Figure 6.11 (a-c), the shielding effect is more noticeable for the *G3* than for that of the *G2*, *G1 and G0* under 20, 80, 320 A/m AC field amplitudes. Similar behavior is seen for other field values.

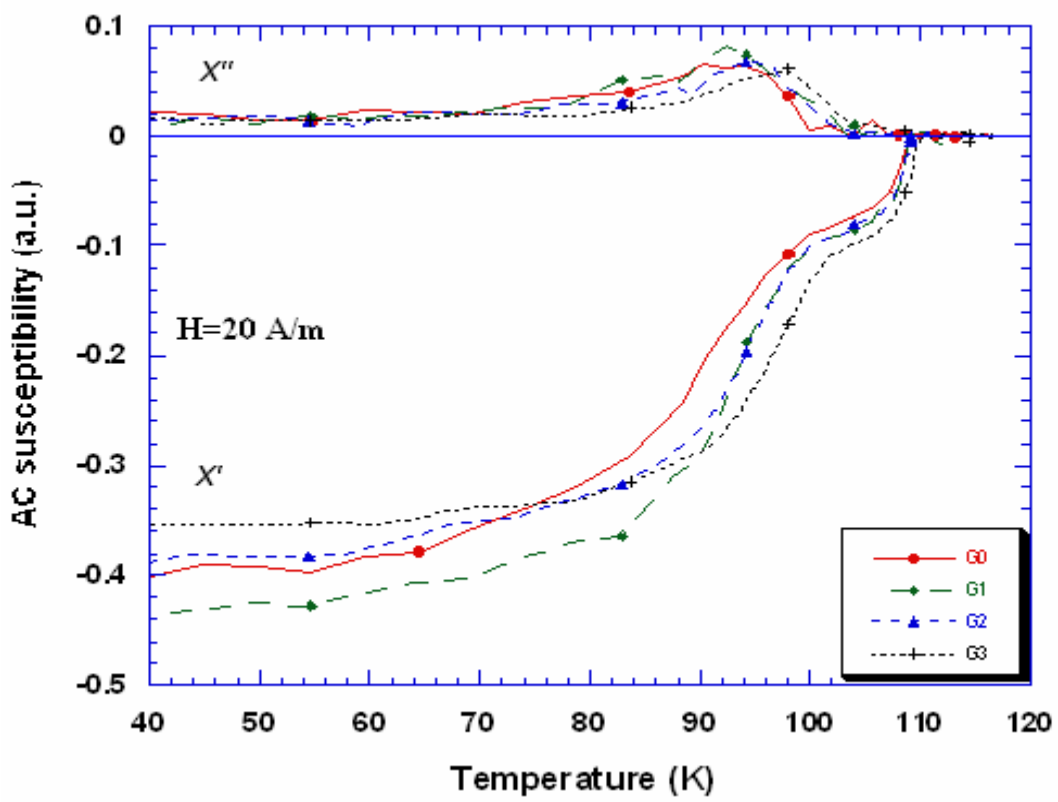

(a)

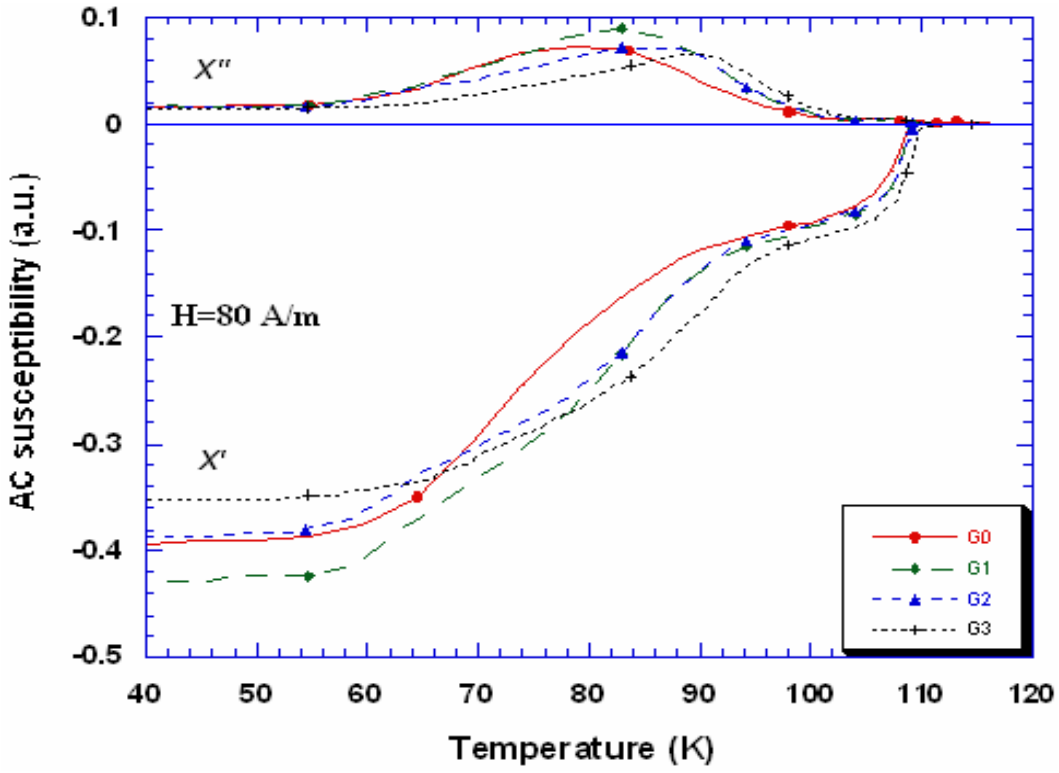

(b)

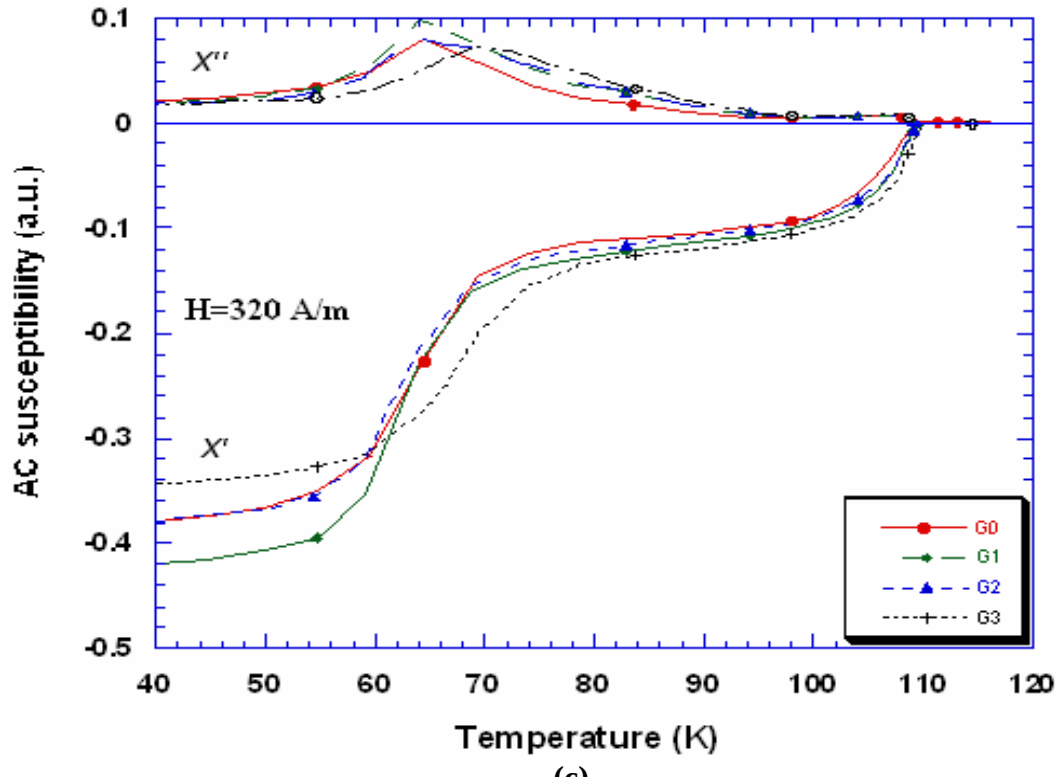

(c)

Figure 6.11: AC susceptibility as a function of temperature under **(a)** 20, **(b)** 80, **(c)** 320 A/m AC field amplitudes for *G0, G1, G2*, and *G3* samples.

We have investigated the peak temperature dependence as a function of AC magnetic field, $H_{ac,}$ in order to study the effect of *Au* diffusion and diffusion-annealing time on the intergranular pinning force (Figure 6.12). As can be seen from Figure 6.12, a linear dependence of T_p as a function of H_{ac} is observed for all the samples. Müller critical state model assumes a magnetic flux independent pinning force densities, and α_J and α_g for inter- and intragranular vortices described by the relation;

$$T_p = T_{p0} - T_{p0} U^{1/2} H_{ac} \tag{6.4}$$

where U is $\left[\frac{\mu_0 \mu_{eff}(0)}{2a\alpha_J(0)}\right]$, a is the length of the samples, $\mu_{eff}(0)$ is the effective permeability of the ceramic, and $\alpha_J(0)$ is the intergranular pinning force density. From a least squares fit of this expression (Eq. 6.4) to the data T_{p0} and U were extracted for all samples (Table 6.5). The values of T_{p0} increased while U decreased with increasing diffusion-annealing time. This means that the values of $\alpha_J(0)$ increases with increasing the diffusion-annealing time, being consistent with present transport critical current density measurement such as J_c decreased with increasing the diffusion-annealing time. A decreasing trend in pinning force of the samples with decreasing diffusion-annealing time is attributable to grater voids and defects as will be confirmed by SEM results.

Table 6.5: From a least squares fit of Eq. (6.4) to the data T_{p0} and U were extracted for *G0, G1, G2,* and *G3* samples.

Samples	J_c^{inter}(A/cm^2) (at 77 K)	T_{p0} (K)	U
G0	13.06	90.34	0.085977
G1	15.70	93.17	0.089810
G2	18.21	95.46	0.093293
G3	21.45	97.70	0.094194

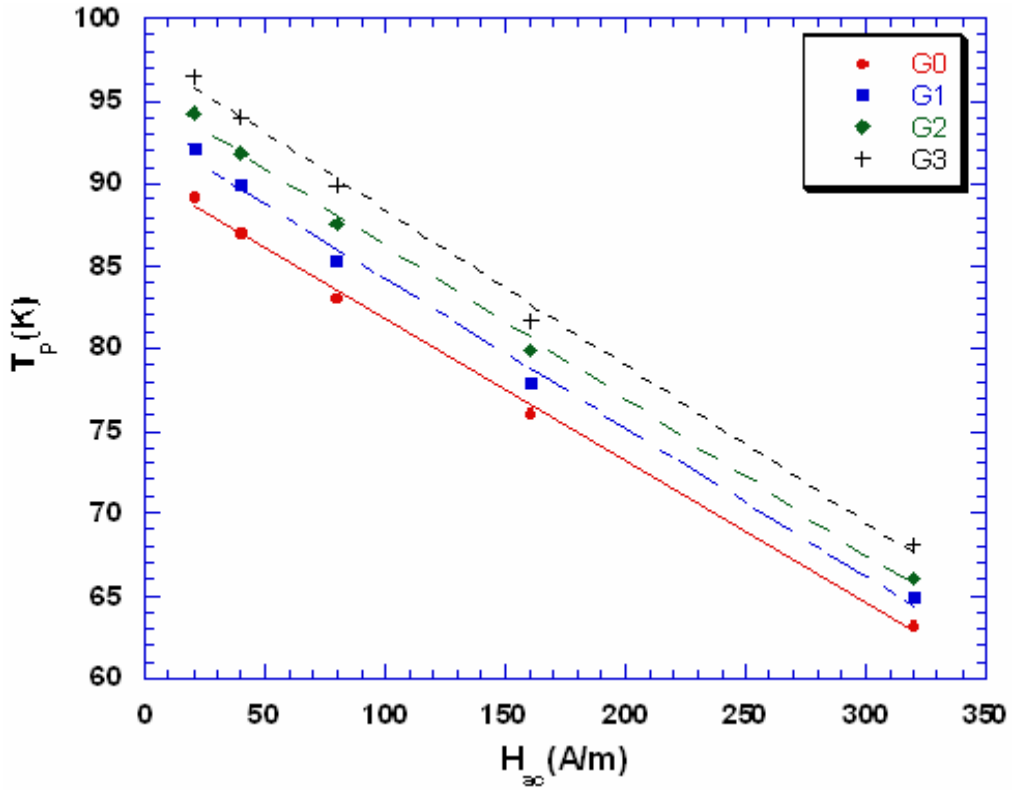

Figure: 6.12: The peak temperature dependence as a function of AC magnetic field, for *G0, G1, G2,* and *G3* samples.

The temperature dependence of intergranular critical current density, $J_c(T_p)$, is often determined via the temperature dependence of the intergrain maximum in the imaginary part, $\chi''(T)$ of the AC susceptibility using the Bean model [65] (Figure 6.13). $J_c(T_p)$ is calculated for our samples using the relation $J_c(T_p) = H_a/a$ for the sample having cross section of the rectangular bar shaped, like *2ax2b* where a < b. $J_c(T_p)$ is the intergranular current density and H_a is the amplitude of applied field at T_p. The determined $J_c(T_p)$ at 77 K for the samples is listed in Table 6.5**.** As seen from the table, the value of $J_c(T_p)$ increases with increasing diffusion-annealing time. This result is consistent with present transport critical current density measurements. Moreover, we observed the same evidence for this behavior in ρ-T transport measurements in the samples such as T_c increases with increasing diffusion-annealing time.

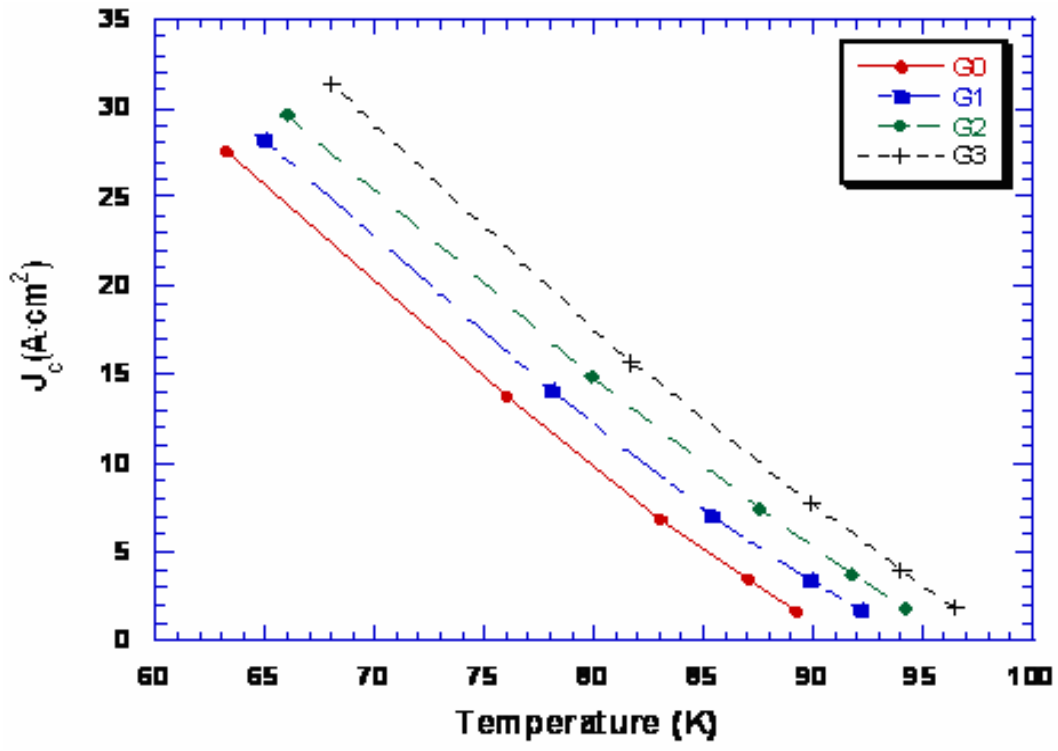

Figure 6.13: The temperature dependence of intergranular critical current density, for *G0, G1, G2,* and *G3* samples.

6.9 Diffusion Coefficient and Activation Energy Calculation

The diffusion coefficients of gold may be useful for the understanding of doping mechanism and changes of microstructure and superconducting properties of *BSCCO* systems under doping. To our knowledge, no detailed work on the calculation of the *Au* diffusion coefficient in a *Bi(Pb)-Sr-Ca-Cu-O* bulk sample has been published in the literature.

There are several methods to estimate the diffusion parameter in polycrystalline high-T_c superconductors. The most common four methods are: successive removal of thin layers and (1) the measurements of lattice parameters from XRD patterns, (2) the measurement of the sample's resistivity, (3) the radio-tracer, and (4) the energy dispersive X-ray fluorescence method. In this study, we used first and second technique to calculate the diffusion coefficient of *Au* in *Bi(Pb)-Sr-Ca-Cu-O* system.

In this part the diffusion parameters of *Au* determined lattice parameter *c* from XRD patterns at room temperature of diffusion-doped *Bi(Pb)SrCaCuO-Au* samples. The XRD measurements provide data about lattice parameters for only a thin surface layer of *Au*-diffused $Bi_{1.8}Pb_{0.35}Sr_{1.9}Ca_{2.1}Cu_3O_y$ sample. Hence, information about the diffusion profile of non-uniformly distributed *Au* in $Bi_{1.8}Pb_{0.35}Sr_{1.9}Ca_{2.1}Cu_3O_y$ can be obtained by the successive removal of thin layers from the *Au*-diffused surface of the sample and the measurement of the lattice parameters. It is observed that substitution of matrix atom by impurity atoms with a different radius causes a deformation near the impurity atoms [94]. This results in changes of lattice parameters of the specimen. The deformation, ε, in the region of the crystalline lattice at point *x* is given by

$$\varepsilon(x) = [c(x) - c_0]/c_0, \tag{6.5}$$

where $c(x)$ and c_0 are the lattice parameters in the deformed and non-deformed region of the samples, respectively. This deformation is related to the radii of impurity and matrix atoms, and also the concentration of impurity atoms, $N(x)$, namely by the relation

$$\varepsilon(x) = \beta N(x). \tag{6.6}$$

Here β is the expansion coefficient of the lattice given by following equation

$$\beta = \frac{1}{3N_\ell}\left[1 - \left(\frac{r_i}{r_0}\right)^3\right], \tag{6.7}$$

where r_i and r_0 are the radii of the impurity and the matrix atoms, respectively, and N_ℓ is the concentration of the matrix atoms. Thus, data about the concentration profile of the diffusing impurity in the *Au*-diffused sample can be found by measuring the distribution of deformation $(\varepsilon(x) = \Delta c / c_0)$ over the thickness of the samples.

In this study, it is supposed that the conditions of impurity diffusion from a constant source into semi-infinite solid are satisfied by the following equation [52]

$$N(x,t) = N_0\left[1 - erf\left(x / 2\sqrt{Dt}\right)\right] \tag{6.8}$$

where $erf[x/2(Dt)^{1/2}]$ represents the error function with argument $y = x/2(Dt)^{1/2}$

$$erf(y) = \frac{2}{\sqrt{\pi}} \int_0^y \exp(-y^2). \tag{6.9}$$

Here $N_0 = N(0,t)$ is the constant concentration on the surface of the sample, $N(x,t)$ is the impurity concentration at the distance x, D is the diffusion coefficient, and t is the diffusion annealing time.

As was already mentioned above, one would expect that the change of lattice parameter c with the thickness of the samples resembles the concentration distribution of diffusion gold impurity. From this consideration, the change of lattice parameter c by successive removal of thin layers from the sample and by XRD measurements was studied. Figure 6.14 represents the variation of lattice parameter $\Delta c / c_0$ (c_0 is the lattice parameter of the undoped region of the sample) as a function of thickness of the sample, exposed to *Au* diffusion at $800^\circ C$ for 10 h.

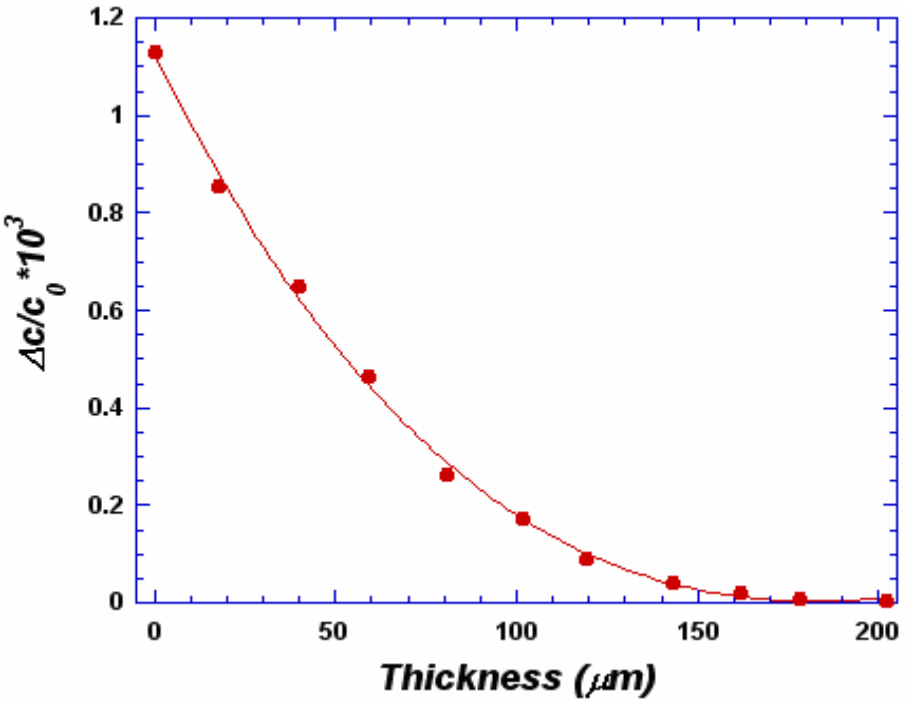

Figure 6.14: Variation of lattice parameter $\Delta c / c_0$ as a function of thickness of the sample.

The solid curve shows the calculated concentration profile of *Au* in Bi-2223. The experimental data of Fig. 6.14 fit well with the theoretical curve, calculated for $D = 1.2 \times 10^{-8}$ cm^2s^{-1} at $800^\circ C$ using Eq. (6.8). The same fitting method was used for the samples diffusion–annealed at 500, 600,700, and $750^\circ C$. Diffusion at lower temperatures is much less significant, being in agreement with our SEM given earlier in this thesis. The mean values of the diffusion coefficients of *Au* in $Bi_{1.8}Pb_{0.35}Sr_{1.9}Ca_{2.1}Cu_3O_y$ as a function of temperature are given in Figure 6.15.

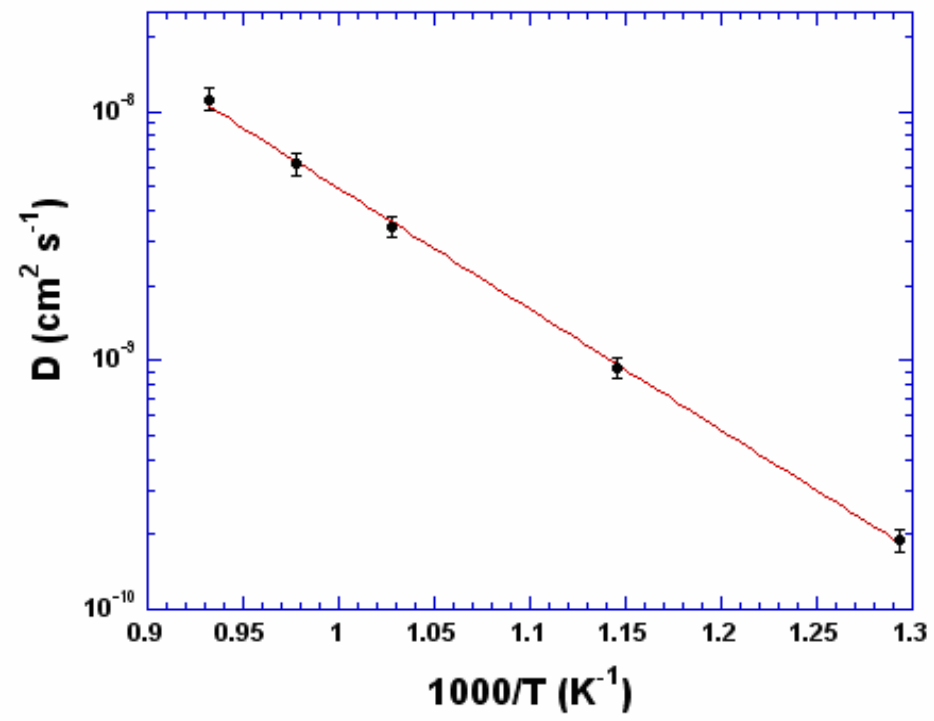

Figure 6.15: The mean values of the diffusion coefficients of *Au* in $Bi_{1.8}Pb_{0.35}Sr_{1.9}Ca_{2.1}Cu_3O_y$ as a function of temperature.

The results of these studies showed that the *Au* diffusion coefficient in $Bi_{1.8}Pb_{0.35}Sr_{1.9}Ca_{2.1}Cu_3O_y$ system in the temperature range 500-800 $^\circ C$ increases in accordance with the Arrhenius relation

$$D = 4.4 \text{ x } 10^{-4} \ \ exp\{(-1.08 \pm 0.10)eV / k_B T\} \tag{6.10}$$

This relatively low value of the activation energy (1.09 eV) of *Au* in $Bi_{1.8}Pb_{0.35}Sr_{1.9}Ca_{2.1}Cu_3O_y$ may testify that the migration of *Au* primarily proceeds trough defects of polycrystalline sample (pore surfaces, grain boundaries etc.) as in the case for *Au* diffusion in *YBaCuO* ceramics [52].

Investigations of *Au* diffusion were carried out in the *Bi-2223* in the temperature range between 500 and 800$^\circ C$. Measuring the distribution of the resistivity of the removed layers over the thickness of the sample one can find the concentration profile of the impurity diffusion. The resistivity distributions over the thickness of the sample were determined by the successive removal of thin plate- parallel layers and measurement of the resistivity by a standard DC four-probe technique at room temperature. Figure 6.16 represents the dependence of the conductivity on the thickness of the layers removed from the sample, after being exposed to the diffusion of *Au* at 700$^\circ C$ for 10 h. The solid curve shows the calculated concentration profile of *Au* in *Bi-2223*. In this study, it is supposed that the conditions of impurity diffusion from a constant source into semi-infinite solid are satisfied by the Equation 6.8 [52].

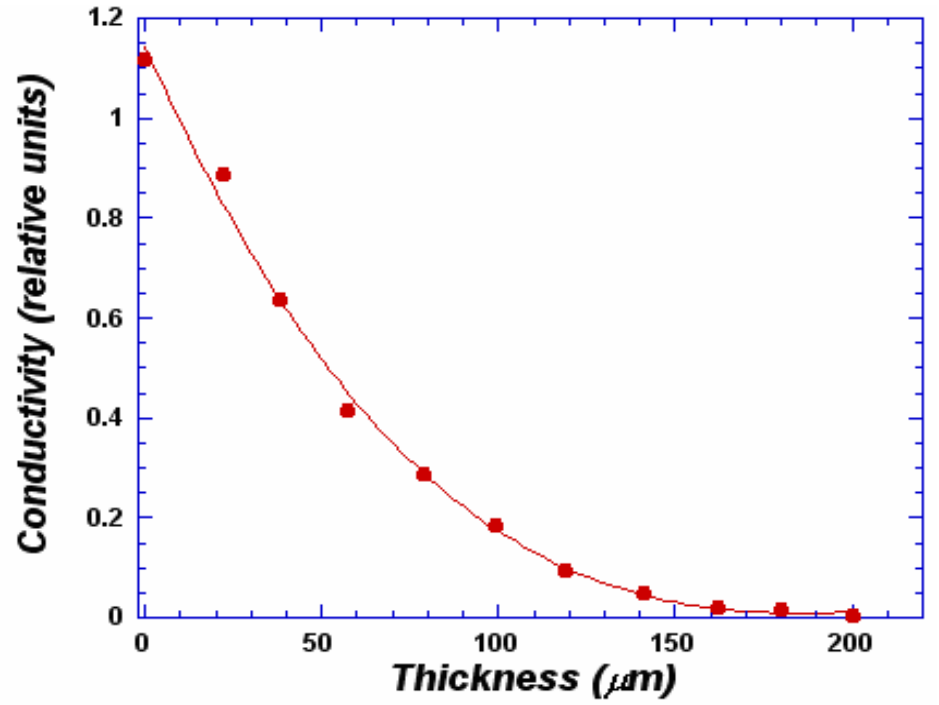

Figure 6.16: The dependence of the conductivity on the thickness of the layers removed from the sample.

The experimental data of Figure 6.16 fit well with the theoretical curve, calculated for D = 2 x 10^{-9} cm^2s^{-1} at $700^\circ C$ by using Eq.(6.8). The same fitting method was used for the samples diffusion–annealed at 500, 600, 750 and $800^\circ C$. Diffusion at lower temperatures is much less significant in agreement with our SEM given earlier in this thesis. Dzhafarov *et al*. used this method to calculate the diffusion coefficient of *Ag* in *Bi(Pb)-Sr-Ca-Cu-O* [31]. Diffusion at lower temperatures is much less significant. The mean values of the diffusion coefficients of *Au* in $Bi_{1.8}Pb_{0.35}Sr_{1.9}Ca_{2.1}Cu_3O_y$ as a function of temperature are given in Figure 6.17.

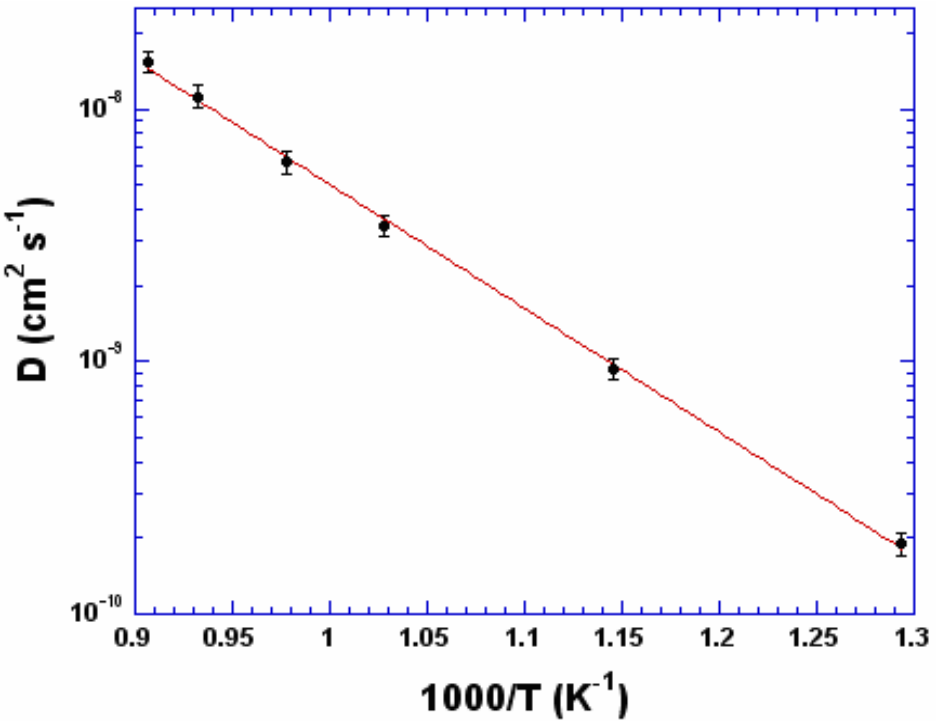

Figure 6.17: The mean values of the diffusion coefficients of *Au* in $Bi_{1.8}Pb_{0.35}Sr_{1.9}Ca_{2.1}Cu_3O_y$ as a function of temperature.

The results of these studies showed that the *Au* diffusion coefficient in $Bi_{1.8}Pb_{0.35}Sr_{1.9}Ca_{2.1}Cu_3O_y$ system in the temperature range 500-800 $^{\circ}C$ increases in accordance with the Arrhenius relation

$$D = 4.1 \text{ x } 10^{-4} \ exp\{(-1.08 \pm 0.10)eV / k_B T\} \qquad (6.11)$$

This relatively low value of the activation energy (1.08 eV) of *Au in* $Bi_{1.8}Pb_{0.35}Sr_{1.9}Ca_{2.1}Cu_3O_y$ may testify that the migration of *Au* primarily proceeds trough defects of polycrystalline sample (pore surfaces, grain boundaries etc.).

6.10 Mechanical Properties

Engineering applications of high critical temperature (T_c) superconducting ceramics are generally restricted because of their brittleness. Therefore, improvement of the mechanical properties of *BSCCO* is a major research objective and very important for their practical applications and high performance such as quasi-permanent magnets and current leads. Hardness is a mechanical parameter and it is strongly related to the structure and composition of solids. The Vickers microhardness test is one of the convenient methods to estimate the mechanical properties. Many investigations have confirmed that the apparent (load dependent) hardness of materials is a function of the applied load. In another word, the experimentally measured hardness decreases with increasing applied load which is called indentation size effect (ISE).

It is worth to mention that the annealing step is one of the important parts of wire production process where one can control the physical and mechanical properties of high-T_c superconductors**.** There are many researches about the effect of annealing time and temperature on microstructure, superconducting and mechanical properties of high-T_c superconductors [95-99]. Many studies of doping into superconductor oxide ceramics have been made in order to improve their mechanical and superconducting properties [13, 69-72, 100].

In order to estimate the effect of *Au* doping and diffusion-annealing time on the mechanical properties of the samples, we measured the diagonal length as a function of test load. Conventional Vickers microhardness measurements consist of applying a load F on the test material via a geometrically defined indenter and after the indenter is removed, measuring the characteristic dimension, d, of the resultant

impression. The Vickers microhardness (apparent) values of different applied loads were calculated by using the equation from [101],

$$H_v = 1854.4\left(F/d^2\right) \quad (GPa) \tag{6.12}$$

where F is the applied load in N and d is the diagonal length of the indentation mark in μm. The calculated load dependent microhardness values for different applied loads are summarized in Table 6.6.

Table 6.6: The calculated load dependent H_v, E, Y, K_{ic} and B_i for the samples.

Sample	Load (N)	H_v (GPa)	E (GPa)	Y (GPa)	K_{IC} (Pa m$^{-1/2}$)	B_i (m$^{1/2}$) × 10^5
G0	0.245	0.458	37.53	0.153	490.9	9.327
	0.490	0.317	26.02	0.106	408.8	7.766
	0.980	0.262	21.47	0.087	371.3	7.054
	1.960	0.244	19.98	0.811	358.2	6.806
	2.940	0.239	19.60	0.079	354.8	6.740
G1	0.245	0.515	42.22	0.172	545.4	9.443
	0.490	0.358	29.32	0.119	454.5	7.879
	0.980	0.302	24.74	0.101	417.5	7.234
	1.960	0.273	22.41	0.091	397.4	6.917
	2.940	0.270	22.16	0.090	395.2	6.832
G2	0.245	0.657	53.84	0.219	650.2	10.010
	0.490	0.404	33.15	0.135	510.3	7.917
	0.980	0.327	26.77	0.109	458.4	7.134
	1.960	0.306	25.07	0.102	443.7	6.897
	2.940	0.295	24.16	0.098	425.6	6.931
G3	0.245	0.823	67.43	0.274	769.6	10.690
	0.490	0.424	34.74	0.141	552.4	7.676
	0.980	0.371	30.40	0.124	516.7	7.180
	1.960	0.327	26.77	0.109	484.9	6.744
	2.940	0.313	25.65	0.104	474.6	6.595

Figure 6.18 displays the variation of microhardness as a function of the applied load for the *G0*, *G1*, *G2*, and *G3* samples. The variation of microhardness with load has similar shape irrespective of the *Au* doping although numerical values are different.

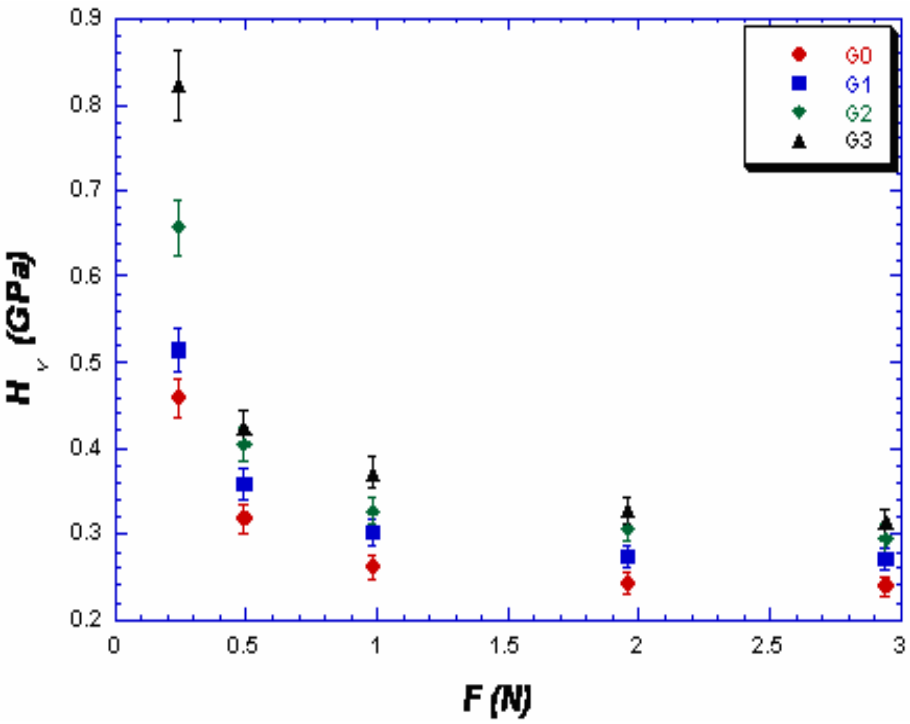

Figure 6.18: The variation of microhardness with load for samples.

We have observed that the microhardness values increased with increasing diffusion-annealing time. The reason of this is ascribed to *Au* doping (diffusion) being able to fill the intergrain space, and leading to a remarkable increase in the mechanical resistance of the samples. SEM pictures (Fig. 6.3) shows a denser microstructure confirming this conclusion. It was observed that Vickers hardness increased with increasing amount of doping in *Bi-2223* superconductors [13, 70, 102]. The rapid variation of microhardness was observed with increasing applied load from 0.245 to 2.000 N. The reason for this behaviour is due to the contribution of weak grain boundaries [103]. It is also obvious from the figure that the Vickers microhardness values are load dependent for all samples; the calculated microhardness value decreases non-linearly as the applied load decreased until 2 N, then it tends to attain saturation. As reported by Khalil [104], this behavior can be explained as following;

a) at larger indention loads, the Vickers hardness registered smaller values, this observation may be due to the presence of weak grain boundaries of the superconducting ceramics; b) at smaller indention loads, the Vickers hardness recorded higher values, this is ascribed to the fact measured hardness values were more indicative of the monocrystalline state without interference from grain boundaries. This non-linear behavior has also been observed in the literature for *Bi-Pb-Sr-Ca-Cu-O* samples [13, 70, 71] and is known as indentation size effect (ISE) [105, 106].

To account for this effect, several relationships between the applied load and the resulting indentation size have been suggested [107-110]. This effect can be explained by two different methods [101]. The first method assumes that the indentation contains an elastic portion. The elastic part of the deformation is relaxed upon removal of loading. This can be accounted for by adding an elastic component, d_e, to the measured plastic indentation semidiagonal, d_p. Thus, a true hardness, H_0, is defined from [101, 111]

$$H_0 = 1854.4\left(\frac{F}{(d_p + d_e)^2}\right) \qquad (GPa) \tag{6.13}$$

Therefore, Eq. (6.13) indicates that measured indentation diagonals should be linear with the square root of the applied load and the slope of such a curve is proportional to $(H_0)^{1/2}$ and the vertical intercept of this graph is proportional to the elastic part of the indentation semi diagonal, d_e. The load dependence of indentation diagonals for *G0*, *G1*, *G2* and *G3* samples was reanalyzed as d_p versus $F^{1/2}$ plots, as in Figure 6.19.

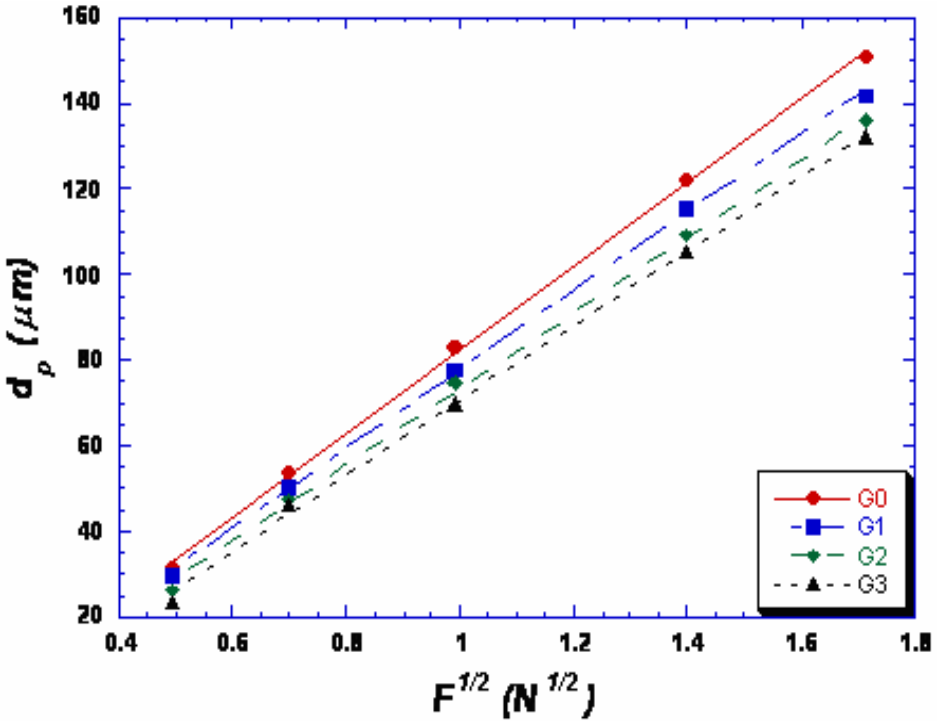

Figure 6.19: Plots of diagonal length versus square root of applied loads for the sample.

It was obvious that such plots are linear with the estimated linear regression coefficients (*LRC*) always better than 99.9%, implying that Eq. (6.13) provides a satisfactory description to calculate the true hardness of the indentation data for the samples. The extracted values of H_o, d_e and *LRC* are listed in Table 6.7.

Table 6.7: Best-fit results of experimental data according to equation (6.13).

Samples	***H_0 (GPa)***	***d_e (μm)***	***LRC***	***H_V (GPa)***
G0	0.200	15.30	0.99935	0.239-0.243
G1	0.201	18.29	0.99982	0.270-0.273
G2	0.204	20.48	0.99958	0.295-0.305
G3	0.216	22.82	0.99949	0.313-0.326

As can be seen from the table, it was observed that the values of H_o of the samples increased slightly but that of d_e increased significantly with increasing the diffusion-annealing time. Quinn *et al* [112] investigated the variation of Vickers microhardness as a function of indentation load for a variety of ceramic materials. They observed that such hardness-load curve shows distinct transition to a plateau of the constant hardness level and concluded that the transition in such curves correspond to the intrinsic hardness value of the material. In this study, this plateau is reached at 2 N applied load for the samples. As can be seen from Table 6.7, true microhardness value of *G0* sample (0.200 GPa) is lower than the hardness results (see Table 6.6) in the plateau region (saturated region) (H_v = 0.239 and 0.243 GPa). This behavior is observed in other samples (*G1*, *G2* and *G3*) in this work. Figure 6.20 shows the true hardness and saturated hardness, H_v (calculated by Eq. (6.12)), as a function of diffusion-annealing time.

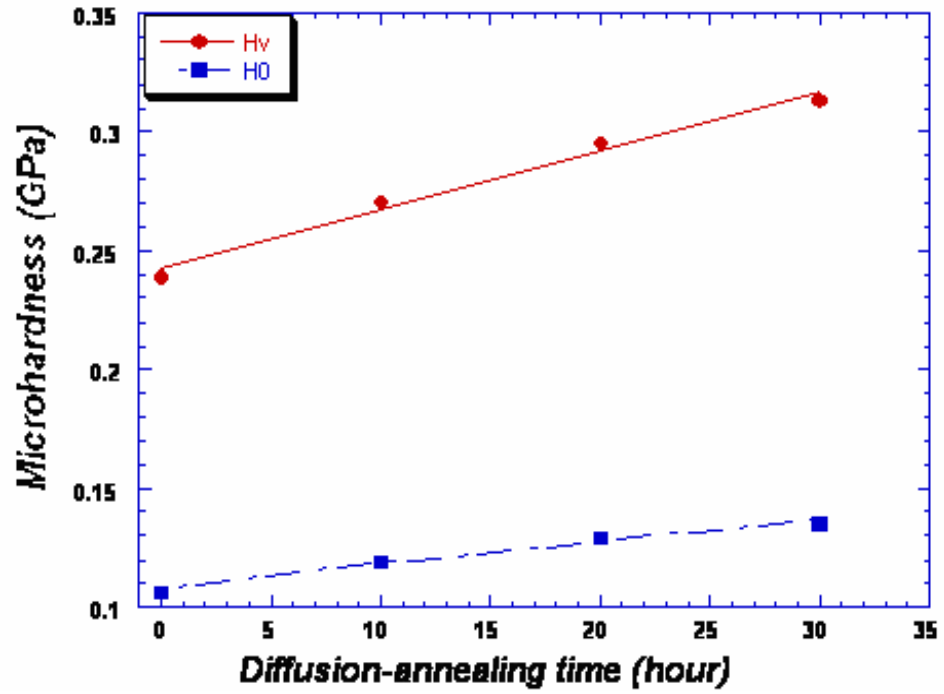

Figure 6.20: True and load dependent microhardness values of the sample calculated by equation (6.12) at 2.940 N.

This result indicates that the true hardness of the sample is lower than that of the traditionally calculated ones. The calculations of H_0 values for the investigated samples also indicated that the magnitude of d_e to be 15 for *G0*, 18-23 μm for *Au* doped samples (*G1*, *G2* and *G3*). These extracted magnitudes of d_e infer that the amount of relaxation of diagonal length is significant with respect to the measured diagonals at low indentation loads [113] and hence the ISE is pronounced for the low load range. This method has been applied to *YBaCuO* and *BiPbSrCaCuO* [101, 113] materials but consistency was not very good.

The second method considers energy dissipative processes during the indentation rather than elastic processes. In this model, a true microhardness can be defined by subtracting a dissipative part, F_0, from the applied load [101].

$$H_0 = 1854.4\left(\frac{F - F_0}{d^2}\right) \qquad (GPa) \tag{6.14}$$

Figure 6.21 exhibits applied load as a function of the square of the diagonal length for the samples. Each set of data shows an excellent linear relationship ($LRC \succ 0.99996$). The slope of each line corresponds to the load independent hardness constant, H_0 and the intercept of each line represents the sample resistance pressure, F_0. The extracted values of F_0, H_0 and *LRC* were listed in Table 6.8. As can be seen from this table, the values of F_0 and H_0 of the samples increased with increasing the diffusion-annealing time and the *LRC* of each sample is very high, implying that Eq. (6.14) provides a satisfactory description of the indentation data for the samples.

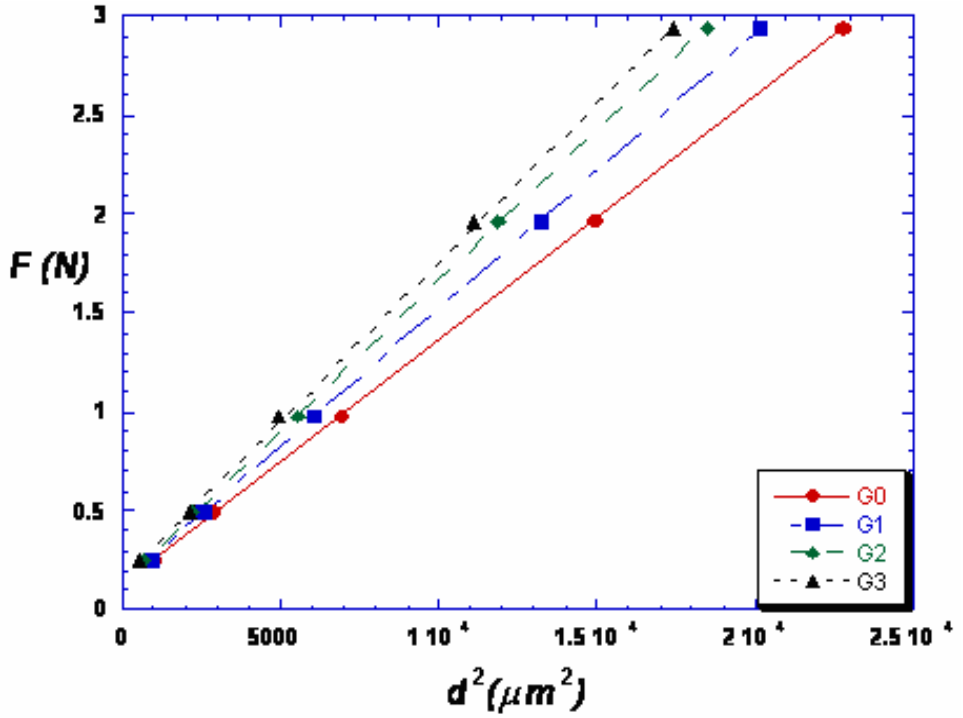

Figure 6.21: Graph of the applied load against the square of the diagonal length for the samples.

Table 6.8: Best-fit results of experimental data according to equation (6.14).

Samples	H_0 *(GPa)*	F_0 *(N)*	*LRC*
G0	0.123	0.128	0.99998
G1	0.138	0.131	0.99998
G2	0.152	0.145	0.99996
G3	0.160	0.166	0.99986

The energy dissipation model is also supported in our work by Figure 6.22, which shows typical impression of *G1* sample for a load 0.98 N.

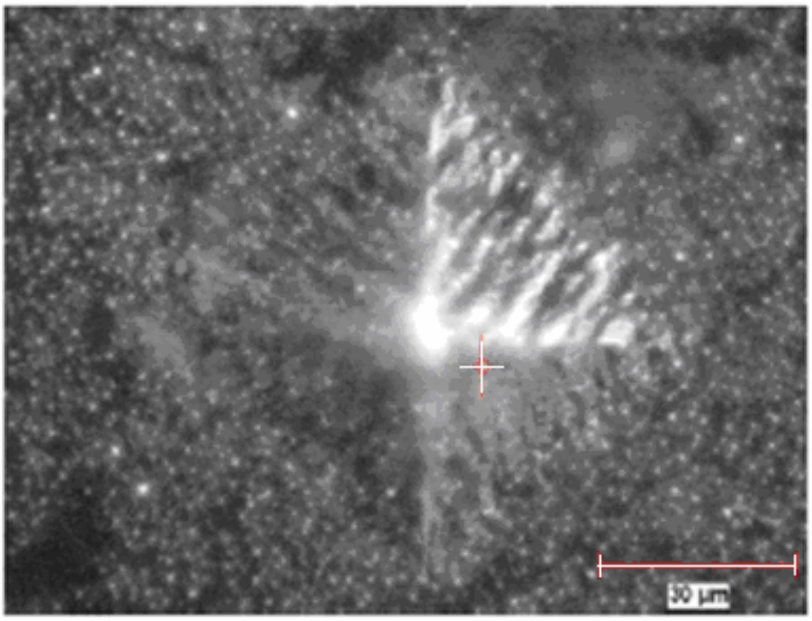

Figure 6.22: Typical indentation for an applied load of 0.980 N for the *G1* sample.

On the other hand, it is observed that the diagonal length is strongly dependent on the applied load from the experimental observations. This observation is governed by

$$\frac{F}{d} = H_0 d + \gamma \tag{6.15}$$

proposed in [13,107,114]. Figure 6.23 exhibits the values of F/d against the diagonal length of indentation, d, for the samples. Each set of data shows an excellent linear relationship. The slope of each line corresponds to the true hardness, H_0 and the intercept of each line represents the surface energy, γ. The extracted values of H_0, γ and *LRC* were listed in Table 6.9. It was observed that the values of H_0 and γ of the all samples increased with increasing the diffusion-annealing time. This observation is

ascribed to the dissipation of the energy of cracks at the interfaces [101] and a similar behaviour in ceramics was also reported in indentation works [13, 69, 115].

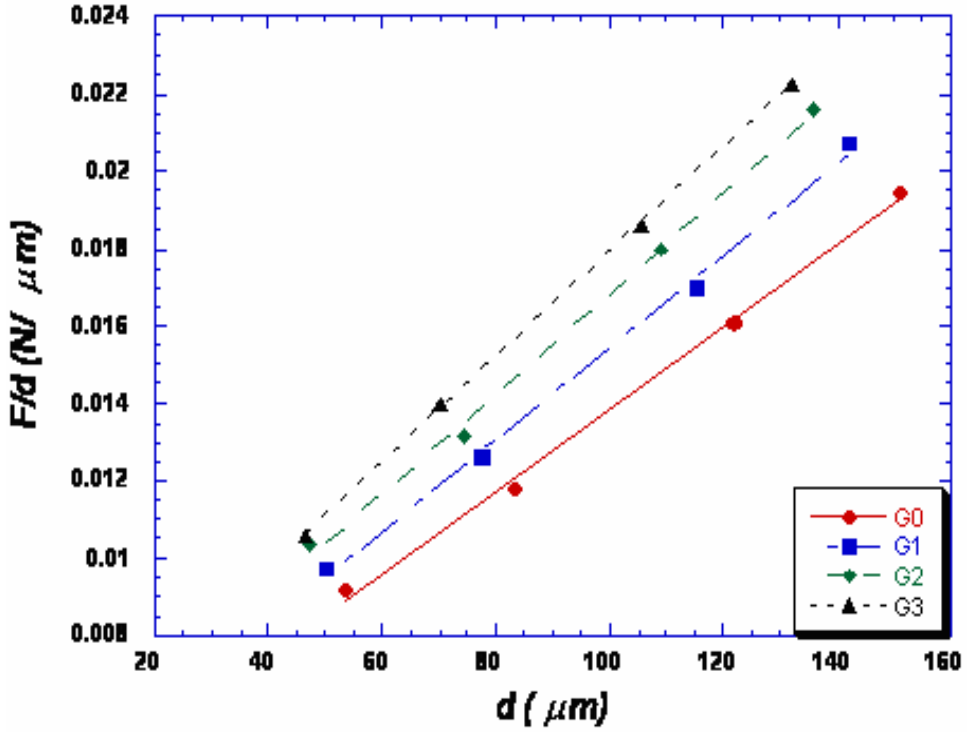

Figure 6.23: Plots of *F/d* versus *d* for the samples.

Table 6.9: Best-fit results of experimental data according to equation (6.15).

Samples	***H_0 (GPa)***	***γ x10^{-3} (N/ μm)***	***LRC***
G0	0.106	3.211	0.9990
G1	0.119	3.523	0.9990
G2	0.129	3.926	0.9990
G3	0.135	4.392	0.9998

In most materials, the elastic modulus (Young's modulus), *E,* is related to the Vickers microhardness (apparent) by the relation [73]

$$E \approx 81.2 H_v, \tag{6.16}$$

and yield strength Y is related to the hardness by the relation [75-76]

$$Y \approx H_v/3. \tag{6.17}$$

The value of load dependent E and Y were calculated for each load by using Eqs. (6.16) and (6.17), and summarized in Table 6.6. As seen in this table, the load dependent E and Y increase significantly with increasing diffusion-annealing time and decreasing loads. This behavior is due to crack initiation and improvement of microhardness. Similar changes in the yield strength and elastic modulus were reported in the literature [73]. This indicates that the diffusion-annealing hardens the superconductor materials further with longer durations. When *Cu* is partially substituted by *Au*, interplayer bonding is strengthened as confirmed by the increase in H_v, E and Y values.

It is useful to mention the fracture toughness, K_{IC}, as it is one of the main mechanical properties of superconducting samples. The fracture toughness is an important parameter for the selection of materials for applications. Due to the nature of intrinsic brittleness, microindentation may result in microfracture around the impressed region on the surface of the samples [76]. Since microfracture occurs mainly during the loading a portion of the energy, which is used to create the indentation deformation, will be dissipated by the crack formation. Owing to the definition of the K_{IC} as the critical stress intensity factor, it is directly related to γ of the crack faces

$$K_{IC} = \sqrt{2E\gamma}. \tag{6.18}$$

where E is the load dependent Young's modulus. The values of load dependent K_{IC} were calculated by using Eq. (6.18) and summarized in Table 6.6. From this table, it is observed that K_{IC} increases significantly with increasing diffusion-annealing time and decreasing loads. Similar change in the fracture toughness was reported in the literature [69]. Owing to this relation, an increase in K_{IC} corresponds to an increase in the average surface energy as proposed from the hardness calculations. From the values of K_{IC} and microhardness, one can calculate the brittleness index, B_i, using the relation [116]

$$B_i = H_v / K_{IC}. \tag{6.19}$$

The calculated values of load dependent B_i for each load is listed in Table 6.6. From the table, it was observed that the brittleness index is load dependent up to 2 N and then remains close to a saturation value at higher applied loads for all samples. One should point out that the apparent microhardness, Young's modulus, yield strength, fracture toughness and brittleness index of the samples in the present work indicate strong dependency on applied load.

In addition, we focused on load independent values of Young's modulus, yield strength, fracture toughness and brittleness index of the samples. Instead of using apparent microhardness (H_v) values to calculate load dependent Y, E, K_{IC} and B_i in Eqs. (6.16)-(6.19) for each load, one can calculate E, Y, K_{IC} and B_i using true microhardness (load independent, H_0) calculated by Eq. (6.15) for each sample. The

obtained load independent Y, E, K_{IC} and B_i for the samples are tabulated in Table 6.10.

Table 6.10: The calculated load independent H_0, E, Y, K_{IC}, and B_i for the samples.

Samples	***H_o (GPa)***	***E (GPa)***	***Y (GPa)***	***K_{IC} ($Pa/m^{1/2}$)***	***B_i ($m^{1/2}$)***
G0	0.106	8.688	0.035	236.2	13.59
G1	0.119	9.754	0.040	262.1	13.44
G2	0.129	10.57	0.043	288.1	13.63
G3	0.135	11.07	0.045	311.7	14.09

From the table, it was observed that the load independent values of E, Y, K_{IC} increase significantly while that of B_i increase slightly with increasing the diffusion annealing duration. Comparing Tables 6.6 and 6.10, one can conclude that the load independent values are lower than that of load dependent values. This is in agreement with the literatures [101, 117]. The above results revealed that by increasing the diffusion-annealing duration, it is possible to control the mechanical properties of the samples. The improvement of mechanical properties is due to the fact that *Au* can fill the intergrain spaces, and thereby reinforces the coupling between granules.

The indenter gives geometrically similar indentation; hence it follows that the measured hardness must be independent of the applied load. However, it has been well known that for many materials, microhardness calculated using Eq. (6.12) is load dependent. In general, higher applied loads lead to lower hardness values. Such a phenomenon is known as the indentation size effect (ISE).

To account for this effect, several relationships between the applied load and the resulting indentation size have been suggested [107-110]. In order to explain the ISE behaviour of our samples, Mayer's law can be used [118-120]

$$F = Ad^n \tag{6.20}$$

where the power n is the Meyer number, and A is the standard hardness constant. The value of n is used as a measure of ISE. When $n \prec 2$, the hardness increases with decrease of the applied load. In the case of $n \succ 2$, the hardness increases with increasing the applied load. The hardness is independent of applied load when $n_k = 2$ and in this case the relation between applied load and diagonal indentation is given by $F = A_{1K} d^2$ (Kick's law). In most cases, Kick's law is hardly met because the exponent n is less or larger than 2. Figure 6.24 represents the plots of ln$F$ versus ln$d$ for the samples.

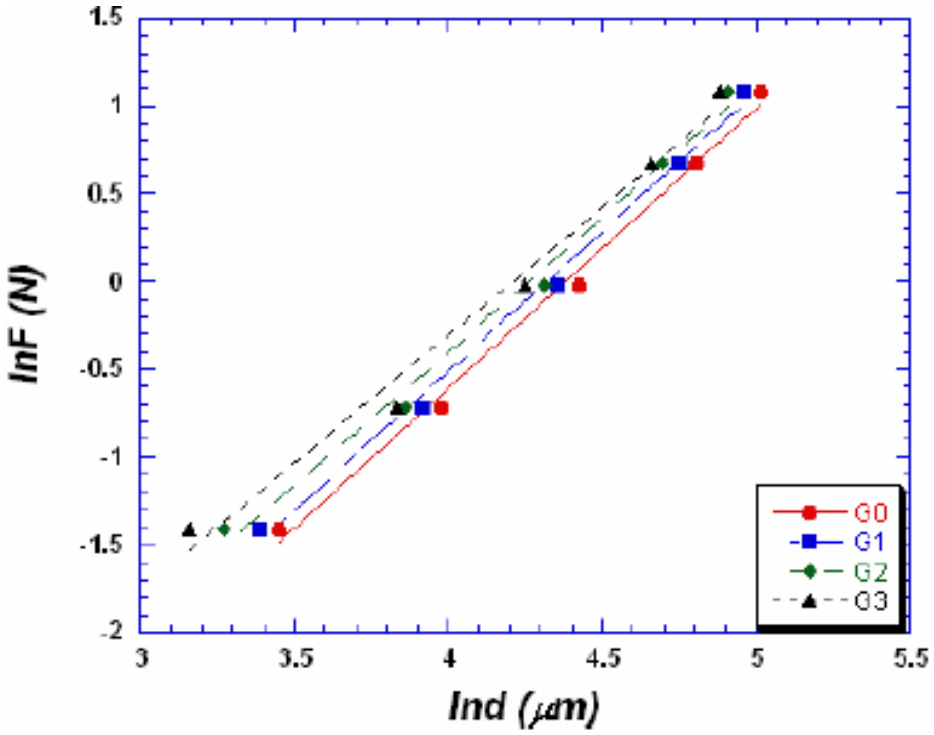

Figure 6.24: Variation of applied load ln$F$ with diagonal ln$d$ for the samples.

The slope of the graph is proportional to n_k and that of vertical intercept is proportional to A_{1K}. Trough linear regression analyses, the values of n_k, A_{1K} and R (the regression coefficient) were obtained and the results are tabulated in Table 6.11. As can be seen from the table, each set of the data did not exhibit an excellent linear relationship ($R \prec 0.997$), and that of n_k is less than 2. According to our results ($n \prec 2$), our samples do not obey Kick's law. Kick's law can explain the ISE of our data qualitatively, but physical significance of the parameter A_{1K} is still not well understood because this law is just an empirical one.

Table 6.11: Best-fit results of experimental data according to equation (6.20).

Sample	Meyer number n_K	$\ln A_{1K}$ (GPa)	Regression of coefficient (R)
G0	1.589	-6.967	0.99719
G1	1.592	-6.879	0.99749
G2	1.521	-6.480	0.99531
G3	1.457	-6.134	0.99260

The PSR model has been recently performed on several materials to account the ISE [70] According to the PSR model, this behaviour is governed by

$$F = W_{PSR}d + A_{1PSR}d^2 \tag{6.21}$$

The coefficient of W_{PSR} and $A_{1\mathrm{PSR}}$ correspond to the load dependent hardness and the load independent hardness, respectively. Rearranging Eq. (6.21), it can be written as

$$\frac{F}{d} = W_{PSR} + A_{1PSR}d \tag{6.22}$$

When examining the load-dependence of microhardness of the samples measured in a wide range, it was found that the resultant *F/d* versus *d* curves showed significant non linearity and it was argued that the PSR model mentioned above may only be used to represent the experimental data in a narrower range of applied loads.

A modified proportional specimen resistance (MPSR) model has recently proposed in order to explain the ISE behaviour [110]. According to this modified model,

$$F = W_{MPSR} + A_{0\,MPSR}d + A_{1MPSR}d^2 \tag{6.23}$$

where W_{MPSR} corresponds to minimum applied load to produce an indentation, A_{0MPSR} and A_{1MPSR} are related to the energies dissipated for creating a new surface of a unit area and for producing the permanent deformation of a unit volume, and is a measure of the load independent hardness estimated by MPSR model, respectively. Figure 6.25 shows *F* versus *d* graph for the samples. From a conventional polynomial fit of this expression (Eq. (6.23)) to the data, the parameters of W_{MPSR}, A_{0MPSR}, A_{1MPSR} and *R* were extracted for all samples and tabulated in Table 6.12. According to the MPSR model, the load independent hardness can be calculated by relation,

$$H_{\mathrm{MPSR}} = 1854.4\ A_{\mathrm{MPSR}} \tag{6.24}$$

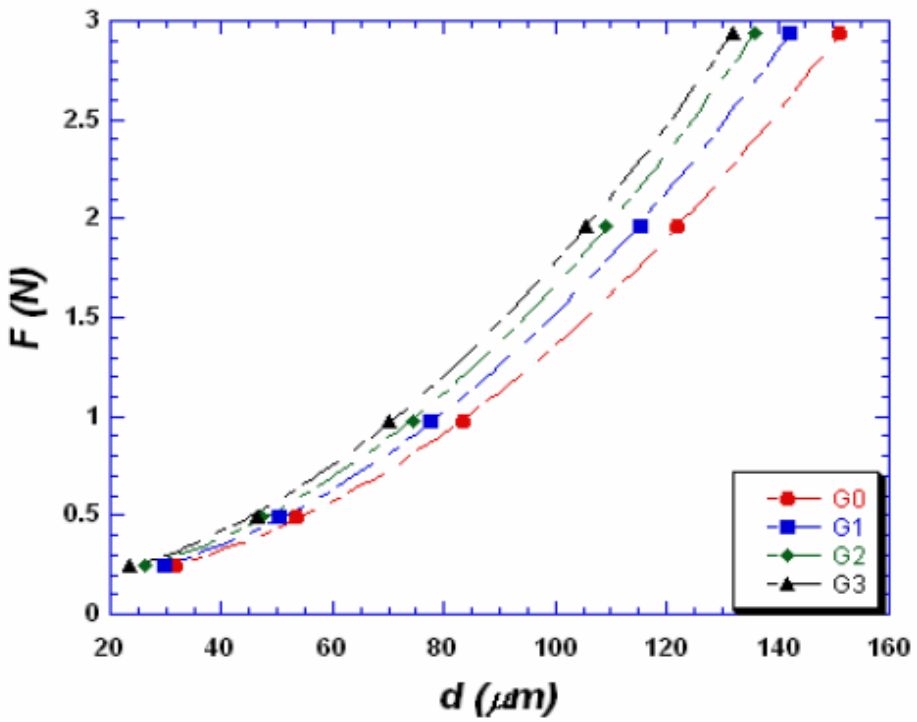

Figure 6.25: Variation of applied load with the indentation diagonal length for the samples.

Table 6.12: Best-fit results of experimental data according to equations (6.23) and (6.24).

Sample	W_{MPSR} (N)	A_{0MPSR} (N/μm)	A_{1MPSR} ($N/\mu m^2$)	Regression of coefficient (R)	Load independent hardness H_{LMPSR} (GPa)	Load dependent hardness (in plateau regime) H_V(GPa)
G0	0.129	-2.46×10^{-5}	12.33×10^{-5}	0.99998	0.229	0.239-0.243
G1	0.123	21.5×10^{-5}	13.77×10^{-5}	0.99994	0.255	0.270-0.273
G2	0.113	44.2×10^{-5}	14.89×10^{-5}	0.99997	0.276	0.295-0.305
G3	0.111	178×10^{-5}	15.35×10^{-5}	0.99992	0.285	0.313-0.326

The calculated load independent hardness for each sample is listed in Table 6.12. As can be seen from the table, load independent microhardness value of *G0* sample (0.229 GPa) is closer to the hardness results in the plateau region (H_v = 0.239 and 0.243 GPa). The MPSR model also provides a description for measured indentation data.

Hays and Kendal [109] proposed a concept that there exist minimum levels of the applied test load, W_{HK}, named minimum applied load to produce an indentation. They introduced an effective indentation load, $F_{eff} = F - W_{HK}$, and proposed the following relationship (modified Kick's law),

$$F - W_{HK} = A_{1HK} d^2 \tag{6.25}$$

where A_{1HK} is the load independent hardness constant calculated by HK approach for a given sample.

Figure 6.26 exhibits applied load as a function of the square of the impression semidiagonal for the samples. Each set of data shows an excellent linear relationship ($R \succ 0.99996$). The slope of each line corresponds to the load independent hardness constant, A_{1HK} and the intercept of each line represents the sample resistance pressure, W_{HK}. The extracted values of W_{HK}, A_{1HK} and R were listed in Table 6.13. As can be seen from the table, it was observed that the values of W_{HK} and A_{1HK} of the samples increased with increasing the diffusion-annealing time and the regression coefficient of each sample is very high, $R \succ 0.99996$, implying that Eq. (6.25) provides a satisfactory description of the indentation data for the samples.

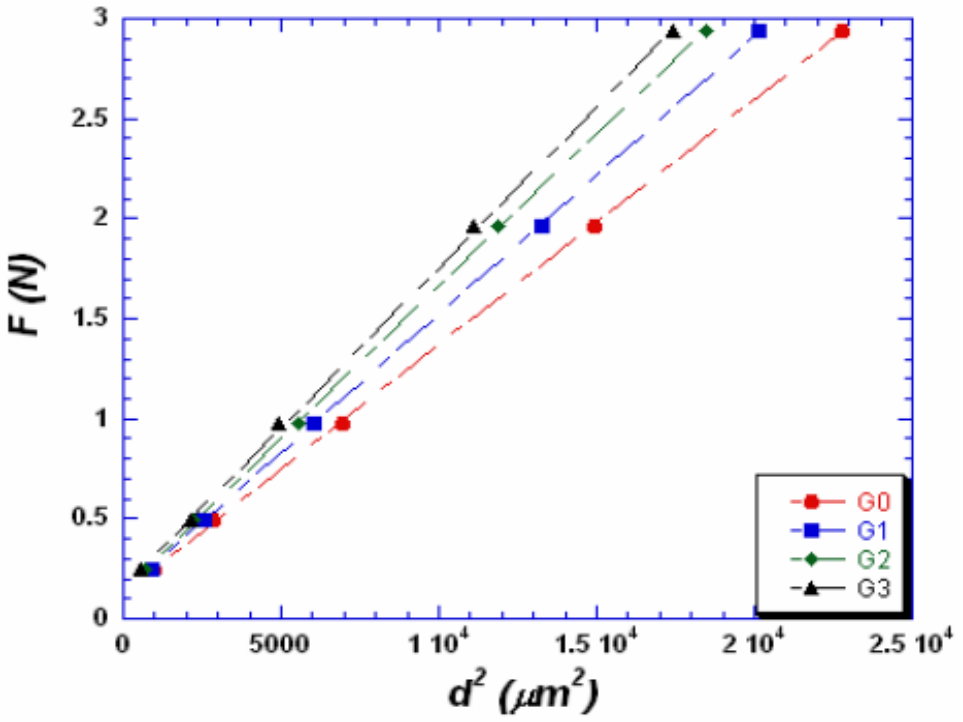

Figure 6.26: Applied load vs. the square of the impression semi-diagonal length for the samples.

Table 6.13: Best-fit results of experimental data according to equations (6.25) and (6.26).

Sample	Load independent hardness A_{1HK} (GPa)	Sample resistance pressure W_{HK} (N)	Regression of coefficient (R)	n_{HK}	Regression of coefficient (R)	Load independent hardness H_{LHK} (GPa)	H_V(GPa)
G0	12.32×10^{-5}	0.128	0.99998	2.018	0.99985	0.229	0.239-0.243
G1	13.89×10^{-5}	0.131	0.99994	2,020	0.99980	0.258	0.270-0.273
G2	15.16×10^{-5}	0.145	0.99996	2.023	0.99991	0.282	0.295-0.305
G3	16.12×10^{-5}	0.166	0.99983	2.070	0.99982	0.299	0.313-0.326

Figure 6.27 exhibits a plot of ln$(F\text{-}W_{HK})$ versus ln$d$ and gives a value of $n_{HK} \approx 2$ and that of R $\succ$ 0.9998 (see Table 6.13) for all samples.

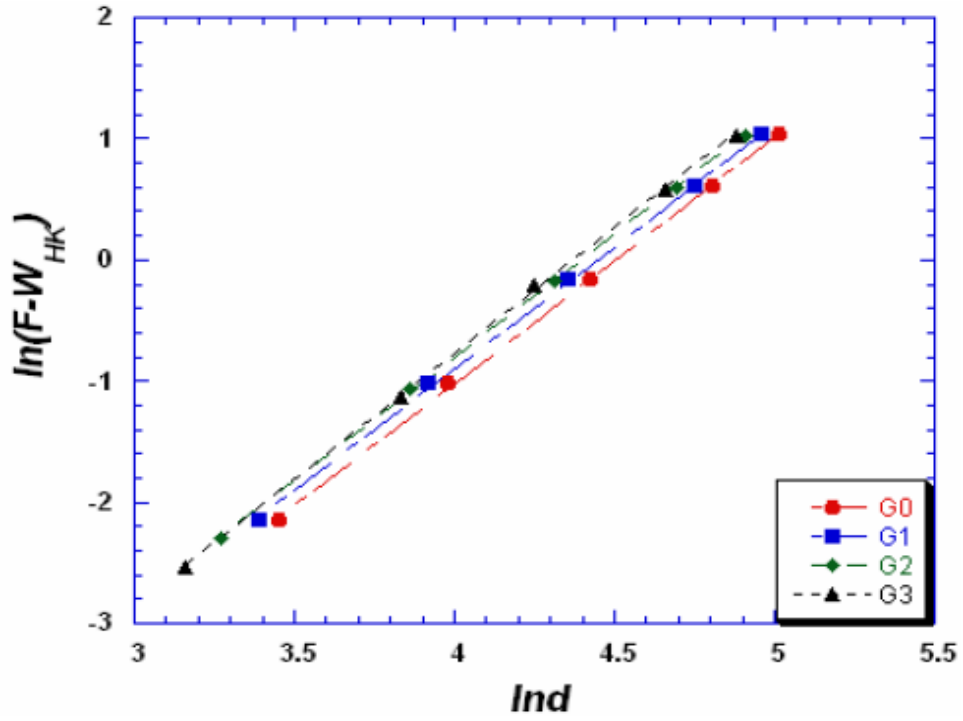

Figure 6.27: Relationship between true applied load ln$(F\text{-}W_{HK})$ and the Vickers diagonal ln$d$ for the samples.

This result confirms the validity of Eq. (6.25) or HK law in the explanation of the dependence of microhardness on applied load. According to the HK approximation, load independent microhardness H_{LHK} can be calculated by relation

$$H_{LHK}=1.8544A_{1HK.} \qquad (6.26)$$

The values of H_{LHK} were calculated by using Eq. (6.26) and summarized in Table 6.13. The load independent hardness values estimated by HK approach (H_{LHK} = 0.229 GPa) and the hardness results of *G0* sample (see table 6.13) in the plateau region (H_v = 0.239 and 0.243 GPa) are comparable. This behaviour is observed in other samples (*G1*, *G2* and *G3*) of this work. The extracted values of W_{HK} were found to vary from 0.128 to 0.166 N. The HK approach also provides a satisfactory description for measured indentation data.

It can be concluded that both the load independent values calculated by MPSR model and that of obtained by HK approach are obviously comparable and closer to plateau value. Therefore, it was found that the load independent microhardness values estimated based on different (MPSR and HK) models, are similar with each other and this comparability was attributed to the similarity between the empirical equations. On the other hand, the estimated value of W_{HK} was generally found too large to be accepted [121], being consistent with the present work. Therefore, the HK approach is not convenient for describing the microindentation data. At the same time, the estimated value of A_{0MPSR} listed in Table 6.12 is negative that has no physical meaning. This result also implies that the MPSR model cannot provide a satisfactory explanation for the samples. Based on the above explanations, we concluded that the indentation size effect is a rather complex phenomenon and cannot be analyzed based on a unique mechanism. In this work, a much high the regression coefficient was obtained for both models when analyzing the indentation data but the resultant best fit values of the parameters included in these equations cannot be explained satisfactorily based on the models.

The possible reasons for the observed enhancement in mechanical properties due to *Au* diffusion are discussed. The experimental results of hardness measurements were analyzed using the Kick's law, modified proportional specimen resistance (MPSR) model and the Hays-Kendall (HK) approach. Among them HK approach was the most successful.

CHAPTER 7

CONCLUSIONS

$Bi_{1.8}Pb_{0.35}Sr_{1.9}Ca_{2.1}Cu_3O_y$ samples were prepared by using solid-state reaction method. We determined the effect of gold diffusion-doped and diffusion annealing time in the *Bi(Pb)SrCaCuO* superconductor samples by a low AC field susceptibility, investigation of XRD patterns, surface morphology (SEM), room temperature resistivity, critical temperature, critical current density, and microhardness measurements. All results from our investigations indicate that improved in crystalline structure, superconducting and mechanical properties of the *Au*-doped samples.

When *Au*-doped samples of $Bi_{1.8}Pb_{0.35}Sr_{1.9}Ca_{2.1}Cu_3O_y$ phase, are compared with those for the undoped sample, following statements are concluded for doped samples:

- It is observed that for diffusion of *Au* atoms in $Bi_{1.8}Pb_{0.35}Sr_{1.9}Ca_{2.1}Cu_3O_y$ in the temperature range 500-800 $^{\circ}C$, the coefficient of diffusion increases from 2 x 10^{-10} cm^2s^{-1} to 1.2 x 10^{-8} cm^2s^{-1}, the corresponding activation energy being 1.08 eV for calculation from the lattice parameter *c*. The coefficient of diffusion increases from 1.9 x 10^{-10} cm^2s^{-1} to1.6 x 10^{-8} cm^2s^{-1}, the corresponding activation energy being 1.08 eV for calculation from the conductivity. The low value of the activation energy indicates that the *Au* diffusion proceeds through defects in the ceramic samples.
- The lattice parameter *c* and the high-T_c phase ratio increase.

- The denser microstructure of the surface morphology is obtained.
- The critical transition temperature increases.
- The decrease in the normal state resistivity.
- The critical current densities of the Au-doped samples were increased with increasing the diffusion-annealing duration.
- The increase in carrier concentration.
- Au doping increased the high-T_c phase, decreased the low-T_c phase
- The improvement of superconducting properties is due to the modification of grain boundaries by *Au* doping with increasing diffusion-annealing time.
- It was observed that the overall susceptibility curves of the samples are shifted to lower temperature by increasing the AC field amplitude. The shift is related to the pinning force strength.
- The intensity of the imaginary parts increased with increasing the AC field amplitude.
- The intergrain critical temperature T_p is linear as function of the AC field amplitude for all samples and agrees with the Müller critical state model.
- The improvement of mechanical properties can be observed by the increase of microhardness with *Au* doping and increasing diffusion annealing time.
- The estimated apparent microhardness, Young's modulus, yield strength and fracture toughness values of the samples are load dependent. Their variation with load is non-linear.
- Load independent hardness values are more reasonable than the values obtained from the traditional definition of Vickers formula for one applied load.
- The load independent H_0, E, Y, K_{IC} and B_i can be calculated directly using Eq. (6.15).

- The load dependent values of H_v, E, Y, K_{IC} and B_i are greater than that of load independent values.
- HK approach involving the concept of sample resistance pressure can explain the ISE.
- Among the other models employed in this thesis, the HK approach is suitable for describing the experimental data.

7.1 Future Works

The fallowing future experiments are suggested:

- We are planning the perform EDXRF (Energy dispersive X-ray fluorescence) measurements on the same sample to investigate *Au* diffusion in $Bi_{1.8}Pb_{0.35}Sr_{1.9}Ca_{2.1}Cu_3O_y$ and to calculate diffusion coefficient and compare these results with previous calculations.
- A review article will be written on *Au* diffusion in $Bi_{1.8}Pb_{0.35}Sr_{1.9}Ca_{2.1}Cu_3O_y$.
- To cover Scientific and Technological Council of Turkey (TUBITAK) project, the same investigations will be performed on *Fe* diffusion-doped in $Bi_{1.8}Pb_{0.35}Sr_{1.9}Ca_{2.1}Cu_3O_y$.

REFFERENCES

[1] Kittel, C., Introduction to Solid State Physics. John Wiley & Sons, Inc., New York, London, Sydney (1986).

[2] Onnes, H. K., Superconductivity and Magnetism. Comm. Phys. Lab. Univ. Leiden, (1911), 119-120.

[3] Meissner, W.Ochsenfeld, R., Upper Critical Fields of High-T_c Superconducting Y-Ba-Cu-O, Nature ,**132** (1933), 931-935.

[4] Bednorz, J.G., Muller, K.A., Possible High T_c Superconductivity in the Ba-La-Cu-O System, Z.Phys., **64** (1986), 189-193.

[5] Wu, M.K., Ashburn, J.R., Torng, C., Superconductivity at 93 K in a New Mixed-Phase Y-B-Cu-O Compound System at Ambient Pressure, Phys.Rev.Lett. **58**, 9 (1987), 908-910.

[6] Michel, C., Superconductivity in Bi-Sr-Ca-Cu-O System, Z. Phys. B, Condensed Matter **68**, (1987), 421-423.

[7] Maeda, H., Taraka, Y., Measurement of the Normal State Anisotropic Resistivity of Single Crystal Bi-Sr-Ca-Cu-O, Jpn.Appl.Phys., **27**, 2 (1988), L209-L211.

[8] Tokano, K., Properties of Pb-Doped Bi-Sr-Ca-Cu-O Superconductors, Appl. Phys. Lett., **53,14**, (1988), 1329-1331.

[9] Terzioglu, C., Yilmazlar, M., Ozturk, O., Yanmaz, E., Structural and physical properties of Sm-doped $Bi_{1.6}Pb_{0.4}Sr_2Ca_{2-x}Sm_xCu_3O_y$, Physica C, **423** (2005), 119.

[10] Kambe, S., Guo, Y.C., Dou, S.X., Liu, H.K., Wakahara, Y., Maeda, H., Kakimoto, K., and Yavuz, M., Supercond. Sci. Technol., **11** (1998), 1061.

[11] Kambe, S., Guo, Y.C., Dou, S.X., Liu, H.K., Proc. R. Soc. London **96**, (1996) 454.

[12] Serway, R. A., Physics for Scientists and Engineers, Thomson Brooks/Cole, (1992).

[13] Yilmazlar, M., Cetinkara, H.A., Nursoy, M., Ozturk, O., and Terzioglu, C., Thermal Expansion and Vickers Hardness of $Bi_{1.6}Pb_{0.4}Sr_2Ca_{2-x}Sm_xCu_3O_y$ Superconductors, Physica C **442**, (2006) 101.

[14] Pissas, M., Niarchos, D., Chiristides, C., Anagnostou, M., The optimum percentage of Pb and the appropriate thermal procedure for the preparation of the 110-K $Bi_{2-x}Pb_xSr_2Ca_2Cu_3O_y$ superconductor Supercon. Sci. Tech. Vol.**3**, (1990), 128.

[15] Nkum, R.K., Datars, W.R, Substitution of Sn in the superconducting Bi-Pb-Sr-Ca-Cu-O system, Physica C, **190,** (1992), 465.

[16] Dzhafarov, T.D., Yilmazlar, M., The effect of Ag electromigration on the properties of BiPbSrCaCuO superconductors, Physica C, **292,** (1997), 140-146.

[17] Prabitha, V.G., Biju, A., AbhilashKumar, R.G., Sarun, P.M., Aloysius R.P., Syamaprasad, U., Effect of Sm addition on (Bi,Pb)-2212 superconductor, Physica C, **433,** (2005), 28.

[18] Terzioglu, C., Ozturk, O., Kilic, A., Gencer, A., and Belenli, I., Effect of cooling rates on bare bulk and silver wrapped pellets of Bi-2223, superconductor Physica C, **434,** (2006), 153.

[19] Hua, L., Yao, G.Z., Jiang, M., Wang, Y.Z., Tang, H., and. Li, Z.R, Study Of Ag/Oxide Interface Of Bi-2223 Silver-Sheathed Superconducting Composite, J. Appl. Phys., **78,** (1995), 3274.

[20] Yu, Y., Jin, X., Din, S.Y., Zhen, Z.Y., et al., The Superconductivity Of $Bi_{1.7}Pb_{0.3}Sr_{2-X}Ag_xCa_2Cu_3O_y$, Phys. Stat. Sol., **151,** (1995), 9.

[21] Matsushita, T., Suzuki, A., Kishida, T., Okuda, M., and Naito, H., The Effect Of Ag On The Superconductıvıty Of $Bı_{2-X}Pb_xSr_2Ca_2Cu_3O_y$ Superconductors Prepared By An Optımum Thermal Procedure, Supercond. Sci. Technol., **7,** (1994,) 222.

[22] Cömert, H., Altunbaş, M., Dzhafarov, T.D., Küçükömeroğlu, T., Asadov, Y.G., and Karal, H., The effect of ag dıffusıon on the crystal-structure and electrıcal-propertıes of Bi(Pb)srcacuo superconductors, Supercond. Sci. Technol., **7,** (1994), 824.

[23] Jeong, D.Y., Sohn, M.H., Ha, D.W., Dependence of superconducting properties and microstructure on heat treatment in Ag-sheathed Bi-Pb-Sr-Ca-Cu-O tapes, Physica C, **185-189,** (1991), 2487.

[24] Dzhafarov, T.D., Cömert, H., Altunbaş, M., Alver, Ü., Küçükömeroğlu T., and Kopya, A.Y., Diffusion of Ag in Bi(Pb)-Sr-Ca-Cu-O superconductors, J. Alloys Comp., **221,** (1995), 246.

[25] Lee, H. G., Hong, G. W., Kim, J. J., and Song, M. Y., Role of silver on phase-formation and texture development in Ag/BSCCO composites, Mat. Lett., **23,** (1995), 65.

[26] Chin, J.D., Kao, C.H., Lei, T.S., and Wu, M.K., Effect of Ag_2O on the formation of high-T_c phase in the BPSCCO/Ag_2O composites, Physica C, **235-240**, (1994), 485.

[27] Görür, O., Terzioglu, C., Varilci, A., and Altunbaş, M., Investigation of some physical properties of silver diffusion-doped YBa2Cu3O7-x superconductors, Supercond. Sci. Technol., **18**, (2005), 1233.

[28] Jin, S., Sherwood, R.C., Tiefel, T.H., Kammlott, G.W., Superconductivity in the Bi-Sr-Ca-Cu-O compounds with noble-metal additions, Appl. Phys. Lett., **52**, (1998), 1628.

[29] Liu, H.K., Dou, S.X., Song, K.H., and Sorrell, C.C., Superconducting properties of Au/Bi-Pb-Sr-Ca-Cu-O composites, Supercond. Sci. Technol., **3**, (1990), 210.

[30] Grivel, J. C., and Flukiger, R., Effects of Au and Ag additions on the formation of the Bi(2223) phase, Physica C, **229**, (1994), 177.

[31] Dzhafarov, T.D., Altunbaş, M., Varilci, A., Küçükömeroğlu, T., and Nezir, S., Superconducting properties of gold-diffusion doped BiPbSrCaCuO, Solid State Comm., **99**, (1996), 839.

[32] Omar, M.A., Elementary Solid State Physics. Addison-Wesley Publishing Company (1993).

[33] Aschroft, N. W. and Mermin, N. D., Solid State Physics. W. B. Sounders Company, USA (1976).

[34] Halley, J.W., Theories of High Temeperature Superconductivity, Addison-Wesley Publishing Company (1988).

[35] Ibach, H. and Luth, H., Festkorperphysik, Third Edition (1990).

[36] Christman, J.R.,Fundementals of Solid State Physics, John Wiley & Sons(1988).

[37] Kishio, K., Kitazawa, K., Kanbe, S., Yasuda, I., Sugii, N., Takagi, H., Uchida, S., Fueki, K. and Tanaka, S., New high-temperature superconducting oxides - $(La_{1-X}Sr_X)_2CuO_{4-Delta}$ and $(La_{1-X}Ca_X)_2CuO_{4-Delta}$, Chem.Lett., **24,** (1987), 429.

[38] Gubser, D.U., Hein, R.A., Lawrence, E.H., Osafsky, M.S., Schrodt, D.J.,Toth, L.E. and Wolf, S.A., Phys.Rev.B, **35**, (1987), 5350.

[39] Grant, P.M., Beyers, M.B., Engler, E.M., Lim, G., Parkin, S.S.P.,Ramirez, M.L., Lee, V.Y., Nazzal, A., Vazquez, J.E. and Sovay, R.J., Superconductivity Above 90 K in the Compound $YBa_2Cu_3O_{7-x}$, Phys.Rev.B, **35**, 13 (1987), 7242-7244.

[40] Quadri, S.B., Toth, L.E., Osofsky, M., Lawrence, S., Gubser, D.U., and Wolf, S.A., X-ray identification of Supercunducting High T_c Phase in Y-Ba-Cu-O System, Phys. Rev. B, **35**, 13 (1987), 7235-7237.

[41] Hwu, S.J., Song, S.N., Thiel, J., Poeppelmeier, K.R., Ketterson, J.B. and Freeman, A.J., High T_c superconductivity in Regions of Possible Compound Formation, Phys. Rev. B, **35**, 13 (1987), 7119-7121.

[42] Tarascon, J.M., Green, L.H., McKinnon, W.R., and Hull, G.W., Superconductivity at 90K in Multiphase of Y-Ba-Cu-O, Phys.Rew.B, **35**, 13 (1987), 7115-7117.

[43] Kikuchi, M., Syono, Y., Tokiwa, A., Oh-Ishi, K., Arai, H., Hiraga, K., Kobayashi, N., Sasaoka, T. and Muto,Y., Thermal and X-ray Analyses of High Temperature Superconductor $YBa_2Cu_3O_{6.74}$, Jpn.Appl.Phys., **26**, 6 (1987), L1066-L1069.

[44] Hor, P.H., Meng, R.L., Wong, Y.q., Gao, L., Huang, Z.J., Bechtold, J., Forster, K. and Chu, C.W., Superconductivity above 90 K in the square-planar compound system $ABa_2Cu_3O_{6+x}$ with A = Y, La, Nd, Sm, Eu, Gd, Ho, Er, and Lu, Phys.Rev.Lett., **58**, (1987), 1891.

[45] Moodenbaugh, A.R., Suenaga, M., Asano, T., Shelton, R.N., Ku, H.C., McCallum, R.W. and Klawins, Superconductivity near 90-K in the Lu-Ba-Cu-O system, P., Phys.Rev.Lett. **58**, (1987), 1885.

[46] Quidwai, Ansar A.,et al., Supercond.Sci.Technol.,**5**, (1992), 602-604.

[47] Kilic, A., Master Thesis, University of Ankara, (2000).

[48] Nagamatsu, J., Nakagawa, N., Muranaka, T., Zenitani,Y., Akimitsu, J., Superconductivity at 39K in Magnesium Diboride, Nature, **410**, (2001), 63-64.

[49] Glasso, F.S., Perovskite Type Compounds and High T_c Superconductor, Jurnal of Metals, **8**, (1987), 10.

[50] Torrance, J.B., , Tokura, Y., Laplaca S., Huang, T.C., Savoy, R.J., Nazzal, A.I., New Class Of Hıgh-Tc Structures - Intergrowth Of Multiple Copper-Oxide Perovskıte-Lıke Layers Wıth Double Sheets Of Bıo Solide State Communications, **66**, (1988), 703-706.

[51] Koyama, S. et al., Preparation of single 110 K phase of the Bi-Pb-Sr-Ca-Cu-O superconductor, Jpn. J. Appl. Phys., **27**, (1988), L1861-L1863.

[52] Abdullaev G.B., Dzhafarov T.D., Atomic Diffusion in Semiconductor Structures, Harwood academic publishers, Chur, London, Paris, Newyork, (1987).

[53] Enger, E.M., Chemtech. **17**, (1987), 542.

[54] Goldfarb, R.B., Lelental, M. and Thompson, C.A. Magnetic Susceptibility of Superconductors and Other Spin Systems, ed: R A Hein, T L Francavilla and D H Liebenberg, New York: Plenum, (1992).

[55] Supple, F., Campbell, A. M. and Cooper, J. R., An investigation of the irreversibility line in $Bi_2Sr_2CaCu_2O_8$ single crystals, Physica C, **242**, (1995), 233.

[56] Flippen, R. B., Askew, T. R., Fendrich, J. A. and Vlcek, B. M., χ'' peaks, flux pinning, and the irreversibility line in high-temperature superconductors, Physica C, **228,** (1994), 85.

[57] Caplin, A. D., Cohen, L. F., Perkins, G. K. and Zhukov, A. A., The electric-field within high-temperature superconductors - mapping the E-J-B surface, Supercond. Sci. Technol., **7,** (1994), 412.

[58] Müler, K. A., Takashige, M. and Bednorz, J. G., Flux trapping and superconductive glass state in La_2CuO_4-Y-Ba, Phys. Rev. Lett., **58,** (1987), 1143.

[59] Malozemoff, A. P., Worthington, T. K., Yeshurun, Y., Holtzberg, F. and Kes, P. H., Remanent moment of high-temperature superconductors - implications for flux-pinning and glassy models, Phys. Rev. B, **38,** (1988), 6490.

[60] Gencer, A., Ph-D Thesis, Birmingham University, (1994).

[61] Brandt, E. H. and Indenbom, M., Type-II-superconductor strip with current in a perpendicular magnetic-field, Phys. Rev. B, **48,** (1993), 12893.

[62] Clem, J. R., Granular and superconducting-glass properties of the high-temperature superconductors, Physica C, **153–155**, (1988), 50.

[63] Kes, P. H., Aarts, J., van den Berg, J., van der Beek, C. J. and Mydosh, J. A., Thermally assisted flux flow at small driving forces, Supercond. Sci. Techno*l.* **1,** (1989), 242.

[64] Shaulov, A. and Bhargava, R., Characterization of Y-Ba-Cu-O thin-films using their nonlinear magnetic response, J. Appl. Phys., **69,** (1991), 6738.

[65] Bean, C. P., Rev. Mod. Phys. **36,** (1964), 31.

[66] Yang, Y., Beduz, C., Yi, Z., and Scurlock, R. G., Transport critical currents and flux pinning in melt-grown $YBa_2Cu_3O_{7-\delta}$, Physica C**, 199,** (1992), 23.

[67] Ji. L., Sohn, R. H., Spalding, G. C., Lobb, C. J. and Tinkham, M., Critical-state model for harmonic-generation in high-temperature superconductors, Phys. Rev. B, **40,** (1989), 10936.

[68] Gencer, A., Mutlu, R.H., Belenli, İ.,Özoğul, Ö. and Aydınuraz, A., A study of the nonlinearity in magnetic response of $Bi_2Sr_2CaCu_2O_8$, Supercond. Sci.Technol., **9,** (1996), 284-289.

[69] Khalil, S.M., Role of rare-earth Ba^{2+} doping in governing the superconducting and mechanical characteristics of Bi-Sr-Ca-Cu-O, Smart Mater. Struct., **14,** (2005), 804.

[70] Khalil, S.M., Enhancement of superconducting and mechanical properties in BSCCO with Pb additions, Journal of Physics and Chemistry of solids, **62,** (2001), 457.

[71] Murakami, A., Katagiri, K., Noto, K., Kasaba, K., Sohoji, Y., Muralidhar, M., Sakai, N., and Murakami, M., Tensile mechanical properties of (Nd,Eu,Gd)–Ba–Cu–O bulk superconductors at room and liquid nitrogen temperatures, Physica C, **378-381**, (2002), 794 .

[72] Katagiri, K., Murakami, A., Kan, R., Kasaba, K., Noto, K., Muralidhar, M., Sakai, N., and Murakami, M., Effects of Ag content on the mechanical properties of (Nd,Eu,Gd)–Ba–Cu–O bulk superconductors, Physica C, **392-396**, (2003), 526.

[73] Veerender, C., Dumke, V.R., Nagabhooshanam, Hardness and elastic-moduli of $Bi_{2-X}Pb_XCa_2Sr_2Cu_3O_y$ superconductors, M., Phys. Status Solid A, **144,** (1994), 299.

[74] McClintock, F.A., Argon, A.S., Mechanical Behaviour of Materials, Addison-Wesley, Reading, MA, pp. 455, (1996).

[75] Tabor, D., The Hardness of Metals, Clarendon, Oxford, (1951).

[76] Lawn, B.R., Atomistic model of kinetic crack growth in brittle solids, J. Mater. Sci. **10** (1975) 469.

[77] Davidge, R.W., Mechanical Behavior of Ceramics, London, Cambridge University Press, pp.31-50, (1979).

[78] Kishore K. N., Muralidhar M. And Babu V. H., Peña, O., Sergent, M., and Bénière, F., Effect of rare-earth Sm^{3+} substitution on the superconducting properties of the $Bi_{1.7}Pb_{0.3}Sr_2Ca_{2-x}Sm_xCu_3O_y$ system, Physica C**, 204** (1993), 299.

[79] Ilyusechkin A. Y., Yamashita T., Boskovic L. And Mackinnon I. D. R., The effect of Yb addition in $Bi_2Sr_2Ca_{1-x},Yb_xU_2O_y$ partial melted thick films, Supercond. Sci. Technol., **17,** (2004), 1201.

[80] Biju A., Aloysius R. P., Sayamaprasad U., Enhanced critical current density in Gd-added (Bi, Pb)-2212 bulk superconductor, Supercond. Sci. Technol., **18,** (2005), 1454.

[81] Lı Y., Kavıraj S., Berenov A., Perkıns G. K., Drıscoll J., Caplın A. D., Cao G. H., Ma Q. Z., Wang B., Weı L., Zhao Z. X., Enhancement of critical current density of (Pb,Sn)-doped Bi-2212 superconductors at high temperature, Physica C**, 355,** (2001), 51.

[82] Görür O., Küçükömeroğlu T., Terzıoğlu C., Varılcı A., Altunbaş M., The effect of Ag diffusion on properties of $YBa_2Cu_3O_{7-x}$ thin films produced by electron beam deposition techniques, Physica C, **418,** (2005), 35.

[83] Yilmazlar M., Ozturk O., Gorur O., Belenli I., Terzioglu C., Role of diffusion-annealing time on the mechanical properties of bulk Bi-2223 superconductors diffusion-doped with Au, Supercond. Sci. Technol.**, 20,** (2007), 365.

[84] Chiu C. W., Meng R. L., Gao L., Huang Z. J., Chen F. And Xue Y. Y., Nature, **365,** (1993), 323.

[85] Halim S. A., Khawaldeh S. A., Mohammed S. B., Azhan H., *Materials* Chemistry and Physic**, 61,** (1999), 251.

[86] Chen, Y.C., Chong, K.K., Meen, T.H.,Heat-treatment effect on the metal contact of high-T_c (Pb, Bi)SrCaCuO superconductor, Jpn. J. Appl. Phys., **30,** (1991), 33.

[87] Yoon, K.H., Lee, Y.B., Formation of the high-Tc phase in lead-doped Bi-Sr-Ca-Cu-O superconductors, J. Mate. Sci., **26,** (1991), 5101.

[88] Dzhafarov, T.D., Altunbaş, M., Varilci, A., and Küçükömeroğlu, T., The effect of au dıffusıon on structural and superconductıng propertıes of YBaCuO, Materials Letters, **25**, (1995), 81.

[89] Persland M. R., Tallon J. L., Buckley R. G., Liu R. S., Flower N. E., General trends in oxygen stoichiometry effects on T_c in Bi and Tl superconductors, Physica C, **176,** (1991), 95.

[90] Aksan M. A., Yakinci M. E., Synthesis and characterization of Er-substituted Bi-2223 H-T-c glass-ceramic superconductors, J. Alloys and Compounds, **385,** (2004), 33.

[91] Ilonca, G. Pop, A.V., Yang, T.R., Jurcut, T., Lung, C., Stiufiuc, G., Stiufiuc, R., Panfilescu, I.A., International Journal of Inorganic Materials, **3**, (2001), 763.

[92] Yegen, D., Terzioglu, C., Gorur, O., Belenli, I., and Varilci, A., Investigation of the cooling rate in Bi(Pb)SrCaCuO high temperature superconductor by low field AC magnetic susceptibility, Chinese Journal of Phys., **44,** (2006), 3.

[93] Celebi, S., Nezir, S., Gencer, A., Yanmaz, E., and Altunbas, M., AC losses and irreversibility line of Bi-(Pb)-Sr-Ca-Cu-O high-T-c superconductors, Journal of Alloys and Compounds, **5,** (1997), 255.

[94] Dzhafarov T. D., Diffusion in High-Temperature Superconductors, Phys. Status Solidi (a), **158,** (1996), 335.

[95] Khalil, S.M., Sedky, A., Annealing temperature effect on the properties of Bi : 2212 superconducting system, Physica B, **357**, (2005), 299.

[96] Ibrahim M.M., and Khalil, S.M., Dependence of some $Bi_{1.7}Pb_{0.3}Sr_2Ca_2Cu_3O_y$ physical properties on the annealing period, Eur. Phys. J. AP, **14**, (2001), 79.

[97] Sarkar A.K., and Maartense, I., Effect of post-sintering quenching parameters on T_c and crystal structure of the $Bi_2Sr_2CaCu_2O_{8+\delta}$ (2212) phase, Physica C, **168**, (1990), 591.

[98] Khalil, S.M., Effects of optimum annealing time on superconducting properties of $Bi_{2-x}Pb_xSr_2Ca_2Cu_3O_y$ system, Phys. Stat. Sol. (a), **178**, (2000), 731.

[99] Shi, L., Dong Q., and Zhang, Y.,Effect of Pb-doping and annealing on the structure and T_c of Bi-2212 phase superconductor, Physica C, **341-348,** (2000), 649.

[100] Biju, A., Abhilash Kumar, R.G., Aloysius, R.P., Syamaprasad, U., Structural and superconducting properties of $Bi_{1.7}Pb_{0.4}Sr_{2-x}Gd_xCa_{1.1}Cu_{2.1}O_y$ system, Physica C, **449**, (2006), 109.

[101] Leenders, A., Ullrich, M., Freyhardt, H.C., Influence of thermal cycling on the mechanical properties of VGF melt-textured YBCO, Physica C, **279**, (1997), 173.

[102] Bruneel, E., Degrieck, J., Van Driessche, I., Hoste, S., Mechanical properties of Bi-2223/Ag bulk composites, Physica C, **372-376,** (2002) 1063.

[103] Ling H.C., and Yan, M.F., Microhardness measurements on dopant modified superconducting $YBa_2Cu_3O_7$ ceramıcs, J. Appl. Phys., **64,** (1988), 1307.

[104] Rabier, J., Denanot, M.F., Dislocations in $YBa_2Cu_3O_{7\text{-delta}}$ ceramics plastically deformed at room-temperature, J. Less-Common Met., **164,** (1990), 223.

[105] Gong, J.H., Wu, J.J., Guan, Z., Analysis of the indentation size effect on the apparent hardness for ceramics, Mater. Lett., **38**, (1999), 197.

[106] Elmustafa, A.A., Stone, D.S., Nanoindentation and the indentation size effect: Kinetics of deformation and strain gradient plasticity, J. Mech. Phys. Solid, **51,** (2003), 357.

[107] Fröhlinch, F., Grau, P., Grellmann, W., Phys. Status Solidi, **42**, (1997), 79.

[108] Li, H., Bradt, R.C., The microhardness indentation load sıze effect in rutile and cassiterite single-crystals. J. Mater. Sci., **28**,(1993), 917.

[109] Hays, C., Kendall, E.G., Metallography, **6** (4), (1973), 275.

[110] Gong, J., Wu, J., Guan, Z., Examination of the indentation size effect in low-load Vickers hardness testing of ceramics, J. Eur. Ceram. Soc., **19**, (1999), 2625.

[111] Li, Z., Ghosh, A., Kobayashi, A.S., Indentation fracture-toughness of sintered silicon-carbide in the palmqvıst crack regime, J. Am. Cer. Soc., **72,** (1989), 904.

[112] Quinn, J.B., Quinn, G.D., Indentation brittleness of ceramics: A fresh approach, J. Mater. Sci., **32,** (1997), 4331.

[113] Dutta, A.K., Narasaiah, N., Chattopadhyaya, A.B., Ray, K.K., The load dependence of hardness in alumina-silver composites, Ceramics International, **27**, (2001), 407.

[114] Hirao, K., Tomozawa, M., Mıcrohardness of SiO_2 glass in various environments, J. Am. Ceram. Soc., **70,** (1987), 497.

[115] Bernhardt, E.O., Z. Metall., **33**, (1941), 135.

[116] Nihara, K., Movena, R.,. Hasselman, D.P.H., Evaluation of klc of brittle solids by the indentation method with low crack-to-indent ratios, J. Mater. Sci., **1**, (1982), 13.

[117] Uzun, O., Kolemen, U., Celebi, S., Guclu, N., Modulus and hardness evaluation of polycrystalline superconductors by dynamic microindentation technique, J. Europ. Ceramic Soc., **25**, (2005), 969.

[118] Mott, B.W., Microindentation Hardness Testing , vol. **9**, Butterworths, London, 1956.

[119] Sangwal, K., Surowska, B., Study of indentation size effect and microhardness of $SrLaAlO_4$ and $SrLaGaO_4$ single crystals, Mater. Res. Innov., **7**, (2003), 91.

[120] Tickoo, R., Tandon, R.P., Bamzai, K.K., Kotru, P.N., Microindentation studies on samarium-modified lead titanate ceramics, Mater. Chem. Phys., **80**, (2003), 446.

[121] Peng, Z., Gong, J., Miamo, H., On the description of indentation size effect in hardness testing for ceramics: Analysis of the nanoindentation data, J. Of Eur. Ceram. Soc., **24**, (2004), 2193.

Appendix A:

DETERMINATION OF THE TEMPERATURE ZONE IN THE FURNACE

In order to prepare high quality superconductor, the calibration of the furnace used during the annealing is very important. For this purpose, the furnace is calibrated using a thermocouple and the regions of stable temperature are determined. The data for different temperatures are drawn in the graph shown below. Generally deviations of 3-5 K from the set temperature are obtained.

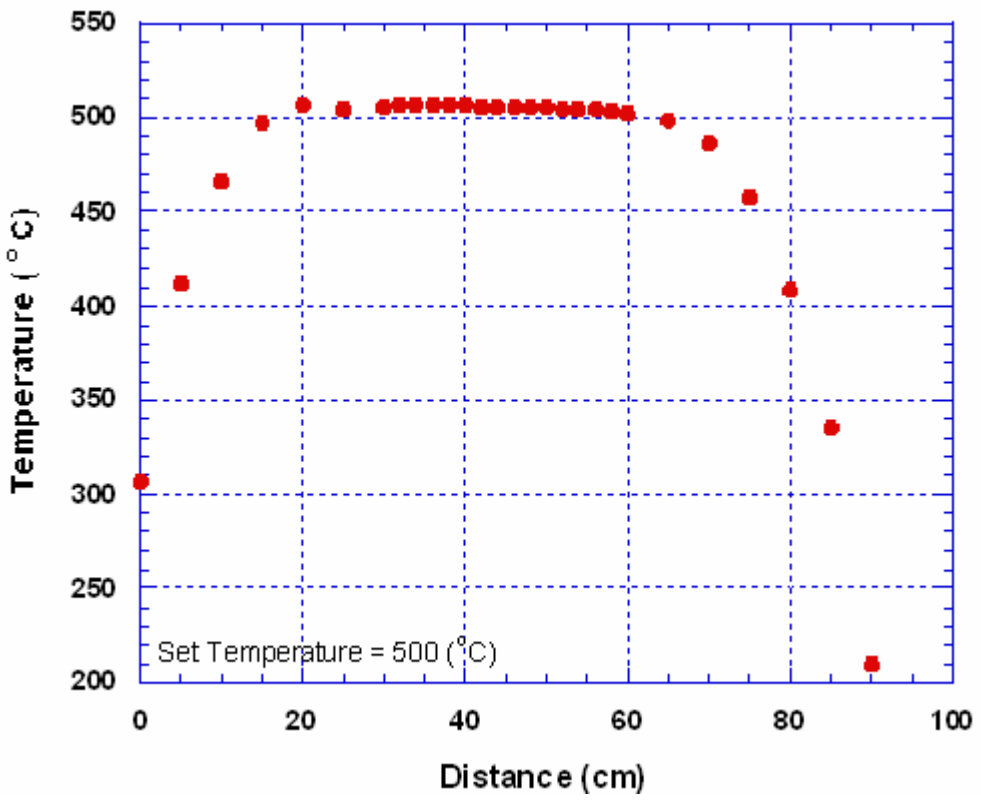

Figure A1: Calibration curve of the furnace (PROTHERM Model PTF 12/75/200) at the set temperature 500 ° C.

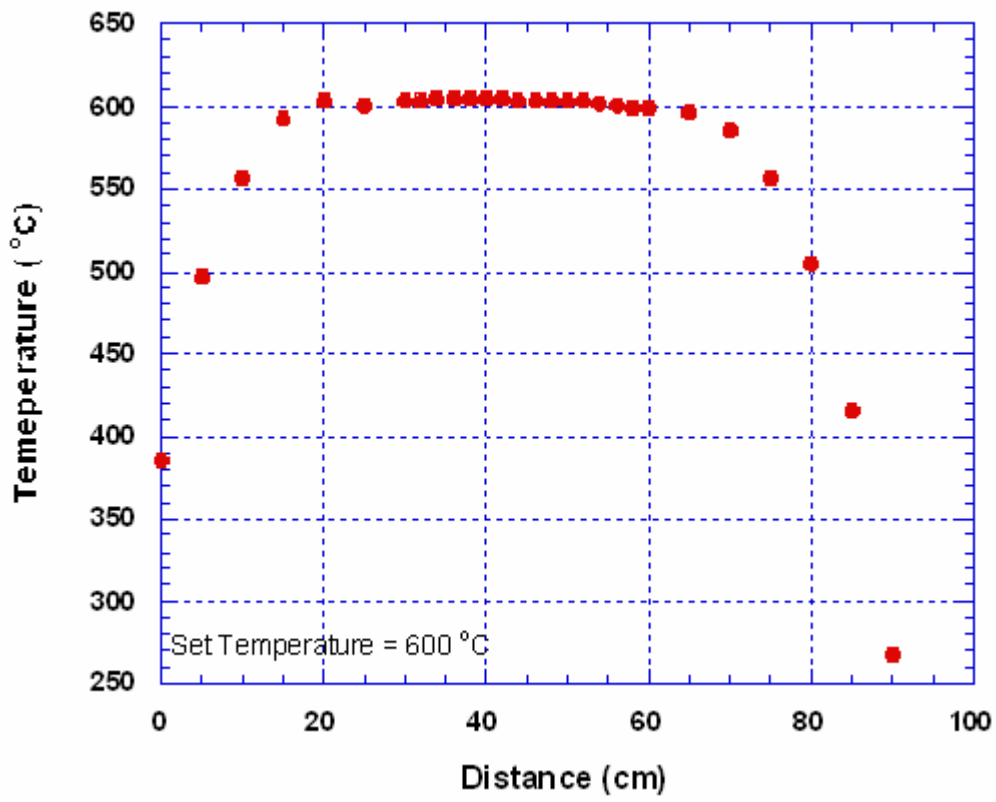

Figure A2: Calibration curve of the furnace (PROTHERM Model PTF 12/75/200) at the set temperature 600 ° C.

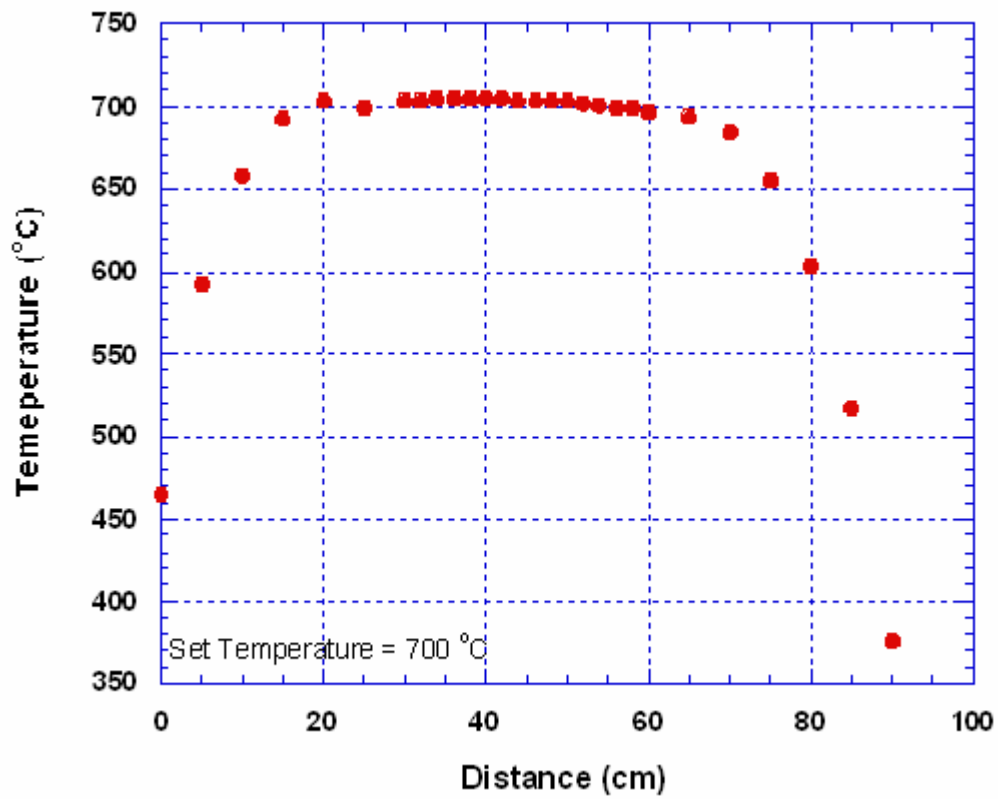

Figure A3: Calibration curve of the furnace (PROTHERM Model PTF 12/75/200) at the set temperature 700 ° C.

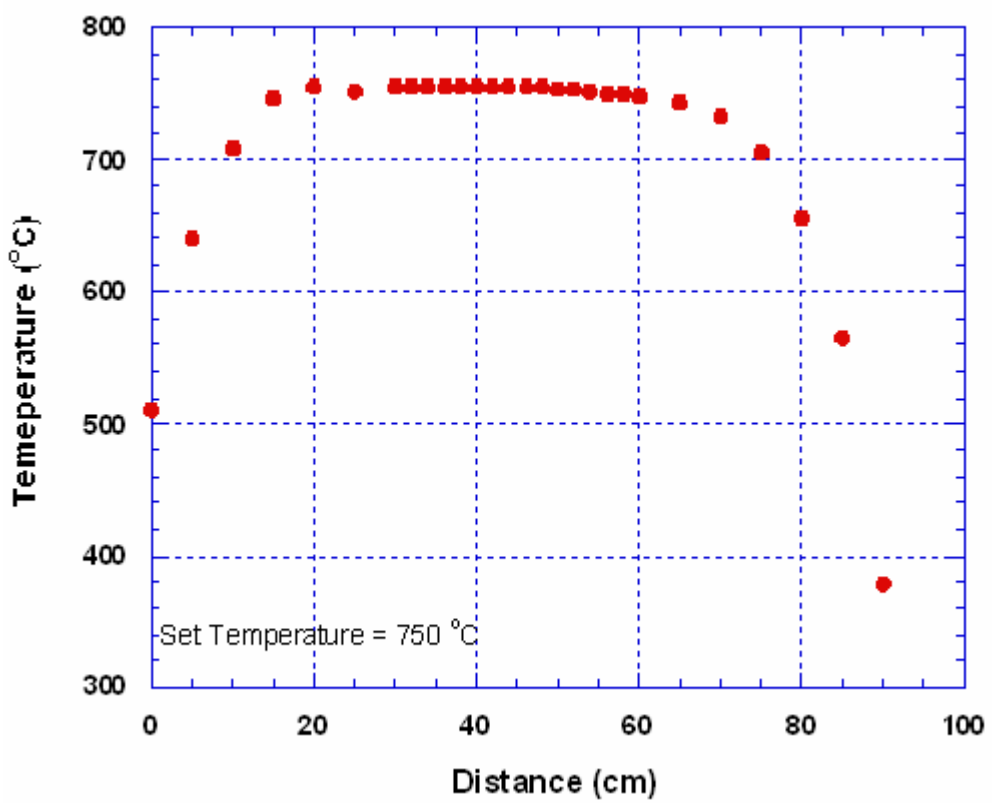

Figure A4: Calibration curve of the furnace (PROTHERM Model PTF 12/75/200) at the set temperature 750 ° C.

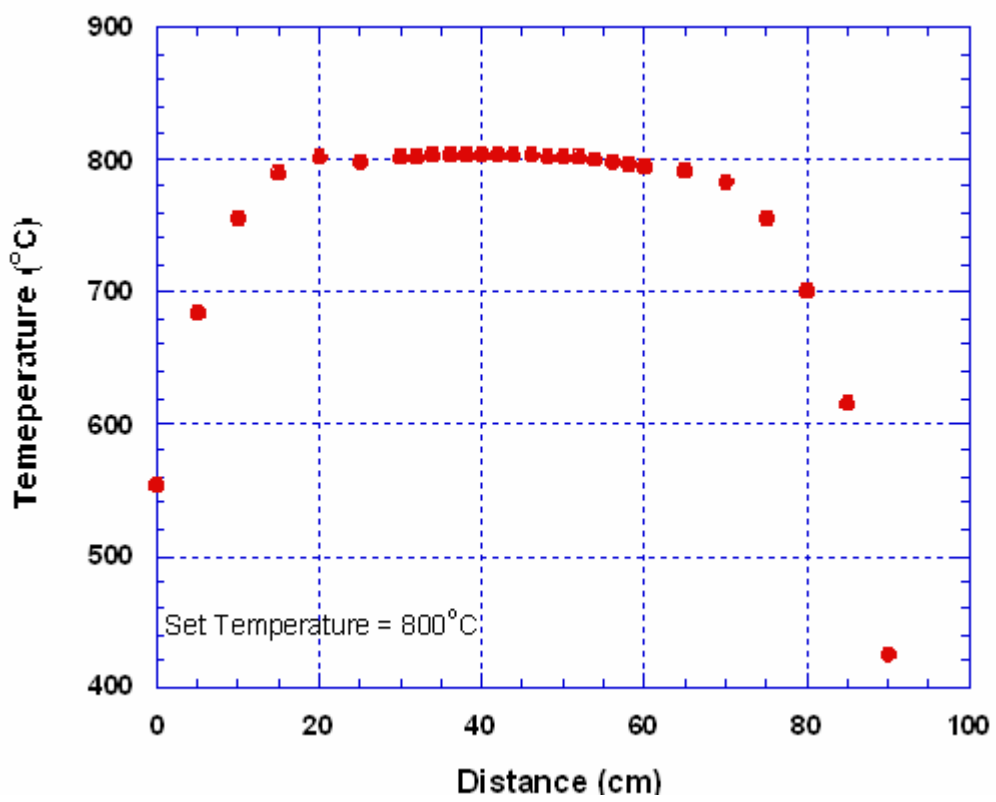

Figure A5: Calibration curve of the furnace (PROTHERM Model PTF 12/75/200) at the set temperature 800 ° C.

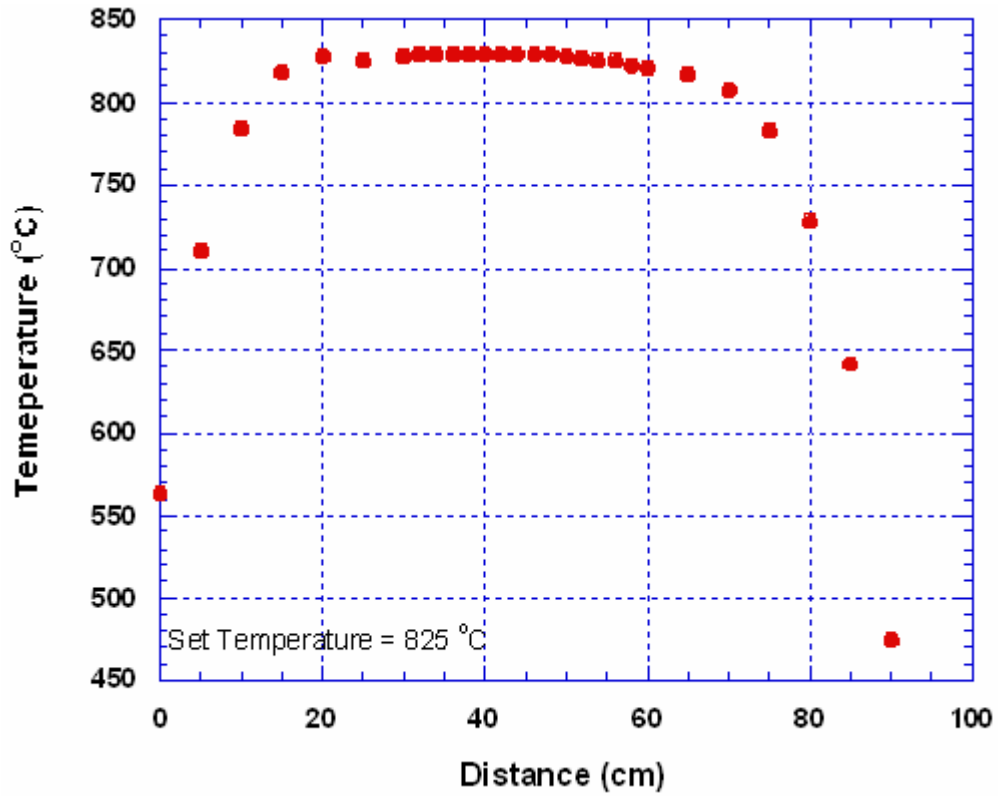

Figure A6: Calibration curve of the furnace (PROTHERM Model PTF 12/75/200) at the set temperature 825 ° C.

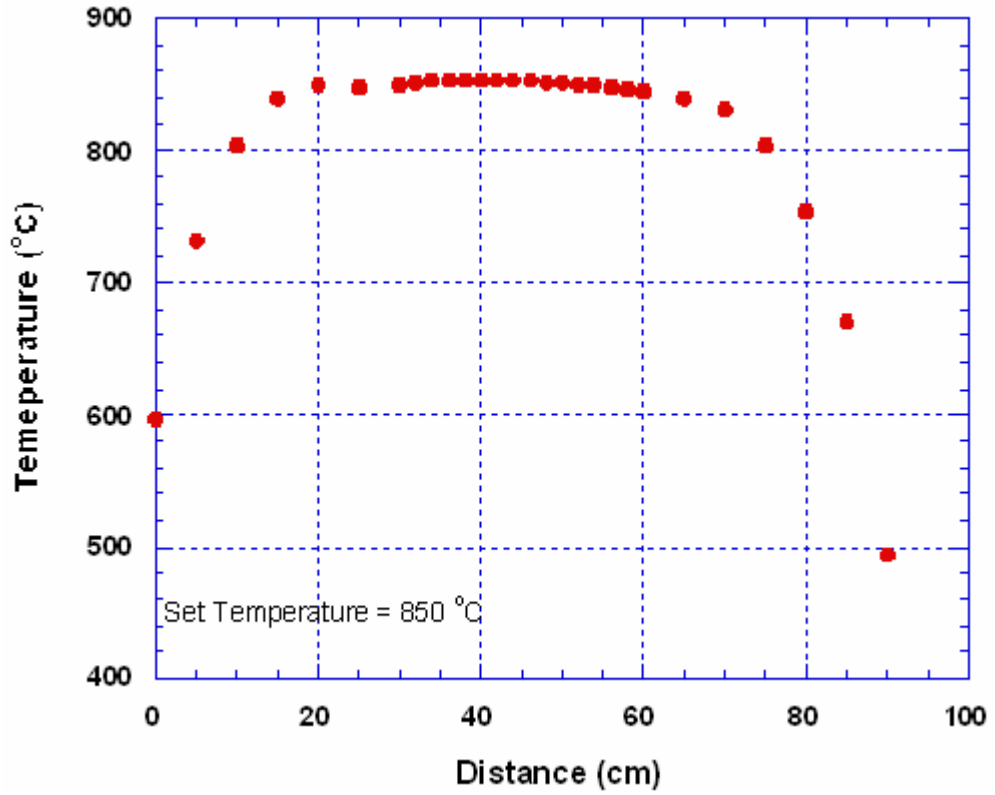

Figure A7: Calibration curve of the furnace (PROTHERM Model PTF 12/75/200) at the set temperature 850 ° C

CURRICULUM VITAE

Name Surname **:** Özgür ÖZTÜRK

Permanent Address **:** Bahçelievler Mah. Konak Sok. No: 11/20 BOLU

Degree and date to be conferred: Doktora, 2007

Place Date of Birth **:** Bandırma, 1974

Secondary education **:** 29 Ekim Orta Okulu, Ankara, 1988

Bahçelievler Deneme Lisesi, Ankara, 1991

Collegiate instituons attended	**Degree**	**Date of Degree**
Ankara University	B.S	1998
Abant Izzet Baysal Uni.	M.S	2002
Abant Izzet Baysal Uni.	Ph.D	2007

Subspecialty: Solid State Physics

Publications:

Publications in S.C. indexed Journals:

1- Terziglu, C., Yilmazlar, M. **Ozturk**, **O.**,Yanmaz**,** E., Structural and physical properties of Sm-doped $Bi_{1.6}Pb_{0.4}Sr_2Ca_{2-x}Sm_xCu_3O_y$, Physica C, 423, 119-126 (2005).

2- Terzioglu,C., **Ozturk**, **O.,** Kılic, A., Gencer, A., Belenli, İ., Effect of cooling rates on bare bulk and silver wrapped pellets of Bi- 2223 superconductor, Physica C, 434, 153-156, (2006).

3- Terzioglu, C., **Ozturk**, **O.,** Kilic, A., Goodrich, R.G and Fisk**,** Z., Magnetic and Electronic Measurements in CeB_6 Journal of Magnetism and Magnetic Materials, 298, 33-37, (2006).

4- Yilmazlar, M., Cetinkara, H.A, Nursoy, M., **Ozturk**, **O.,** Terzioglu, C., Thermal Expansion and Vickers Hardness of $Bi_{1.6}Pb_{0.4}Sr_2Ca_{2-x}Sm_xCu_3O_y$ Superconductors, Physica C, 442, 101-107,(2006).

5- Ozturk, O., Yegen, D., Yılmazlar, M., Varilci A., Terzioglu,C., The effect of cooling rates on properties of $Bi_{1.7}Pb_{0.35}Sr_{1.9}Ca_{2.1}Cu_3O_y$ superconductors produced by solid state reaction method, Physica C, 451, 113-117, (2007).

6- Yılmazlar, M., **Ozturk, O**., Aydın, H., Akdogan, M., Terzioğlu, C., The effect of Sm-Ca Substitution on Mechanical Properties of BSCCO superconductors, Chinese Journal of Phys., Vol.45,No.2-I,(2007).

7- Yılmazlar, M., **Ozturk, O**., Gorur, O., Belenli, İ., Terzioğlu, C., Role of diffusion-annealing time on the mechanical properties of bulk Bi-2223 superconductors diffusion-doped with Au, Supercond. Sci. and Technol., 20, 365, (2007).

8- Ozturk, O., Akdogan, M., Aydın, H., Yılmazlar, M., Terzioglu, C, Belenli, I.,Substitution of Sm at Cu site in $Bi_{1.6}Pb_{0.4}Sr_2Ca_{2-x}Sm_xCu_3O_y$ superconductors, Physica B, 399, 94-100 (2007).

9- Ozturk, O., Kucukomeroglu, T., Terzioglu, C., The calculation of diffusion coefficient of Au in Bi-2223 superconductors, Jurnal of Phys.- Condansed Matter,19,346205,(10pp) (2007).

10- Ozturk, O., Kuçukomeroğlu, T., Varilci A., Belenli, I., and Terzioglu,C., The effect of Au diffusion on structural and physical properties of $Bi_{1.8}Pb_{0.35}Sr_{1.9}Ca_{2.1}Cu_3O_y$ superconductors. Chinese Phys. Lett., (in review) (2007).

11- Ozturk, O., Terzioglu, C., Influence of diffusion-annealing temperature on the physico-mechanical properties of Au-doped Bi-2223 superconductors. Chinese Journal of Physics, (in review) (2007).

12- Ozturk, O., Aydın, H., Varilci A., Terzioglu,C., Belenli, I., The influence of Gd addition on microstructure and transport properties of Bi-2223, Chinese Physics Letters, (in review) (2007).

13- Ozturk, O., Terzioglu, C., Influence of gold diffusion-doped on phase formation, superconducting and microstructure properties of Bi-2223 superconductors, Jurnal of Phys.- Condansed Matter, (in review) (2007).

Talks in national refereed Conventions and Symposiums:

1- Ö. Öztürk, C. Terzioğlu, A. Kılıç, A. Gencer ve İ. Belenli, Bi-2223 Katı Numunelerde Gümüş Kılıfın Soğutma Sırasında Oksijen Girişine Etkisi, TFD-22. Fizik Kongresi, (2004).

2- Ö. Öztürk, C. Terzioğlu, A. Kılıç, R. G. Goodrich ve Z. Fisk, Tek Kristal CeB_6'nın düşük manyetik alan altında özdirenç ölçümleri, TFD-22. Fizik Kongresi, (2004).

3- Ö. Öztürk, M. Yılmazlar, C. Terzioğlu, M. Akdoğan, E. Yanmaz, İ. Belenli Sm Katkılı $Bi_{1.6}Pb_{0.4}Sr_2Ca_{2-x}Sm_xCu_3O_y$ Bileşiğinin Elektiriksel ve Yapısal Özelliklerinin İncelenmesi, III. Ulusal Yüksek Sıcaklık Süperiletkenler Sempozyumu, (2005).

4- M. Erdem, **Ö. Öztürk**, C. Terzioğlu, İ. Belenli, N. Türetken, Effect of Annealing Time on $YBa_2Cu_3O_{7-x,}$ III. Ulusal Yüksek Sıcaklık Süperiletkenler Sempozyumu, (2005).

5- H. Aydın, M. Yılmazlar, **Ö. Öztürk**, M. Akdoğan, S. Nezir, C. Terzioğlu, Sm Katkılanmış BiPbSrCaCuO Süperiletkenlerin Transport Ölçümleri, III. Ulusal Yüksek Sıcaklık Süperiletkenler Sempozyumu, (2005).

Talks in international refereed Conventions and Symposiums:

1- M. Yılmazlar, H. Aydın, H. A. Çetinkara, **Ö. Öztürk**, C. Terzioğlu, M. B. Türköz, Ca Yerine Sm Katkılanmış BiPbSrCaCuO süperiletkenlerinin Aktivasyon Enerjilerinin Hesaplanması, TFD-23. Uluslararası Fizik Kongresi, (2005).

2- Ozgur Ozturk, Mustafa Yilmazlar, Tayfur Kucukomeroglu, Osman Gorur, Cabir Terzioglu, Investigation of some physical properties of gold diffusion-doped $Bi_{1.8}Pb_{0.35}Sr_{1.9}Ca_{2.1}Cu_3O_y$ superconductors, APS, March Meeting, Denver-Colorado, (2007).

3- Murat Erdem, **Ozgur Ozturk,** Cabir Terzioglu, Ibrahim Belenli, Orientation and grain boundaries in bulk samples of Bi-2223 phase, APS, March Meeting, Denver-Colorado, (2007).

4- Mustafa Akdogan, Erhan Budak, **Ozgur Ozturk,** Cabir Terzioglu, Ibrahim Belenli, The effect of hBN addition on properties of Bi-2223 superconductors, APS, March Meeting, Denver-Colorado, (2007).

5- Huseyin Aydin, Mustafa Yilmazlar, **Ozgur Ozturk,** Dincer Yegen, Cabir Terzioglu, The effect of Sm substitution on properties of $Bi_{1.6}Pb_{0.4}Sr_2Ca_{2-x}Sm_xCu_3O_y$ superconductors, APS, March Meeting, Denver-Colorado, (2007).

6- Ö. Öztürk, C. Terzioğlu, Difüzyon-ısıl işlem süresinin, difüzyon yoluyla altın katkılanmış Bi-2223 süperiletkeninin mekanik özellikleri üzerine etkisi, TFD-24. Uluslararası Fizik Kongresi, (2007).

Positions held: He has been working as research and teaching assistant Abant Izzet Baysal University department of Physics since 1998**.**